

2

# NAVAL POSTGRADUATE SCHOOL

Monterey, California

AD-A232 473



DTIC  
ELECTE  
MAR 12 1991  
S B D

## THESIS

PHASE TRANSFORMATIONS AND MICROSTRUCTURAL  
EVOLUTION IN AGED Mn-Cu-BASED ALLOYS

by

Guy Victor Holsten

June, 1990

Thesis Advisor:

Jeff Perkins

Approved for public release; distribution is unlimited.

91 3 06 033

| REPORT DOCUMENTATION PAGE  |       |   |  | Form Approved<br>OMB No 0704-0188                  |                            |
|--|-------|---|--|--|----------------------------|
| 1a REPORT SECURITY CLASSIFICATION<br>UNCLASSIFIED  |       |   | 1b RESTRICTIVE MARKINGS  |  |                            |
| 2a SECURITY CLASSIFICATION AUTHORITY   |       |   | 3 DISTRIBUTION / AVAILABILITY OF REPORT  |  |                            |
| 2b DECLASSIFICATION / DOWNGRADING SCHEDULE   |       |   |  |  |                            |
| 4. PERFORMING ORGANIZATION REPORT NUMBER(S)  |       |   | 5 MONITORING ORGANIZATION REPORT NUMBER(S)   |  |                            |
| 6a NAME OF PERFORMING ORGANIZATION<br>NAVAL POSTGRADUATE<br>SCHOOL   |       | 6b OFFICE SYMBOL<br>(If applicable)<br>34 | 7a. NAME OF MONITORING ORGANIZATION<br>Naval Postgraduate School   |  |                            |
| 6c. ADDRESS (City, State, and ZIP Code)<br>Monterey, CA 93943-5000   |       |   | 7b ADDRESS (City, State, and ZIP Code)<br>Monterey, CA 93943-5000  |  |                            |
| 8a. NAME OF FUNDING / SPONSORING<br>ORGANIZATION   |       | 8b OFFICE SYMBOL<br>(If applicable)       | 9. PROCUREMENT INSTRUMENT IDENTIFICATION NUMBER  |  |                            |
| 8c. ADDRESS (City, State, and ZIP Code)  |       |   | 10 SOURCE OF FUNDING NUMBERS   |  |                            |
|  |       |   | PROGRAM<br>ELEMENT NO  | PROJECT<br>NO                                      | TASK<br>NO                 |
| 11 TITLE (Include Security Classification)<br>PHASE TRANSFORMATIONS AND MICROSTRUCTURAL EVOLUTION IN AGED Mn-Cu-BASED ALLOYS   |       |   |  |  |                            |
| 12 PERSONAL AUTHOR(S)<br>Holsten, Guy V.   |       |   |  |  |                            |
| 13a TYPE OF REPORT<br>Master's Thesis  |       | 13b TIME COVERED<br>FROM _____ TO _____   |  | 14. DATE OF REPORT (Year, Month, Day)<br>June 1990 |                            |
| 15 PAGE COUNT<br>100   |       |   |  |  |                            |
| 16 SUPPLEMENTARY NOTATION<br>The views expressed in this thesis are those of the author and do not reflect the official policy or position of the Department of Defense or the U.S. Government   |       |   |  |  |                            |
| 17 COSATI CODES  |       |   | 18 SUBJECT TERMS (Continue on reverse if necessary and identify by block number)<br><br>High Damping Alloys, Spinodal Decomposition,<br>Cu-Mn alloys, Flickering |  |                            |
| FIELD  | GROUP | SUB-GROUP                                 |  |  |                            |
|  |       |   |  |  |                            |
|  |       |   |  |  |                            |
| 19. Abstract: The transformation behavior of aged Mn-Cu-based alloys was studied via transmission electron microscopy. The evolution of several unique forms of diffraction contrast, such as "tweed" and "flickering", was characterized and correlated with the underlying transformation behavior. Convergent beam microbeam compositional analysis and high resolution lattice imaging techniques were employed to assist in the interpretations. It was determined that upon aging these alloys, a FCC solid solution decomposes into a fine dispersion of Mn-rich and Mn-poor regions which coarsen with further aging. This decomposition was modeled using finite difference techniques. The Mn-rich regions were determined to undergo a crystallographic transformation which involves a slight tetragonal distortion upon cooling. For short aging times, when the elastic strain fields around each of the finely dispersed FCT regions overlap sufficiently, tweed contrast is observed. At longer aging times, the Mn-rich regions grow and become further apart, so that the strain fields of the FCT crystallites do not overlap so much, and the tweed contrast diminishes and is replaced by a V-shaped morphology within the FCT regions which resembles a set of self-accommodating crystals. In all stages of aging, the orientation of the tetragonal c-axis is easily switched by elastic excitation, giving rise to the unique flickering contrast in the TEM. |       |   |  |  |                            |
| 20 DISTRIBUTION / AVAILABILITY OF ABSTRACT<br><input checked="" type="checkbox"/> UNCLASSIFIED/UNLIMITED <input type="checkbox"/> SAME AS RPT <input type="checkbox"/> DTIC USERS  |       |   | 21 ABSTRACT SECURITY CLASSIFICATION<br>Unclassified  |  |                            |
| 22a NAME OF RESPONSIBLE INDIVIDUAL<br>Jeff Perkins   |       |   | 22b TELEPHONE (Include Area Code)<br>(408) 646-2216  |  | 22c OFFICE SYMBOL<br>69 Ps |

Approved for public release; distribution is unlimited.

**PHASE TRANSFORMATIONS AND MICROSTRUCTURAL  
EVOLUTION IN AGED Mn-Cu-BASED ALLOYS**

by

**Guy Victor Holsten**  
**Lieutenant, United States Navy**  
**B.S., University of the State of New York**

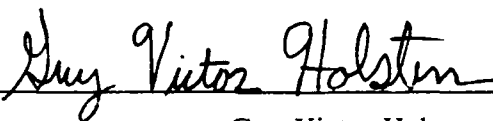
Submitted in partial fulfillment  
of the requirements for the degree of  
**MASTER OF SCIENCE IN MECHANICAL ENGINEERING**  
and

**MECHANICAL ENGINEER**

from the  
**NAVAL POSTGRADUATE SCHOOL**

June 1990

Author:

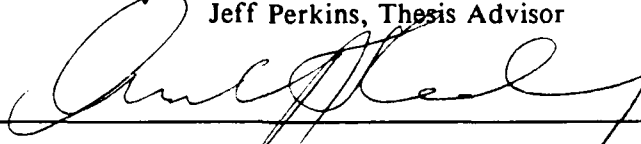


Guy Victor Holsten

Approved by:



Jeff Perkins, Thesis Advisor



Anthony Healey, Chairman

Department of Mechanical Engineering



**DEAN OF FACULTY  
AND GRADUATE STUDIES**

## ABSTRACT

The transformation behavior of aged Mn-Cu-based alloys was studied via transmission electron microscopy. The evolution of several unique forms of diffraction contrast, such as "tweed" and "flickering", was characterized and correlated with the underlying transformation behavior. Convergent beam microbeam compositional analysis and high resolution lattice imaging techniques were employed to assist in the interpretations. It was determined that upon aging these alloys, a FCC solid solution decomposes into a fine dispersion of Mn-rich and Mn-poor regions which coarsen with further aging. This decomposition was modeled using finite difference techniques. The Mn-rich regions were determined to undergo a crystallographic transformation which involves a slight tetragonal distortion upon cooling. For short aging times, when the elastic strain fields around each of the finely dispersed FCT regions overlap sufficiently, tweed contrast is observed. At longer aging times, the Mn-rich regions grow and become further apart, so that the strain fields of the FCT crystallites do not overlap so much, and the tweed contrast diminishes and is replaced by a V-shaped morphology within the FCT regions which resembles a set of self-accommodating crystals. In all stages of aging, the orientation of the tetragonal c-axis is easily switched by elastic excitation, giving rise to the unique flickering contrast in the TEM.



|                    |                                     |
|--------------------|-------------------------------------|
| Accession For      |                                     |
| NTIS GRA&I         | <input checked="" type="checkbox"/> |
| DTIC TAB           | <input type="checkbox"/>            |
| Unannounced        | <input type="checkbox"/>            |
| Justification      |                                     |
| By                 |                                     |
| Distribution/      |                                     |
| Availability Codes |                                     |
| Dist               | Avail and/or Special                |
| A-1                |                                     |

## TABLE OF CONTENTS

|             |                                    |           |
|-------------|------------------------------------|-----------|
| <b>I.</b>   | <b>INTRODUCTION</b>                | <b>1</b>  |
| <b>II.</b>  | <b>SUMMARY OF PREVIOUS WORK</b>    | <b>2</b>  |
| <b>III.</b> | <b>EXPERIMENTAL METHODS</b>        | <b>8</b>  |
| <b>IV.</b>  | <b>RESULTS</b>                     | <b>10</b> |
| <b>A.</b>   | <b>EARLY STAGES OF AGING</b>       | <b>10</b> |
| 1.          | "Mottled" Contrast Microstructures | 10        |
| 2.          | "String" Images                    | 11        |
| 3.          | "Tweed" Contrast                   | 11        |
| a.          | (100) Orientation                  | 12        |
| b.          | (110) Orientation                  | 12        |
| c.          | (111) Orientation                  | 12        |
| 4.          | Streaking in Diffraction Patterns  | 12        |
| 5.          | "Tweed Bands"                      | 14        |
| 6.          | "Flickering Contrast"              | 17        |
| 7.          | High Resolution TEM                | 19        |
| <b>B.</b>   | <b>LATER STAGES OF AGING</b>       | <b>20</b> |
| 1.          | Reduction in "tweed" contrast      | 20        |
| 2.          | "V-shaped" contrast                | 21        |

|    |  |    |
|----|--|----|
| 3. | "Flickering" of V-shaped contrast .....                                    | 25 |
| 4. | Diffraction Results at Longer Aging Times .....                            | 27 |
| 5. | Trace Analysis and Extinction Behavior of the V-contrast .....             | 28 |
| 6. | Diffraction Streaking: Extinction Analysis .....                           | 35 |
| 7. | High Resolution TEM .....  | 41 |
| 8. | Microbeam compositional analysis .....                                     | 44 |
| V. | DISCUSSION .....   | 46 |
| A. | "Mottled" and "String" Images .....  | 46 |
| B. | Tweed Contrast .....   | 47 |
| C. | "Tweed Bands" .....  | 48 |
| D. | "V-shaped" Contrast .....  | 49 |
| E. | Modeling of the Microstructure .....                                       | 50 |
| 1. | Strain Effects on Transformation .....                                     | 50 |
| 2. | Mechanism of Flickering .....  | 52 |
| 3. | Thermodynamic Transformation Model .....                                   | 56 |
| 4. | Computer Model of the Transformation .....                                 | 58 |
| 5. | Computer Model Results .....   | 60 |
| F. | Mechanisms of High Damping .....   | 68 |
| 1. | Strain Dependence of Damping .....   | 68 |
| 2. | Damping by Microstructural Boundaries .....                                | 69 |
| 3. | Atomistic Structure of High-Damping Boundaries in<br>Microstructures ..... | 70 |

|                                     |  |    |
|-------------------------------------|--|----|
| a.                                  | Martensite Intervariant Boundaries . . . . .           | 71 |
| b.                                  | Ferromagnetic Domain Walls . . . . .                   | 72 |
| c.                                  | Mini-twins in Antiferromagnetic Mn-Cu Alloys . . . . . | 73 |
| 4.                                  | High Damping in Mn-Cu alloys . . . . .                 | 73 |
| VI. SUMMARY . . . . .               |  | 76 |
| APPENDIX . . . . .                  |  | 79 |
| LIST OF REFERENCES . . . . .        |  | 85 |
| INITIAL DISTRIBUTION LIST . . . . . |  | 93 |

## I. INTRODUCTION

The physical metallurgy of alloys based on the Cu-Mn system has been a subject of research for more than 40 years [Ref. 1-4]. Particular attention has been given to Mn-rich alloys which have a face centered cubic structure at high temperature, but when cooled, or aged and cooled, are known to undergo an antiferromagnetic transition [Ref. 5-9], to form a twinned face centered tetragonal structure [Ref. 9-12], and to display high damping behavior [Ref. 8,11,13-20]. These various features have been appreciated for some time, and it has come to be realized that they are intimately linked to one another.

The present work was intended chiefly to clarify the transformation behavior of aged alloys which have been subjected to the sort of heat treatment schedule which creates a high-damping condition. This typically consists of solution-treatment in the FCC range, followed by aging within what is now realized to be a miscibility gap in the lower FCC range, then cooling. While a reasonably coherent explanation of the transformation behavior can be built out of the existing literature, there are several key aspects which lack sufficient explanation, and which have not been subjected to explicit investigation. For example, the exact nature of the high damping microstructures of aged Cu-Mn based alloys has not been at all well defined. In addition, in spite of the large body of work on the Cu-Mn system in general, the effects of aging temperature and time, of alloy composition, and of the extent of cooling after aging on transformations and microstructure are not well known. Therefore, the present research was designed to systematically investigate these aspects.



## II. SUMMARY OF PREVIOUS WORK

In the past, particularly in the 1960's, fairly detailed work was reported on transformations and microstructures which are specifically linked to high damping in Cu-Mn-based alloys [Ref. 15-21]. Much of this work concentrated on transformations during cooling of fairly Mn-rich FCC solid solutions, including determinations of the crystallography and microstructure of the transformed state [Ref. 15-17,21]. In addition, numerous studies have been made of the effect of lower temperature aging on the microstructure and properties [Ref. 18-20,22,23]. It is now realized that decomposition during aging initiates within a metastable miscibility gap, which exists in the lower temperature range of the FCC phase, and reliable determinations have been made of the extent of this gap and of the kinetics of phase separation within it [Ref. 24-30]. The most thorough and revealing body of research on the metal physics of Cu-Mn-based alloys has been reported in the Russian open literature over the period 1972 to 1986 [Ref. 24,27,28,31-52], particularly by Vintaykin and coworkers. This has included detailed reports on aging [Ref. 24,27,28,31-36], damping and internal friction [Ref. 31,37,38], the antiferromagnetic transition [Ref. 34,39], the FCC-to-FCT transition [Ref. 32,39], elastic constants and phonon spectra [Ref. 31,40,41], "pre-martensitic" phenomena [Ref. 39,41-44], shape memory behavior [Ref. 45-51], deformation behavior [Ref. 48,50-52] and ternary alloying effects [Ref. 35,36,49]. In this same period, work elsewhere has been more scattered but nevertheless has provided excellent additional insight to the transformation behavior of these alloys. This has included extensive research in Japan [Ref. 21,53-65], which has emphasized techniques to monitor the FCC-to-FCT transition and/or characterize the twinned FCT structure,

including internal friction and ultrasonic attenuation methods [Ref. 53-59], x-ray and neutron scattering [Ref. 60-62] and x-ray and electron diffraction and electron microscopy [Ref. 63-65]. These results have revealed very interesting crystallographic details of the lattice transition [Ref. 60,63], and the behavior of phonon spectra [Ref. 61] and elastic moduli [Ref. 21,62] in the vicinity of the transition. A limited number of other studies on Cu-Mn alloys have been carried out in Germany [Ref. 25,66-68], Australia [Ref. 69], India [Ref. 26], the United Kingdom [Ref. 70], Canada [Ref. 71-72], Hungary [Ref. 73] and the United States [Ref. 74].

Before proceeding with the presentation of results, it will be useful to present a brief summary of the known physical metallurgy of Mn-rich Cu-Mn alloys. In this part of the phase diagram, a broad FCC solid solution phase exists at high temperature, as seen in Fig. 1, which is based on the phase diagram recently republished by Massalski et al [Ref. 75]. Upon cooling of the FCC phase, an antiferromagnetic ordering reaction is observed to occur [Ref. 5-9], with the Neel temperature,  $T_N$ , increasing with increasing Mn content [Ref. 6,21,22]. The variation of Neel temperature with composition which has been accurately transferred onto Fig. 1 is based on what is believed to be very reliable compilation of data presented by Vitek and Warlimont [Ref. 25], based on their work and that of others [Ref. 6,21,22]. Closely associated with this magnetic transition is a tetragonal distortion of the FCC lattice [Ref. 6,9,12,20,63] which eventually leads to a twinned FCT microstructure which may be regarded as quasi-martensitic [Ref. 76]. This sort of microstructure, which has long been known to be quite high damping [Ref. 8,11,14,15] consists of an assembly of twin-related plate-like FCT crystals [Ref. 12,16,18-20]. This form of microstructure has as

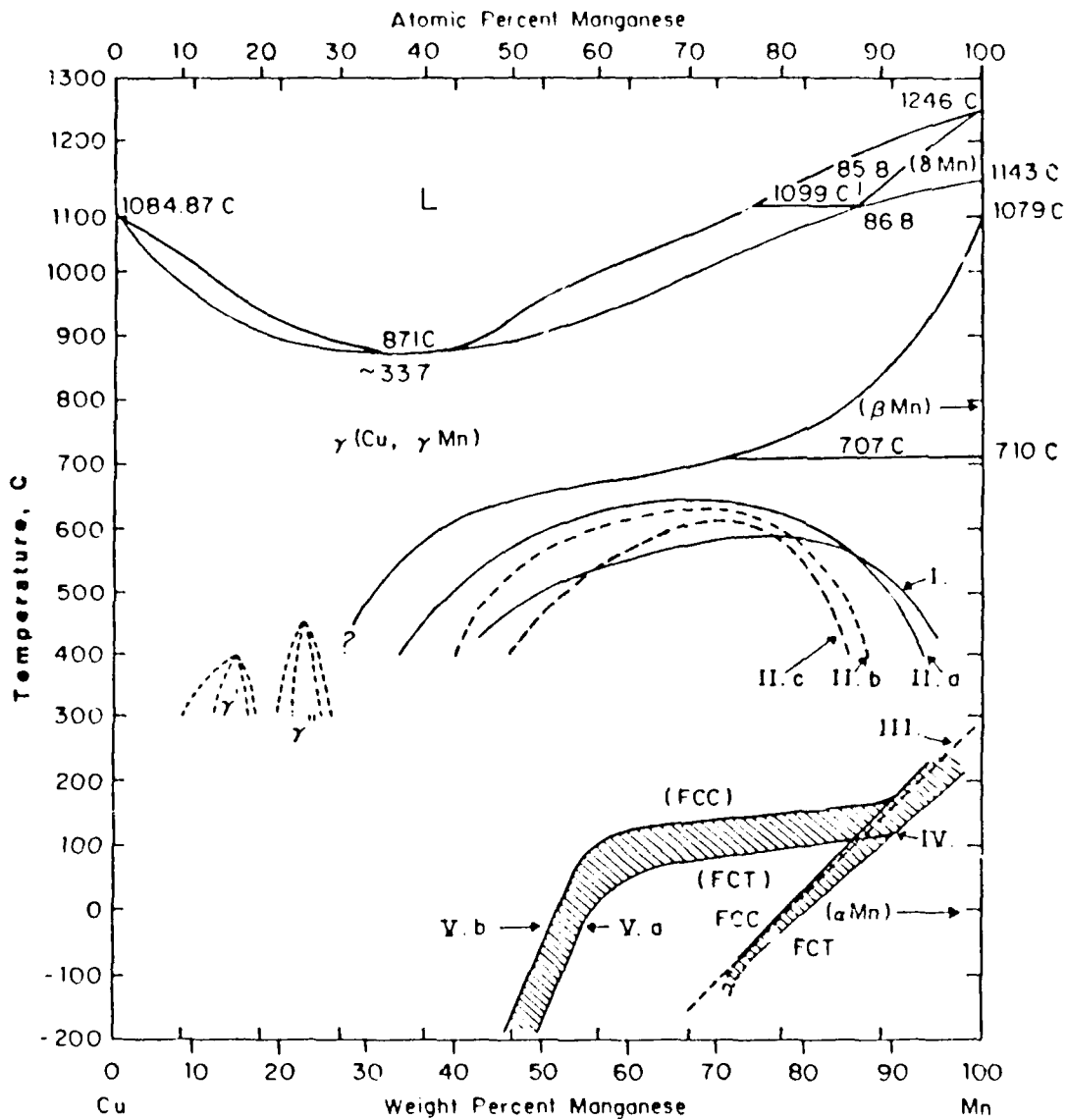


Figure 1: The Cu-Mn binary phase diagram showing the Miscibility gap,  $M_s$  and  $T_n$  [Ref. 75].

- I. Miscibility Gap [Ref. 25].
- II. Miscibility Gap [Ref. 24].
  - a. Layering range.
  - b. Chemical Spinodal.
  - c. Coherent Spinodal.
- III. Neel temperature [Ref. 25].
- IV. FCC to FCT transition in quenched alloy [Ref. 12].
- V. FCC to FCT transition in aged alloys [Ref. 32].

been characterized in some detail with electron microscopy by Butler and Kelly [Ref. 16], Nittono and coworkers [Ref. 63] and Shimizu and coworkers [Ref. 64]. It should be noted that in these martensitic structures, each martensite plate corresponds to one antiferromagnetic domain, and the twin boundaries which separate the plates are identical to the magnetic domain boundaries. The tetragonal c-axes, which have a different orientation in each plate and are twin-related across the boundaries, correspond to one of three variants of distortion which the magnetic transition can induce. The temperature at which the twinned plate-like microstructure begins to form, conventionally labeled as  $M_s$  (the martensite start temperature), has been determined by various workers [Ref. 9,12,63]. It is now clear that this temperature is usually only very slightly below  $T_N$ , and for some alloy compositions,  $T_N$  and  $M_s$  are virtually coincident [Ref. 9,69]. It seems that a gradual tetragonal distortion begins at  $T_N$ , but the creation of the plate-like structure usually requires a bit of undercooling. The data for  $M_s$  and  $M_f$  which has been carefully plotted on Fig. 1 is taken from the early work of Basinski and Christian [Ref. 12], the precision of which has stood the test of time. As can be seen from this figure, due to the composition dependence of  $T_N$  and  $M_s$ , the transition temperature for the FCC-to-FCT transformation falls below room temperature when the Mn content of the FCC solid solution phase is reduced to about 82 at. % or below. Therefore, homogeneous quenched alloys with Mn content greater than about 82 at. % will be tetragonal at room temperature, while those with Mn content less than this be cubic at room temperature unless subjected to an intermediate aging treatment [Ref. 16,18,20,24].

As a result of this composition dependence of  $M_s$ , and in order to create high damping microstructures in alloys with Mn content lower than 82 at. %, aging treatments at

temperatures in the range 350°C to 450°C have typically been employed [Ref. 16,18-20,24,55]. It is now very well established that these aging treatments are based on a compositional phase separation reaction which occurs upon aging within the metastable miscibility gap in the phase diagram [Ref. 24-30]. Although there has been some uncertainty about the limits of this gap, it may now be regarded as fairly well defined, and its delineation is shown on Fig. 1, from two sources [Ref. 24,25], one of which has also provided a calculation of the chemical and strain-modified spinodal limits [Ref. 24].

Because appropriate aging within this gap can create a high damping condition, it has often been assumed that the associated high damping microstructure of aged alloys is also of the twinned quasi-martensitic type found in quenched Mn-rich alloys, and that the primary damping mechanism involves the cyclic movement of twin boundaries. However, there has been no direct evidence that this is the case. One thing that is beyond dispute is that upon aging within the miscibility gap, a separation of the microstructure into Mn-enriched and Mn-depleted regions occurs [Ref. 24-30,32,33]. Therefore, depending on the aging treatment, it would be expected that upon subsequent cooling the Mn-enriched regions could undergo the magnetic and lattice transitions referred to for quenched homogeneous Mn-rich alloys, but the form which the transformed microstructure would take is not clear. Vintaykin and coworkers [Ref. 32,34] have carried out detailed experiments to monitor the transformation behavior of aged alloys upon subsequent cooling; one of their plots of  $M_s$  versus alloy composition [Ref. 32], for Cu-Mn alloys aged at 400°C for 20 hours, is included in Fig. 1. From this it is clear that the phase separation at a given temperature creates a certain proportion of Mn-enriched microstructure, with the composition determined by the boundary of the miscibility gap at that temperature, and that this Mn-enriched phase indeed displays

a transition temperature on cooling which is characteristic of a homogeneous alloy of the same composition. However, as we will show, an assumption that the resulting microstructure is composed of the same sort of twinned martensitic structure which is seen in quenched homogeneous alloys is neither logical nor true. The present work will show that there is another quite different sort of microstructure which is often created by aging, but which also provides very high damping.

### III. EXPERIMENTAL METHODS

The Cu-Mn-based alloy used in the present research was supplied by the International Copper Research Association in the form of rolled plate. The alloy composition is listed in Table I.

| Table I: Chemical composition of INCRAMUTE (weight percent) |      |      |     |      |      |      |           |
|---|------|------|-----|------|------|------|-----------|
| Cu  | Mn   | Al   | Zn  | Si   | Fe   | Cr   | Remainder |
| 53.1  | 44.8 | 1.61 | 0.1 | 0.08 | 0.06 | 0.05 | 0.2       |

The material was shaped into rods and then cut into discs of 3.0 mm diameter and 0.3 mm thickness. The discs were sealed in evacuated quartz tubes and solution treated at 800°C for 2 hours, then water quenched to room temperature. Individual discs were aged at either 400°C (for periods from zero to 168 hours) or 450°C (for periods from zero to 48 hours). Specimens for transmission electron microscopy (TEM) were prepared with a two-stage procedure consisting of dimpling the discs in a lollipop holder by jet electropolishing with a solution of 50%  $\text{H}_3\text{PO}_4$  and 50%  $\text{H}_2\text{O}$  at room temperature and a current of about 580 ma, followed by final perforation during immersion in a stirred solution of  $\text{H}_3\text{PO}_4$  saturated with  $\text{CrO}_3$  at 8 to 12 VDC and 20 to 30°C. Some of the perforated specimens were cleaned using an ion mill; the samples were bombarded with argon ions accelerated at 5 KV for 1 to 2 hours. Most of the observations were made using a JEOL 100CX microscope operated at 120 KV. A JEOL 200CX microscope was used to observe lattice fringes by means of high resolution electron microscopy (HREM).

Concentrations of copper and manganese at selected sites were measured using an Akashi Beam TEM, model: ABT-EM-002B, equipped with an energy dispersive x-ray (EDX) spectrometer. X-ray spectra were produced at an accelerating voltage of 200 K V with a 2nm diameter electron probe.

Observation of dynamic image behavior was accomplished with a GATAN TEM video imaging system, which employed a YAG transmission scintillator directly linked to a charge coupled device via a fiber optic plate. Image resolution with this system is better than 160 line pairs per cm at the YAG screen.



## IV. RESULTS

### A. EARLY STAGES OF AGING

#### 1. "Mottled" Contrast Microstructures

Solution-treated samples which were not aged at all, or which were aged only very slightly, exhibited a "mottled" microstructure in the TEM. An example is shown in Figure 2. The term "mottled" has often been used in the past to refer to TEM images which display vague and generally-distributed disturbances to otherwise contrast-free image-fields. This type of contrast is so indistinct that it is often considered unnecessary to even present an example of it. However, "mottled" contrast actually has a definite substructure, which can be revealed at high magnification. In the present case, this substructure takes the form of short, string-like lines of contrast, as described below.

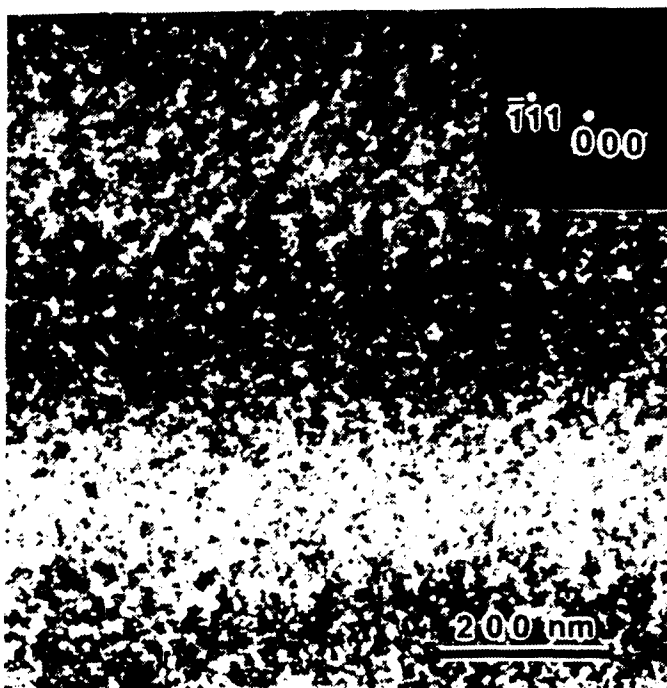


Figure 2: Bright field micrograph from near (110) orientation under two beam condition with  $g=111$ . String shape images are seen in solution treated Cu-Mn-Al alloy.

## 2. "String" Images

The microstructure of the material in the solution treated condition was always similar to that seen in Figure 2, for all thin foil orientations. In high-magnification conventional TEM images of the microstructure, there are numerous short and irregularly curved lines with white or black contrast; hereafter called "string" images. These "string" images are strongly dependent on the orientation of the thin foil, in other words, their appearance changes radically when the operating diffraction vector is changed. When the solution treated alloy was aged at 400°C for a short period of time, the string images appeared to lengthen and assume certain preferred orientations; for example, after 2 hours aging at 400°C, the length of the string images is from 40 to 160 nm.

## 3. "Tweed" Contrast

After aging at 400°C for periods longer than about 4 hours, a "tweed" contrast appears in the microstructure which is observed in the TEM, as exemplified by the image shown in Figure 3, taken from a sample aged for 8 hours. The micrograph of Figure 3 was taken with  $g = \bar{2}20$  at a foil orientation close to (110). Careful inspection shows that the tweed striations in the image are composed of an assembly of string images, with the net striations lying along the traces of {110} planes. Additionally, some string images connect different striations by running at angles

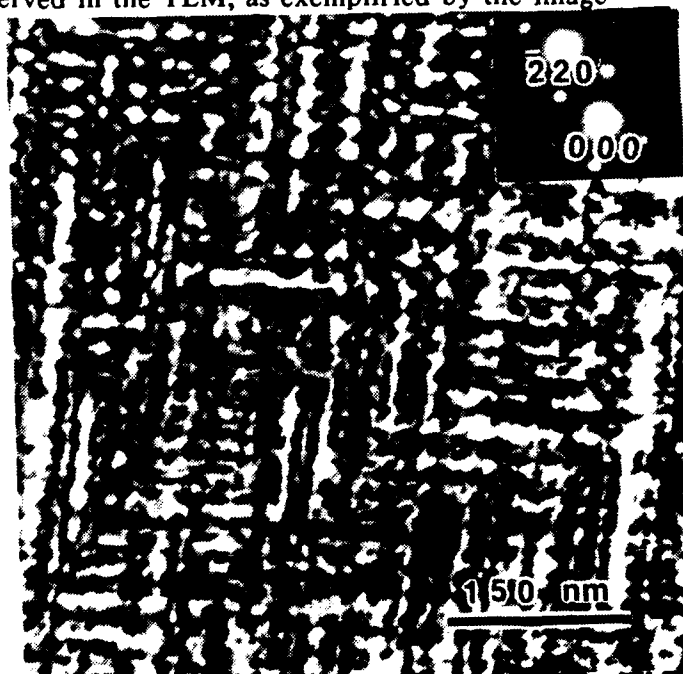


Figure 3: Tweed structure in Cu-Mn-Al alloy aged at 400 °C for 8 hours. Tweed striations lie parallel to traces of {110} planes and consist of bright string images.

between them. The prominent aligned striations are spaced approximately 18nm apart; however the exact spacing varies with crystal orientation and the operating diffraction vector.

The character of tweed contrast microstructures in the present samples may be summarized as follows:

**a. (100) Orientation**

In crystals with (100) orientation, striations in the  $[022]$  and  $[0\bar{2}2]$  directions are observed for  $g=002$ ; thus the striations are consistent with traces of the two sets of edge-on  $\{110\}$  planes. No striations are seen in the directions of the traces of inclined  $\{110\}$  planes. For  $g=022$  or  $g=0\bar{2}2$ , striations normal to  $g$  vanish, while those parallel to  $g$  remain visible.

**b. (110) Orientation**

In crystals with (110) orientation, striations are observed in the  $[1\bar{1}1]$  and  $[\bar{1}11]$  directions for  $g=002$ ,  $2\bar{2}0$  or  $\bar{1}13$ ; in this case, the striations correspond to the traces of inclined  $\{110\}$  planes. For  $g=1\bar{1}1$  or  $g=\bar{1}11$ , only the striations parallel to  $g$  appear; those normal to  $g$  vanish.

**c. (111) Orientation**

In crystals with (111) orientation, striations appear in the two  $\langle 2\bar{4}2 \rangle$  directions which are not normal to the operating vector when  $g=0\bar{2}2$ ,  $\bar{2}02$  or  $2\bar{2}0$ . These striations correspond to the traces of edge-on  $\{110\}$  planes. No striations parallel to the traces of the inclined  $\{110\}$  planes are seen.

**4. Streaking in Diffraction Patterns**

For short aging times, the most instructive information to be gained from the selected-area electron diffraction patterns (SAEDPs) is contained in the details of the streaking and elongation of certain spots. A representative collection of SAEDP's is

presented in Figure 4a, b & c, all taken under near-Bragg conditions from orientations of (100), (110) and (111) from samples solution-treated at 800°C for 2 hours. These patterns are over-exposed to reveal diffuse scattering. It should be noted that faint ring patterns, and in some cases extra spots, are superimposed on the normal SAEDP of the material, due to the formation during electropolishing of a thin

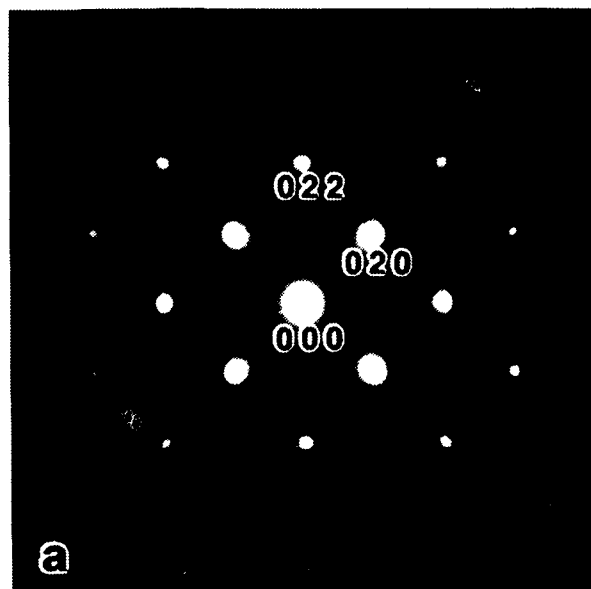


Figure 4a: SAEDP from solution treated Cu-Mn-Al alloy with (100) orientation shown.

contamination layer on the surface of the thin foils. This artifact was unavoidable, and required particular care in the interpretation of the patterns.

Diffuse streaks are detectable on individual reciprocal lattice spots. For example, close examination of the original plate of Figure 4a reveals very weak streaks extending in the  $[022]$  and  $[0\bar{2}2]$  directions and slight elongation in the  $\langle 004 \rangle$  directions of the  $[004]$  and  $[040]$  spots. Weak streaks are also seen in the  $[2\bar{2}4]$  and  $[\bar{2}24]$  directions in Figure 4b. In Figure 4c, diffuse streaks can be clearly seen extending in the  $\langle \bar{4}22 \rangle$  directions. Diffuse spots are observed at the intersection of streaks extending in  $\langle \bar{4}22 \rangle$ , as for example at the intersection of

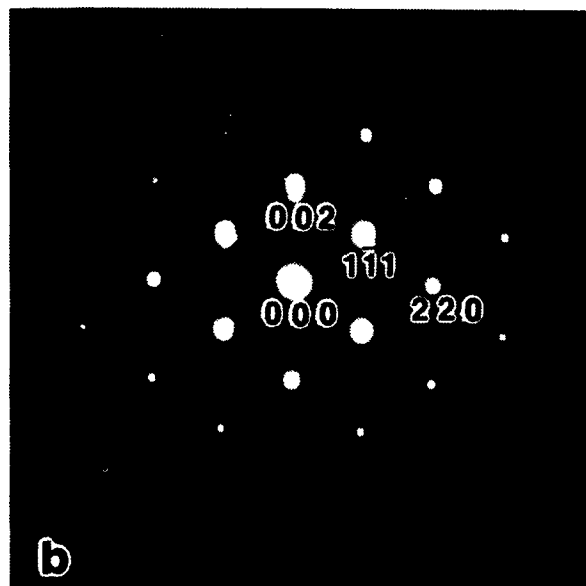


Figure 4b: SAEDP from solution treated Cu-Mn-Al alloy with (110) orientation shown.

the  $1/3\langle\bar{4}22\rangle$  streaks and  $2/3\langle\bar{4}22\rangle$  streaks. No streaks can be seen in the  $\langle 220\rangle$  directions. All of this streaking and elongation of spots is consistent with the existence of  $\langle 1\bar{1}0\rangle^*$  rel rods.

The streaking described above does not appear to change significantly with aging. The SAEDPs taken from samples aged at  $400^\circ\text{C}$  for periods from 2 to 20 hours are similar to those in Figure 4. The

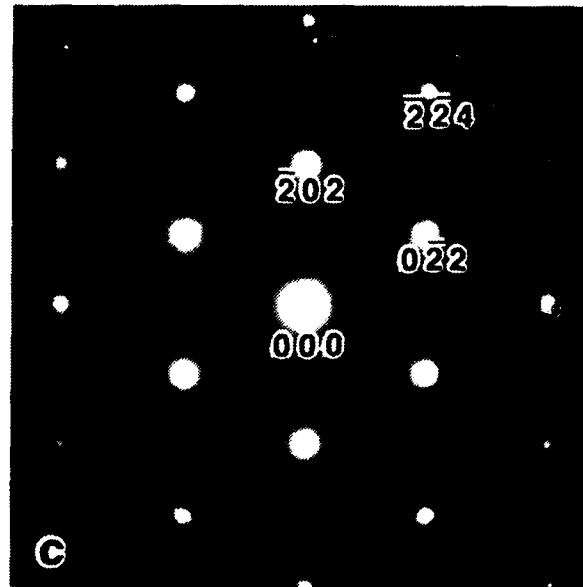


Figure 4c: SAEDP from solution treated Cu-Mn-Al alloy with (111) orientation shown.

SAEDPs associated with  $g$  vectors which caused extinction of striations in the tweed microstructure do not exhibit streaking in the direction perpendicular to the missing striations. There was no observation of satellites to diffraction spots under any diffraction conditions. The streaking and elongation of  $[004]$  and  $[040]$  spots also corresponds to  $\langle 110\rangle$  rel rods in aged samples. It should be noted that the  $\langle\bar{4}22\rangle$  streaking in the (111) orientation is much stronger than the streaking observed in the (110) and (100) orientations.

## 5. "Tweed Bands"

Under certain conditions of aging, diffraction contrast and sample preparation, "tweed bands" are observed, these being linear features superimposed on and aligned with one of the prominent traces of the conventional tweed contrast, as in the example of Figure 5; the tweed bands can be seen in the thin region on the right side while the tweed structure alone is seen in the thicker region on the left side. A tweed band consists of an apparent consolidation of the contrast of a number of parallel tweed striations. The contrast of a tweed

band is strongly dependent on orientation. The width of a typical tweed band varies from several tens to several hundreds of nm and for a given band the width becomes smaller with decreasing foil thickness.

The tweed bands exhibit an extinction behavior which is similar to but not identical with that of the conventional tweed contrast.

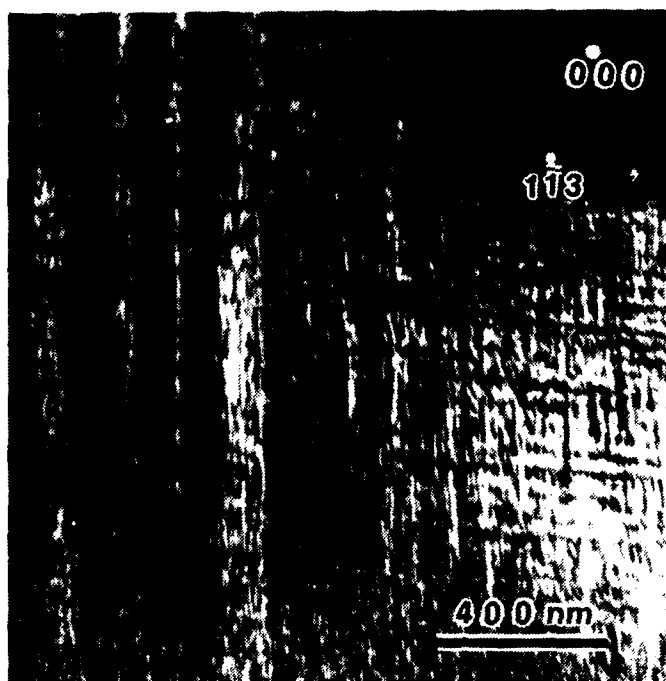


Figure 5: Tweed bands on the left side and tweed structure on the right side. Crystal orientation is (110),  $g = 1\bar{1}3$ .

One example of tweed band extinction is shown in Figures 6a & b, which were taken from a (100) crystal orientation. The sample was aged at 400°C for 10 hours and its surfaces were cleaned by argon ion bombardment after electro-polishing. For  $g=002$  (as shown in Figure 6a), or for  $g=020$ , the tweed bands in the  $[022]$  and  $[0\bar{2}2]$  directions which are parallel to the traces of  $\{110\}$  planes can be observed. For  $g=0\bar{2}2$  (as shown in Figure 6b, or  $g=\bar{0}22$ , the tweed

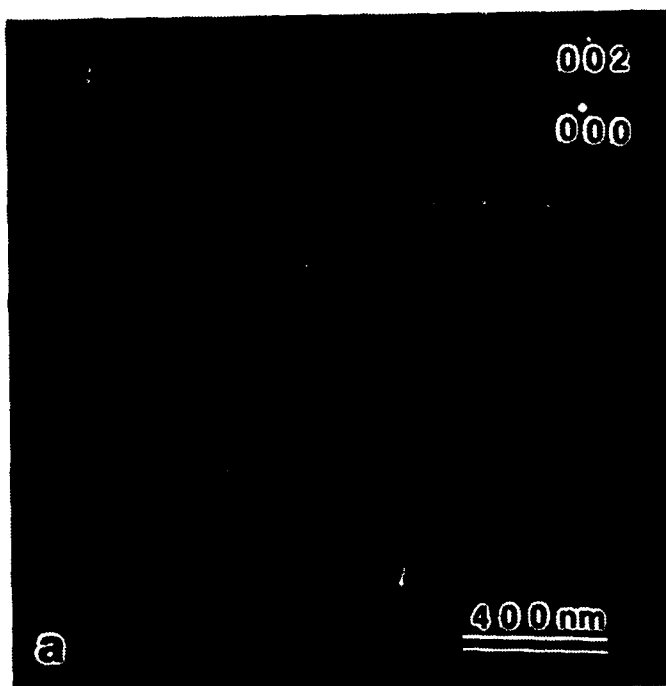


Figure 6a: Tweed bands in a crystal with (100) orientation.  $g = 002$ .

bands parallel to  $g$  appear. This indicates that the atomic displacements responsible for the tweed bands lie in the  $\{110\}$  plane normal to  $g$ . Tweed band extinction conditions in the  $(100)$  crystal orientation match tweed structure extinction conditions in the  $(100)$  crystal orientation.

In a crystal with a  $(110)$ -type orientation, the tweed bands

always appear parallel to the traces of inclined  $\{110\}$  planes, specifically in  $[\bar{1}11]$  and  $[1\bar{1}1]$  directions; this obtains for many different reflections, including  $g=\bar{2}20$ ,  $002$ ,  $\bar{1}11$  and  $1\bar{1}1$ . An example is shown in Figure 7, where  $g=1\bar{1}1$ . This set of results is quite different from that for the conventional tweed contrast, in which only the striations parallel to  $g$  appear. Thus the tweed bands do not follow exactly the same extinction rules as the tweed structure in the  $(110)$  crystal orientation. Therefore the

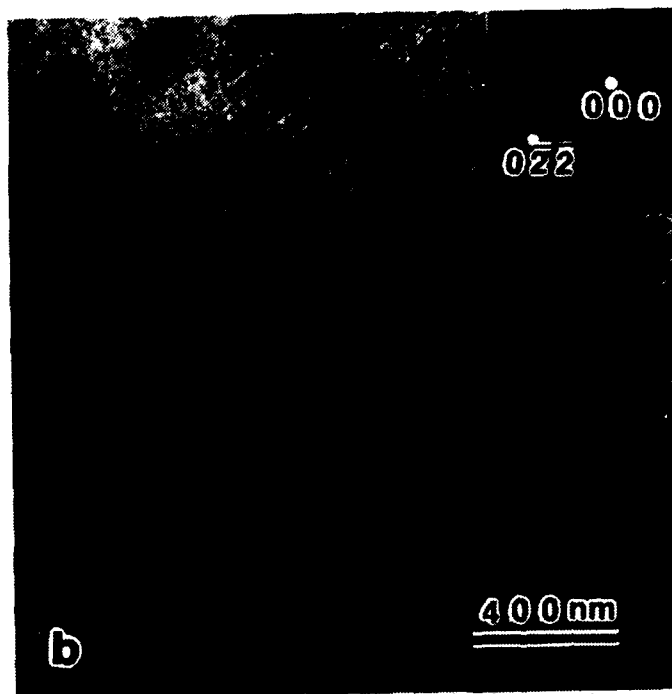


Figure 6b: Tweed bands in a crystal with  $(100)$  orientation.  $g = 022$ .



Figure 7: Tweed bands appear in two directions parallel to traces of inclined  $\{110\}$  plane,  $(110)$  orientation,  $g = 1\bar{1}1$ .

atomic displacements which give rise to the tweed bands cannot be concluded to be simply strains in the  $\langle 1\bar{1}0 \rangle$  directions which lie in  $\{110\}$  planes. In crystals with  $(111)$ -type orientations, tweed bands are observed parallel to the traces of  $\{110\}$  planes which are inclined to the crystal surface, as well as those which are perpendicular. Their directions are therefore in the  $\langle 2\bar{2}0 \rangle$  and  $\langle 2\bar{2}4 \rangle$  directions. From the overall set of extinction observations for the tweed bands, the actual atomic displacement direction has yet to be determined.

## **6. "Flickering Contrast"**

In the course of examination of the tweed microstructures in this alloy over a range of aging conditions, a remarkable and unexpected observation was made, one which has not been reported previously in Cu-Mn or any other tweedy alloy. It was vividly apparent on the viewing screen of the TEM that the tweed contrast microstructure was not completely static. Rather, when the tweed contrast was observed at a sufficient magnification (say 40,000X or so), certain specific points within it were observed to be "flickering". This effect was not observed in samples at early aging times, when the samples displayed simply a "mottled" microstructure, but only after the aligned tweed traces became evident (in the present study, corresponding to aging times of 4 hours or longer at 400°C).

The "flickering" effect consists of spatially consistent and repetitive contrast variations, that is, only certain points flicker, and the contrast variation is always very much the same in nature (although the frequency is variable). Not all of the microstructure changes contrast, just certain small regions. The regions which flicker are on the scale of the tweed trace spacing, around 10 nm or so. Upon close examination, it is apparent that the contrast variations are not of an "on-off" nature, but rather involve short movements or rotation of lines of contrast on about this scale. For example, a short (say 10 nm) black-



white linear contrast may suddenly jump a distance of 5 to 10 nm, or (in another case) may rotate through an angle. At any given location, the movement is cyclic and consistent. The frequency is variable at any given location, but is in the range of 0.1 Hz to 10 Hz.

In Figure 8, just a few of the many active areas are indicated. Because there are a great many of these regions active on the imaging screen at any one time, it is difficult to obtain a complete quantitative characterization of the activity. Also, the moving image presents certain problems in photographic recording by the usual methods, but videotape records have been made [Ref. 77]. In some cases, static exposures do reveal, in blurred form, the movements of lines of contrast described above, if one knows what to look for. The most successful method of recording the activity at individual locations was the use of weak beam techniques, an example of which is

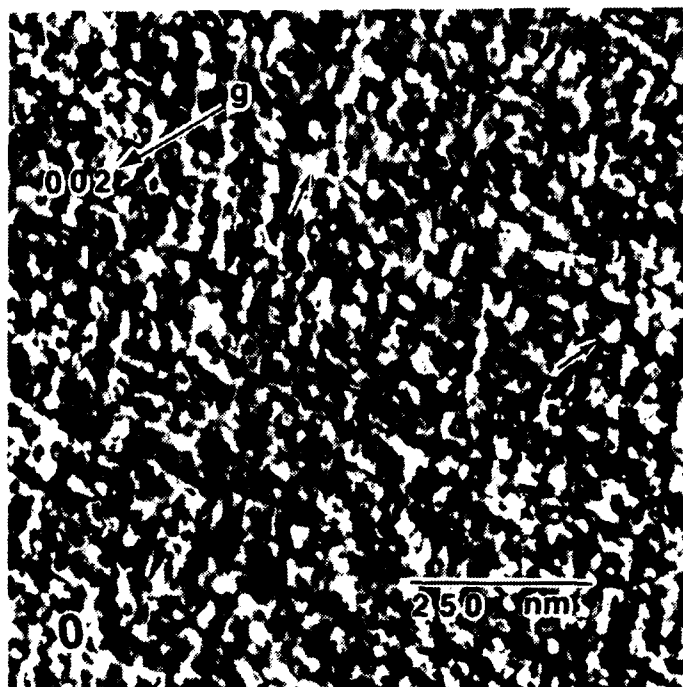


Figure 8: Aged 22 hour at 400 ° C; some of the blurred flicker points are marked with arrows; dark field image,  $g=002$ .

shown in Figure 9a & 9bcd; using this method, it becomes apparent that the contrast has a very specific geometric form, which includes one or more distinct V-shaped angles; this is shown enlarged in Fig. 9d.

Flickering contrast has been carefully studied as a function of specimen temperature and beam current. Flickering is observed to disappear above a certain critical

temperature, which is around 70°C; this is assumed to approximate the FCT-to-FCC transition temperature in the aged alloys.

## 7. High Resolution TEM

In order to further investigate the flickering contrast, lattice fringes from (100) and (110) crystals were studied in regions of samples that showed tweed structure

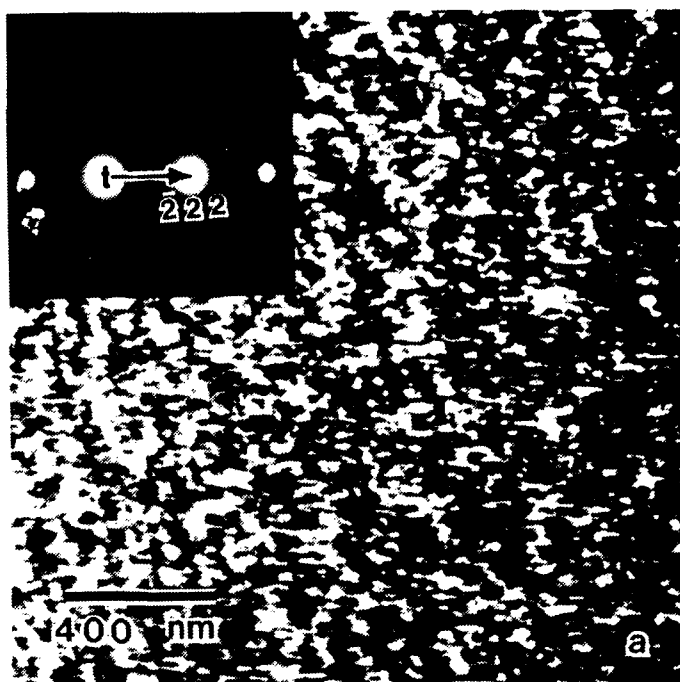


Figure 9a: Aged 10 hours at 400°C; bright field image,  $g=\bar{1}11$  this area used to obtain the weak beam images of Fig. 9bcd.

and flickering. Surface contamination of the electro-polished samples allowed examination

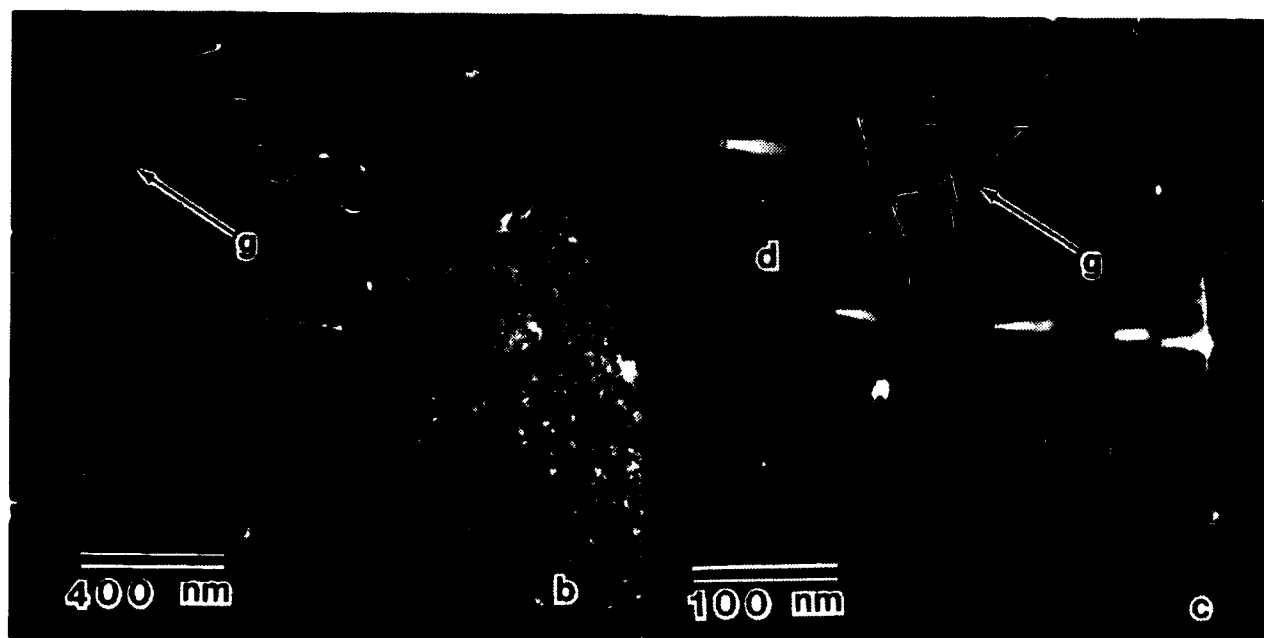


Figure 9bcd: (b) Weak beam image area shown in Fig 9a, individual flicker events are recorded; (c) enlargement of 9b; (d) inset, enlarged further, revealing a V-shaped geometry in the contrast.

of only the  $(\bar{1}11)$  lattice fringes with 0.22 nm spacing and the (002) fringes with 0.19nm spacing. An example is shown in Figure 10, obtained from a (110) crystal aged for 8 hours at 400°C and imaged with the  $\bar{1}\bar{1}1$  and  $1\bar{1}\bar{1}$  reflections, which were the strongest and next strongest reflections in the pattern. The  $(\bar{1}11)$  lattice fringes are seen. No domains where FCT martensite exists can be found and no twin with a  $\langle 111 \rangle$  twin axis can be observed.

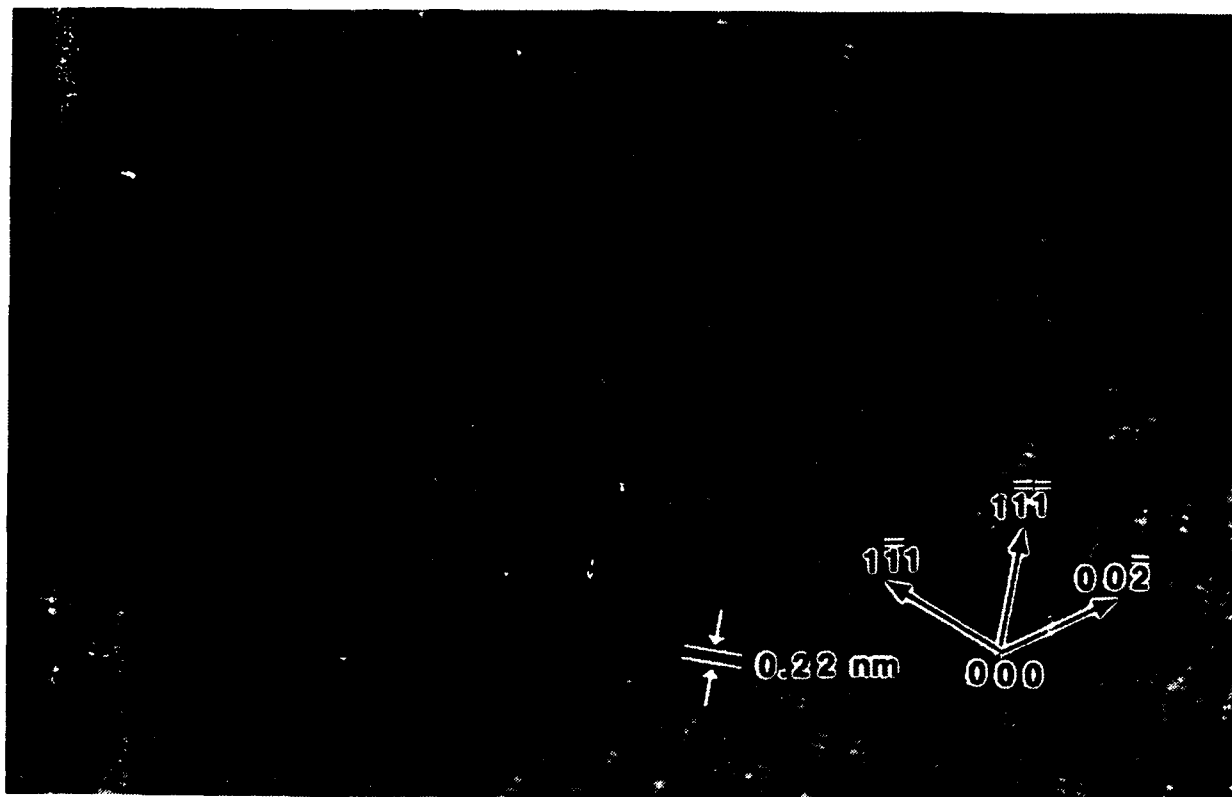


Figure 10:  $(\bar{1}11)$  lattice fringes of (110) crystal orientation. In the thicker region tweed structure and flickering were observed.

## B. LATER STAGES OF AGING

### 1. Reduction in "tweed" contrast

In the present work, the microstructure of aged samples was studied in two time series, one at 400°C, the other at 450°C. Tweed contrast was seen in all alloys aged at 400°C for up to about 22 hours, or at 450°C for up to about 10 hours. The wavelength of the tweed

contrast, i.e. the spacing of the most apparent striations, gradually increases with aging time at a given temperature. Eventually, the distinction of the striations begins to diminish. When the tweed contrast diminishes, it is replaced by a set of more discreet and obvious regions of contrast, which are believed to be a dispersion of small FCT crystallites in an FCC matrix. For example, in the early stages of aging at 450°C, the tweed structure of Figure 11 was observed; as usual, the trace of the striations is consistent with the traces of {110} planes.

However, at aging times longer than about 5 hours the striated tweed contrast is diminished, although it is still visible to some extent, and a new form of distinct contrast develops, namely a set of discreet regions which contain V-shaped and dash-shaped contrast features, as in Figure 12. The angular features obviously adopt a variety of multiple V-shapes, often appearing as W-shapes and so forth.

All of these features are interpreted as being sets of very small and variously oriented FCT crystallites.

## 2. "V-shaped" contrast

The V-shaped images which develop at longer aging times are located in discreet regions which are roughly spherical in shape, as shown in Figure 13. These rounded regions are themselves best seen under slightly out of focus conditions in the TEM. The size of these

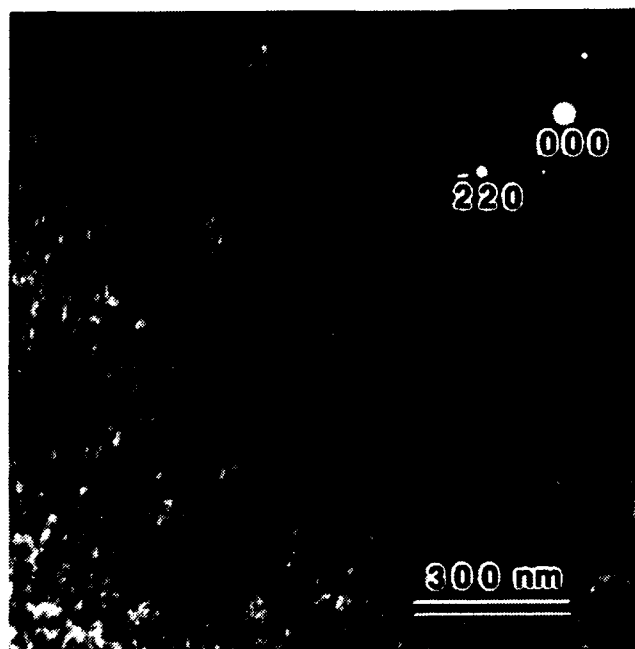


Figure 11: (110) crystal orientation. 450 °C, 3 hr age,  $g = \bar{2}20$ . In the thicker region tweed structure and flickering were observed.

regions is on the order of 20 to 60 nm. The number density of them increases with aging time. The contrast of the rounded regions is usually quite complex. Overlapped images and Moire patterns are among the features which can be discerned. The V-shaped features are best seen when the sample is tilted into a two-beam in-focus condition. Therefore, either the

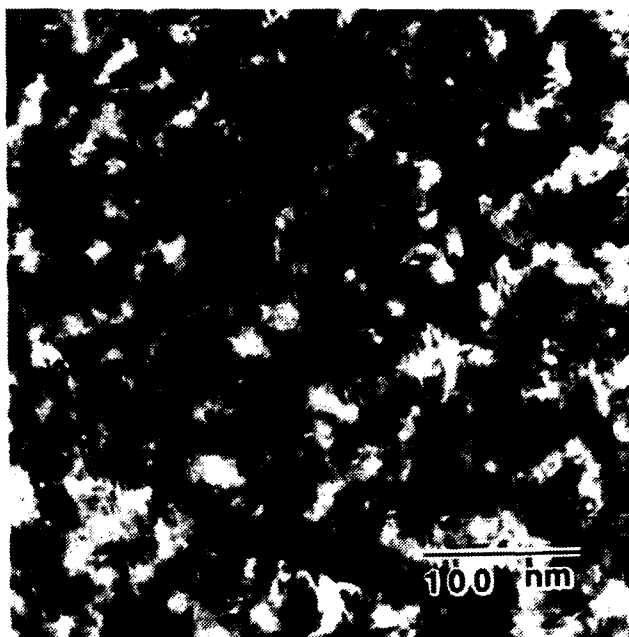


Figure 12: Static and flickering zig-zag groups in sample aged 10 hours at 450 ° C. Beam direction close to  $\langle 100 \rangle$ . Bright field image.

rounded regions or the V-shaped features within them can be imaged, depending on the particular combination of specimen orientation and focus.

One feature of the microstructure seen in Fig. 12 which is different than say, that of Fig. 2, is a less defined pattern of the  $\{110\}$  tweed traces. Close examination reveals that the less defined pattern of tweed traces is due to the fact that the features underlying (and causing) the tweed contrast are somewhat larger and not so finely dispersed. In other words, the

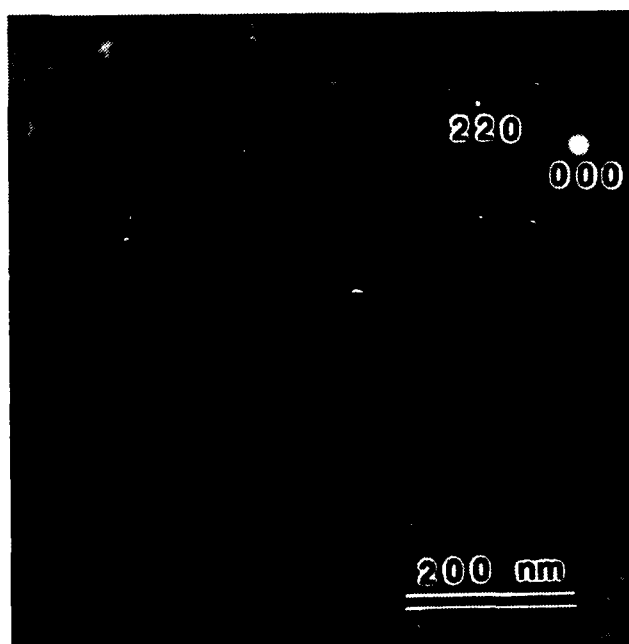
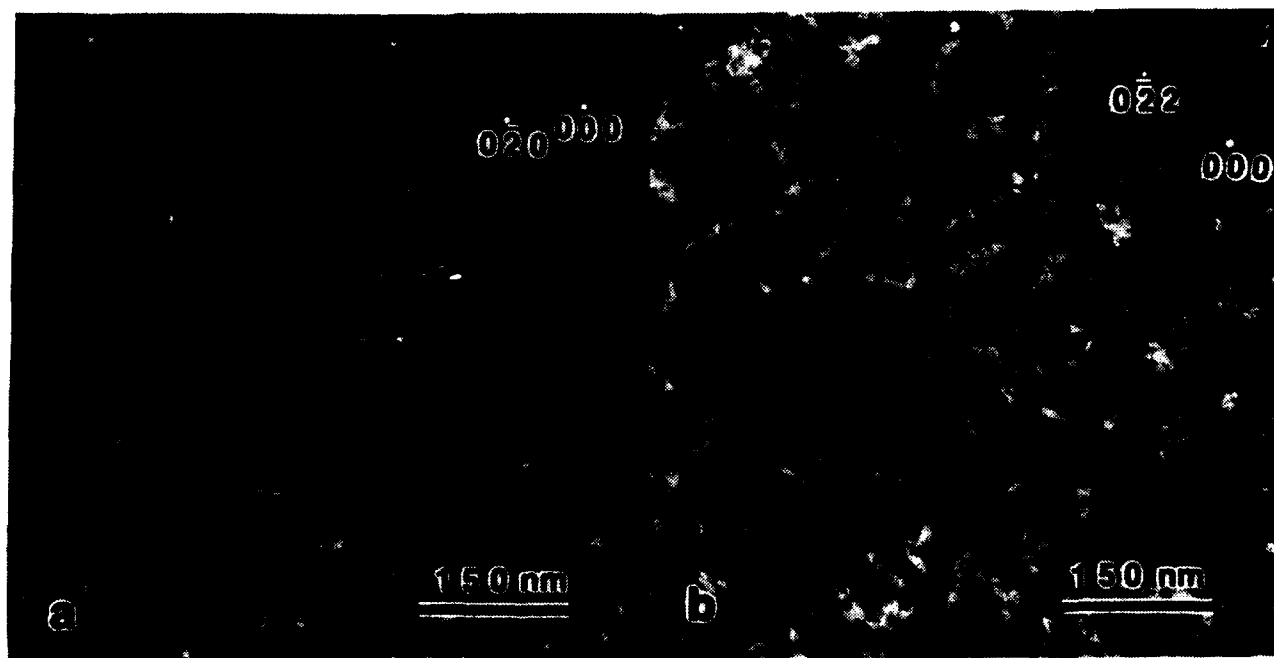


Figure 13: Round shaped images seen in a crystal aged at 450 ° C for 10 hours.

dispersed centers of asymmetric strain on which the tweed contrast depends have become further apart as the aging has progressed, which presumably leads to less interaction between the strain fields of neighboring regions and thus a loss of the tweed-producing mechanism.

In a crystal with (100) orientation and aged at 450°C for longer than about 5 hours, V and W shaped images with a size of about 35 to 55 nm are observed. The angles between the sides of the V-morphology are difficult to define with any accuracy; they appear to range from 17° to 31°, and while it is suspected that there is a unique angle within this range, strain contrast effects and the very short length of the traces makes the measurement of the angle extremely difficult. Examples of electron micrographs for samples aged at 450° C for 10 hours are shown in Figures 14a and 14b. When  $g=002$  or  $g=020$ , the



**Figure 14:** V-shaped images, crystal in (100) orientation. a: images directions  $[022]$  and  $[022]$ , b: image direction  $[0\bar{2}2]$ .

bisectors of the V-angles lie in the directions  $[022]$  and  $[0\bar{2}2]$ , as shown in Figure 14a, where  $g=002$ . When  $g=0\bar{2}2$  or  $g=022$ , only the images parallel to  $g$  appear, as shown in Figure 14b.

For (110)-type orientations of the foil, V-shaped and dash-shaped images lying in the  $[\bar{1}\bar{1}1]$  and  $[\bar{1}11]$  directions are visible for  $g=002$  or  $g=2\bar{2}0$ . An example is shown in Figure 15a, where  $g=2\bar{2}0$ . When  $g=1\bar{1}1$  or  $g=\bar{1}11$ , the images parallel to  $g$  are visible, as shown in Figure 15b where  $g=1\bar{1}1$  and the image direction is also  $[\bar{1}\bar{1}1]$ . For (111)

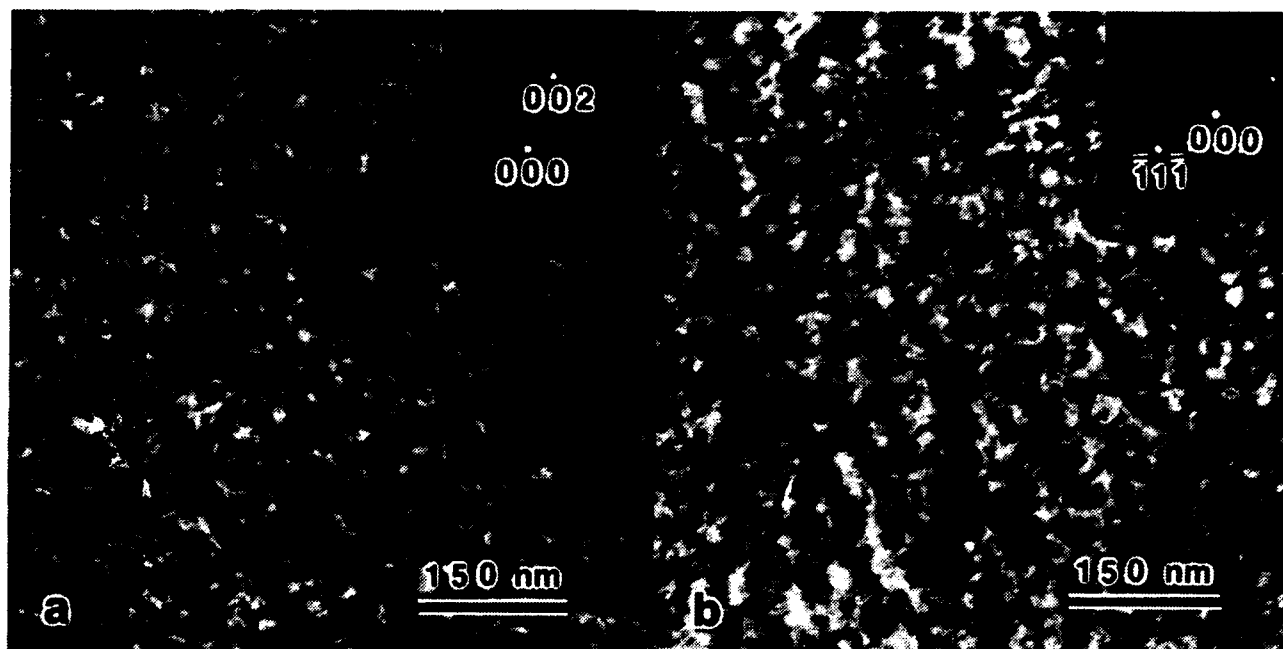


Figure 15: V and dash-shaped images, crystal orientation (110). a:  $g=2\bar{2}0$ , b:  $g=1\bar{1}1$ .

orientations, V and dash-shaped images were observed in  $\langle\bar{4}22\rangle$  directions when  $g=0\bar{2}2$  or  $g=4\bar{2}2$ .

The extinctions of the V-images satisfy the same rules as for the tweed structure [Ref. 78,79]. The atom displacements for V and dash-shaped images are therefore concluded to be in  $\langle 1\bar{1}0\rangle$  directions on (110) planes. It should be noted that the FCT crystallites which give rise to the V-shape images are located in regions which have been enriched in

manganese by the aging process, as will be proved later on. The V-images are seen by matrix strain contrast. It is thus concluded from the directions of the images in (100), (110) and (111) planes and the directions of tweed structure (parallel to the traces of {110} planes) that the center lines of the V-shaped images and the direction of the dash-shaped images are in  $\langle \bar{1}11 \rangle$  directions in the matrix crystal.

### 3. "Flickering" of V-shaped contrast

The V-images also display a distinct flickering behavior. For example, a group of V-images which are pointing in one direction may be observed to execute an abrupt rotation to another direction of pointing. The contrast variation in a given region exhibited a consistent pattern. A common pattern was an abrupt rotation of approximately 90 degrees of a small zig-zag group or of a short line (or pair of lines) of contrast. For example, the V-points in a zig-zag group, or the alignment of the short lines of contrast, would suddenly switch back and forth from pointing along one or the other of the two orthogonal (110) tweed traces.

The dynamic behavior of the flickering activity was observed and recorded with a video system. A schematic diagram for  $g=022$  and a (100) crystal orientation are shown in Figure 16. In this case all of the flickering images show displacements parallel to the  $g$  vector. The pictures (a-i) on the upper line indicate the original image (before the contrast change). The pictures on the lower line show the image shape after the contrast change, with a superimposed dashed line showing the original image. In each case the flickering cycle is completed by a contrast shift back to the original image. The arrows, one or two headed, indicate the directions of motion of the image during the contrast change of the particular mode of flickering.



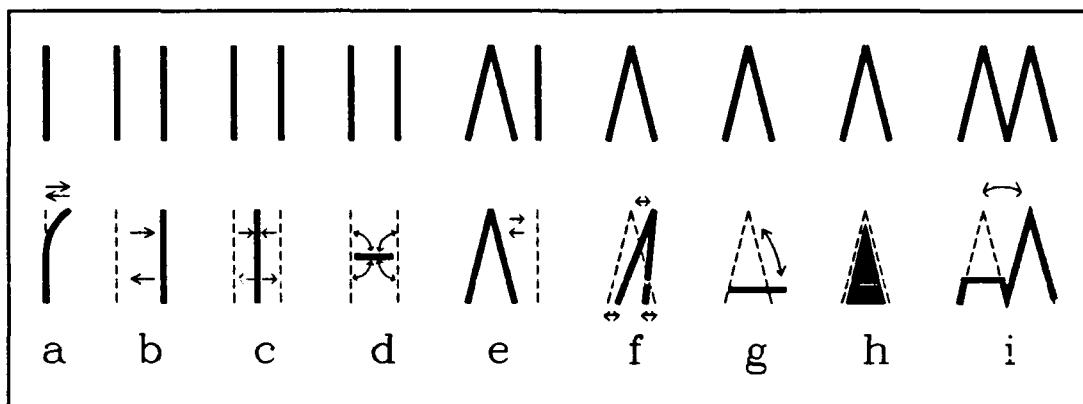


**Figure 16:** Schematically diagram of flickering for  $g = 022$  reflection,  $(100)$  crystal orientation. Upper images; before contrast change, Lower images; after contrast change.

Actually, there are a number of different modes of flickering, as illustrated in Figures 16. In Figures 16a & 16i only one part of the image moves. In Figures 16b & 16e one image moves to the other to coalesce and then moves back to the original position. Figures 16c and 16d show two images moving to an intermediate position to coalesce and then moving back to their original position. Figures 16f & 16g show V-shaped images vibrating from one orientation to another while Figure 16h shows a reversal of contrast inside the images without orientation change. Figures 16d & 16g are especially interesting in that the coalescent images lie normal to the original and thus to  $g = 022$ . This implies that the atomic displacements for the coalescent images are the same as for the original images. In Figures 16d and 16g, there is a 90 degree change of orientation of the V-shaped features; in Figure 16h there is a change of contrast within a given V-shaped image. Some of the V-image groups remain static, i.e. do not flicker.

Flickering of the V-images was prominent in the temperature range between -160°C and 70°C. As is the case with flickering within the conventional tweed contrast, the flickering of the V-images diminishes significantly above about 70°C. The flickering behavior was affected by the intensity of the incident electron beam; at increased electron

beam intensity, the frequency of flickering increased. At a typical flickering site a visible change of contrast took place between one and several times per second. During observation of a given field of view on the TEM screen, a number of previously quiescent sites would typically begin to flicker and at the same time certain sites that were initially flickering would become quiescent.

#### 4. Diffraction Results at Longer Aging Times

Samples aged at 450°C for 3 hours exhibited tweed structure and showed very weak streaks and no satellites to diffraction spots in their SAEDPs. Tweed structure was observed in all sample orientations except (111) and the SAEDP of the (111) orientation was similar to that shown in Figure 17c. When aged at 450°C for 10 hours, the tweed structure vanished and small V shaped images appeared. The SAEDPs associated with the V shaped images show more pronounced streaking and diffraction spot satellites. Example SAEDPs taken at the Bragg position for a sample aged at 450°C for 10 hours are shown in Figures 17a, b & c. Figures 17a' & b' are taken at the same orientation at 17a & b, but under tilting conditions.

In the (100) orientation short, weak streaks are seen in the  $\langle 220 \rangle$  direction at every diffraction spot, including the incident beam spot (Fig. 17a). When the specimen is tilted to a

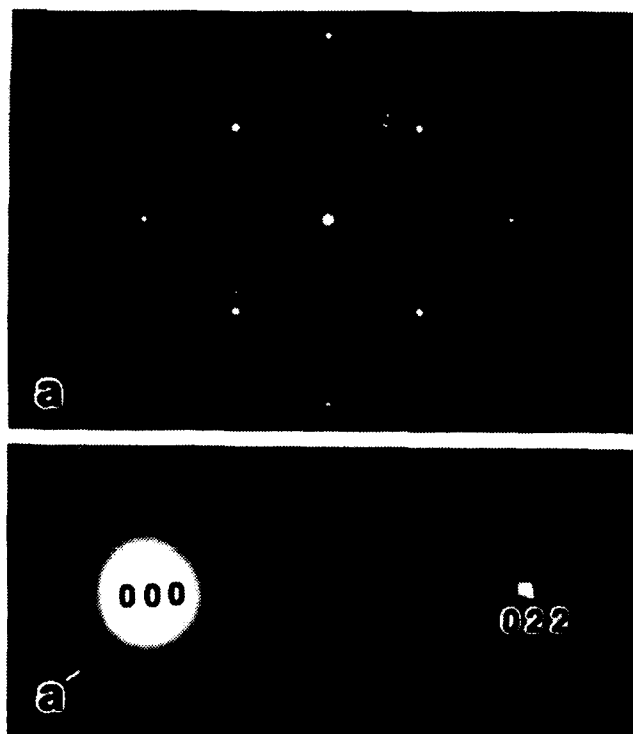


Figure 17a & a': SAEDP for sample aged at 450°C for 10 hours, (100) orientation. a: Near Bragg condition. a': Under tilting conditions.

slightly out of Bragg condition, satellites appear in the  $\langle 002 \rangle$  directions (Fig 17a').

In the (110) orientation there are weak streaks in the  $\langle \bar{4}22 \rangle$  directions at every diffraction spot (Fig 17b). When tilted away from exact (110) orientation satellites appear in  $\langle \bar{4}22 \rangle$  directions (Fig 17b').

In the (111) orientation streaks are observed in the  $\langle \bar{4}22 \rangle$  directions and the streaks have diffuse spots at their intersections (Fig. 17c). The (111) SAEDP for the sample aged at 450°C for 10 hours is quite similar to the (111) SAEDP for the solution treated alloy.

All of the streaks and satellites described above correspond to  $\langle 110 \rangle^*$  rel rods. These rel rods are associated with  $\{110\}\langle \bar{1}10 \rangle$  static displacement waves.

### 5. Trace Analysis and Extinction Behavior of the V-contrast

Detailed analysis of the tweed contrast in numerous systems, such as aged Fe-Pd alloys [Ref. 78], and

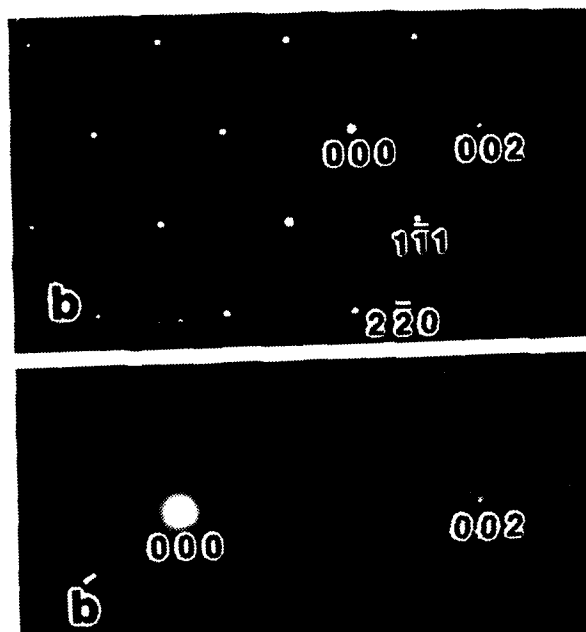


Figure 17b & b': SAEDP for sample aged at 450°C for 10 hours, (110) orientation. b: Near Bragg Conditions. b': Under Tilting Conditions.

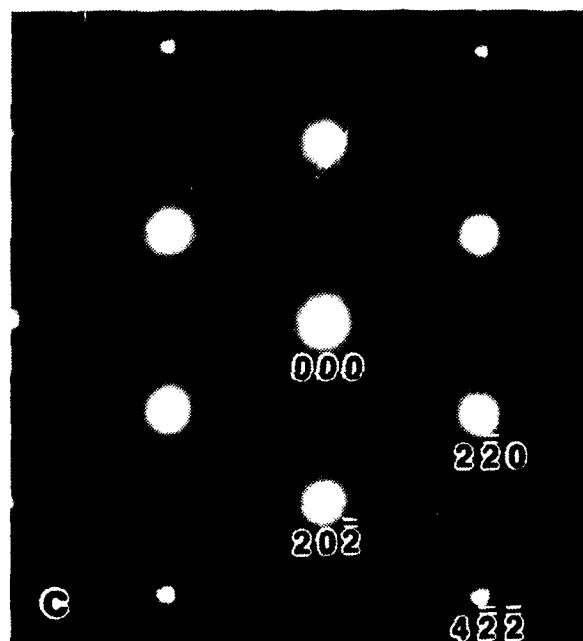


Figure 17c: SAEDP for sample aged at 450°C for 10 hours, (111) orientation. Taken at Bragg condition.

aged Cu-Zn alloys [Ref. 80], has revealed that the lines of contrast (the tweed "striations") typically lie along traces of  $\{110\}$  planes of a cubic phase, and obey extinction rules which are consistent with them being due to underlying net  $\langle 110 \rangle$  shear distortions of  $\{110\}$  planes.

In the present case of well-aged Cu-Mn alloys, the tweed contrast is largely supplanted by a localized V-shaped contrast, but the dominant image axis of the V-shaped morphology also lies along traces of  $\{110\}$  planes, ie., along the same traces which (at shorter aging times) were defined by the tweed striations. This is clear in the time-exposed photograph, taken from the  $(100)$  image plane, which is presented as Figure 18. The V-shapes often appear in parallel clusters, with adjacent V's pointing in opposite directions, forming a sort of zigzag pattern. In this case, the zigzag image contrast resembles a miniaturized group of self-accommodating crystal units, a

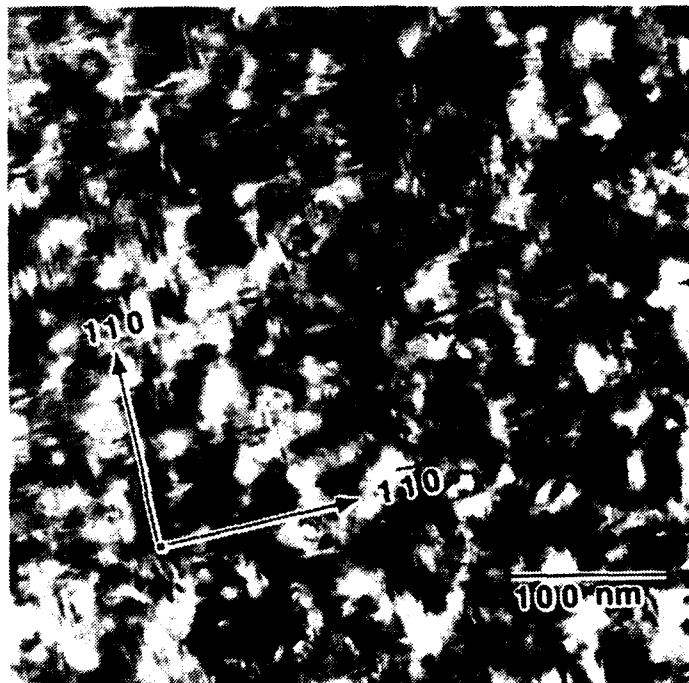


Figure 18: Alloy aged 10 hours at 450 °C.  $(100)$  image plane illustrating V-shaped images lying parallel to traces of  $\{110\}$  planes.  $g = 002$ .

morphology which is well-known in thermoelastic martensites.

The V-shaped images display extinctions similar to those ascribed to tweed contrast by Robertson and Wayman [Ref. 81-83] indicating that static displacements within the matrix give rise to the observed V-shaped contrast. Accordingly, it was possible to

determine the direction of shear displacements producing the images. In this analysis two possible static displacement directions were assumed:

$$R = \delta\{110\}/\langle 110 \rangle \quad \text{and,} \quad R = \delta\{110\}/\langle 111 \rangle,$$

where  $\delta$  is the atom displacement. The magnitude of atom displacement considered (from its perfect lattice position) is very small, corresponding to a small fraction of the interatomic distance.

Stereographic analysis was used to predict image directions for both needles and plates of fct martensite forming on  $\{110\}$  crystal planes in the alloy matrix. Six stereographic projections were prepared, two for each major zone axis (001, 110, and 111) and are included as Figs. 19 to 25. The two projections for each major zone axis include one showing image directions for all possible  $\langle 110 \rangle$  type orientations for both plates and needles. The other shows image direction for all possible  $\langle 111 \rangle$  type orientations for plates and needles.

Figure 19 shows image directions for all possible  $\langle 110 \rangle$  directions on a (001) plane. To determine the possible trace directions for FCT needles, it is necessary to find the pole corresponding to a possible atom displacement direction, say  $[\bar{1}01]$ , then follow the line from that pole through the center pole (marked 001) to the great circle. The intersection of that line with the great circle is the direction of the trace. Arrows

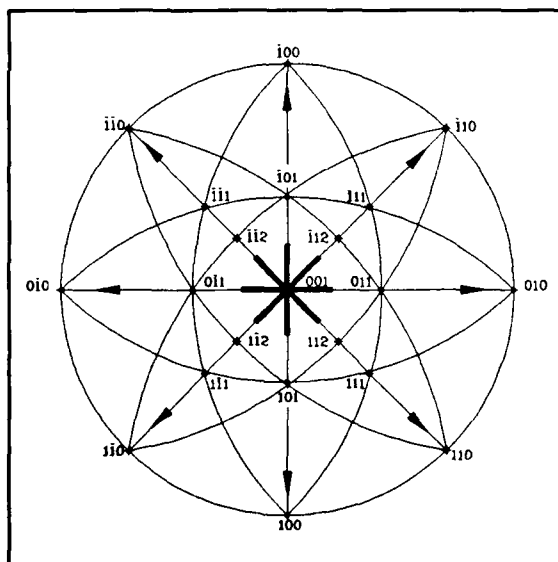


**Figure 19: Stereographic Projection for the (001) zone showing image directions due to  $\langle 110 \rangle$  needles (arrows) and  $\langle 110 \rangle$  plates (thick lines).**

mark all possible trace directions for  $\langle 110 \rangle$  type displacements caused by fct needles on  $\{001\}$  planes.

To find the possible trace directions for FCT platelets, find the pole corresponding to the platelets normal, then follow the line from this pole to the central pole. The line at right angles to the line just followed is the trace direction for this platelet. Heavy lines mark all possible trace

directions for  $\langle 110 \rangle$  type displacements caused by fct platelets.

In the case just examined the directions of traces due to FCT platelets and FCT needles are the same. Examination of Figure 21 shows that the direction of traces due to

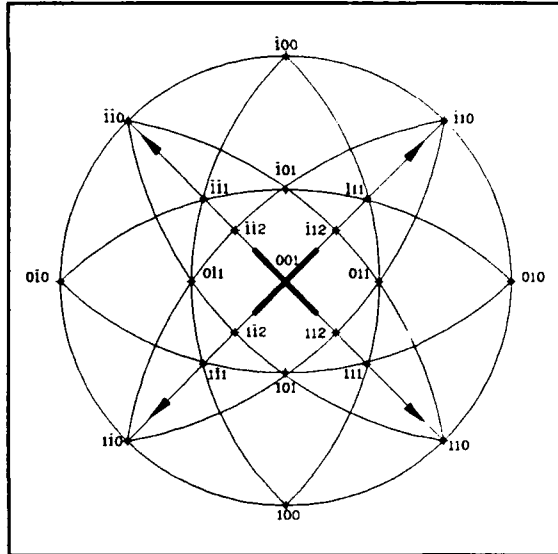


**Figure 20:** Stenographic Projection for the  $(001)$  zone showing image direction associated with  $\langle 111 \rangle$  needles and  $\langle 111 \rangle$  plates.

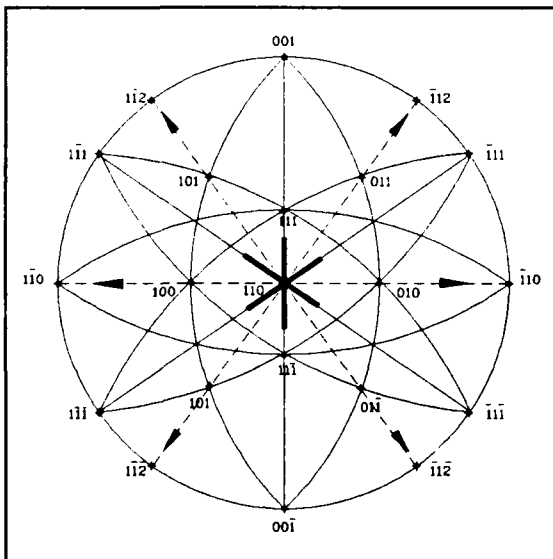


**Figure 21:** Stenographic Projection for the  $(110)$  zone showing image directions for  $\langle 110 \rangle$  needles (arrows) and  $\langle 110 \rangle$  plates (thick lines).

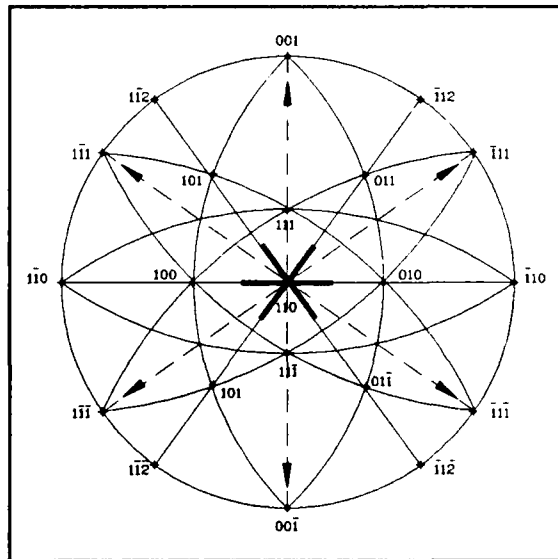


**Figure 22:** Stenographic projection for the  $(110)$  zone showing image directions for  $\langle 111 \rangle$  needles (arrows) and  $\langle 111 \rangle$  plates (thick lines).

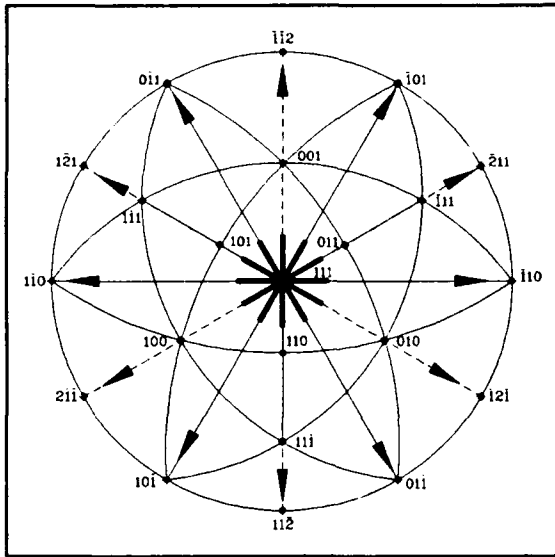


**Figure 23:** Stenographic Projection for the (111) zone showing image directions for  $\langle 110 \rangle$  needles (arrows) and  $\langle 110 \rangle$  plates (thick lines).

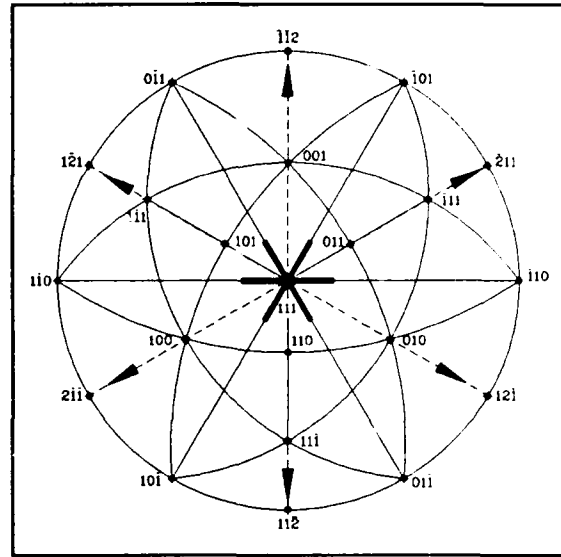


**Figure 24:** Stenographic Projection for the (111) zone showing image directions for  $\langle 111 \rangle$  needles (arrows) and  $\langle 111 \rangle$  plates (thick lines).

FCT platelets and FCT needles do not always correspond. The traces of planes with  $\langle 110 \rangle$  type normals are in  $[001]$ ,  $[\bar{1}11]$  and  $[1\bar{1}1]$  directions. The traces of needles with  $\langle 110 \rangle$  axis directions are  $[\bar{1}12]$ ,  $[1\bar{1}2]$  and  $[001]$  directions.

Figure 25 compares the predicted trace directions for  $\langle 110 \rangle$  needles,  $\langle 110 \rangle$  plates,  $\langle 111 \rangle$  needles and  $\langle 111 \rangle$  plates with the observed trace directions. Examination of this figure shows that the image directions for both  $\langle 111 \rangle$  needles and  $\{110\}$  plates are possible. Since the predicted image directions for  $\langle 110 \rangle$  needles and  $\{111\}$  plates do not contain the observed  $[\bar{1}1\bar{1}]$  or  $[11\bar{1}]$  directions, these shapes are discounted.

A resolution of martensite type and orientation is not possible from this analysis alone, as the observed images are missing some trace directions which would be expected for both  $\langle 111 \rangle$  needles and  $\{110\}$  plates. Additional analysis of V-shaped image extinction data is needed to make the final determination of martensite type.

A strict quantitative analysis of strain contrast requires the use of the dynamical theory of electron diffraction. However, in this case, where the extinction of images is due

| Viewing direction | <110> Needle | <111> Needle | {110} Plate | {111} Plate | Observed |
|-------------------|--------------|--------------|-------------|-------------|----------|
| [001]             |              |              |             |             |          |
| [011]             |              |              |             |             |          |
| [111]             |              |              |             |             |          |

**Figure 25:** Comparison between actual image directions and image directions predicted by stenographic projection. to static displacement,  $\mathbf{R}$ , the use of kinematical theory is sufficient. For a locally distorted crystal, the distortion induces an extra phase factor  $\exp(-i\alpha)$ , where  $\alpha = 2\pi\mathbf{g}\cdot\mathbf{R}$ , and where  $\mathbf{g}$  is the reciprocal lattice vector of the operating diffracted beam in a two-beam condition. This phase factor can essentially be applied to the dynamical theory without change of the expression. The strain field contrast depends on the value of  $\alpha$ , and image extinction occurs when  $\alpha = 0$ . If we exclude the scaling factor  $(2\pi)$  and consider cartesian coordinates,  $\mathbf{g}\cdot\mathbf{R}$  can be written:

$$\mathbf{g}\cdot\mathbf{R} = g_x R_x + g_y R_y + g_z R_z \quad (1)$$

Values of  $\mathbf{g}\cdot\mathbf{R}$  other than 0 may be used to qualitatively indicate the strength of contrast in the directions determined, ie., a value of 4 would produce a "stronger" image than say a value of 2. Thus, it is possible to determine the atomic displacement directions from the extinction rule, where  $\alpha = 0$ , and by assuming that images produced from line features in the crystal are projections on the film plane.



Image extinctions for three low-index crystallographic zones; (001), (011), and  $(\bar{1}\bar{1}1)$ , were predicted for both displacement directions,  $\langle 110 \rangle$  and  $\langle 111 \rangle$ . The predicted image extinctions were then compared with those actually observed in images from a overaged Cu-Mn-Al alloy sample which displayed the V-shaped and zigzag morphologies. In each case a "truth table" of dot products was calculated for  $\mathbf{g} \cdot \mathbf{R}$ , and this product used to predict the expected image axis directions and qualitative contrast intensities. Figures 26, 27 & 28 contain the overaged Cu-Mn-Al (001),  $(\bar{1}\bar{1}1)$  and (011) zone images. Table II contains the tabulated values of  $\mathbf{g} \cdot \mathbf{R}$

Examination of Figure 28, which shows  $\mathbf{g}$  vectors of  $02\bar{2}$ , 200,  $1\bar{1}1$  &  $\bar{1}\bar{1}1$  (a-d) shows two V-shaped image directions. Extinction of one direction of V-shaped image occurs when  $\mathbf{g} = 1\bar{1}1$  and the other direction becomes extinct with  $\mathbf{g} = \bar{1}\bar{1}1$ . This observation agrees with the tabulated values of  $\mathbf{g} \cdot \mathbf{R}$  in Table II  $\mathbf{R} = \epsilon \langle 110 \rangle$  which show the image associated with  $\mathbf{R} = \epsilon[10\bar{1}]$  is missing with  $\mathbf{g} = \bar{1}\bar{1}1$  but present with  $\mathbf{g} = 1\bar{1}1$  while the image associated with  $\mathbf{R} = \epsilon[10\bar{1}]$  is present with  $\mathbf{g} = \bar{1}\bar{1}1$  but missing with  $\mathbf{g} = 10\bar{1}$ . It does not agree with the tabulated values for  $\mathbf{R} = \epsilon \langle 111 \rangle$  which does not show image extinctions (but does show a change in contrast) for those  $\mathbf{g}$  vectors.

| Table II: Tabulation of $\mathbf{g} \cdot \mathbf{R}$    |                   |                       |              |                       |             |              |                   |                       |             |
|--|-------------------|-----------------------|--------------|-----------------------|-------------|--------------|-------------------|-----------------------|-------------|
|  |                   | Observation Direction |              |                       |             |              |                   |                       |             |
|  |                   | $\langle 001 \rangle$ |              | $\langle 011 \rangle$ |             |              |                   | $\langle 111 \rangle$ |             |
| $\mathbf{g} =$   |                   | $\bar{2}20$           | $020$        | $200$                 | $1\bar{1}1$ | $02\bar{2}$  | $1\bar{1}\bar{1}$ | $02\bar{2}$           | $202$       |
| $\mathbf{R} = \epsilon \langle 110 \rangle$<br>(assumed) | $110$             | 0                     | 0            | $2\epsilon$           | 0           | $2\epsilon$  | $2\epsilon$       | $2\epsilon$           | $2\epsilon$ |
|  | $101$             | $-2\epsilon$          | $2\epsilon$  | $2\epsilon$           | $2\epsilon$ | $-2\epsilon$ | 0                 | $-2\epsilon$          | $4\epsilon$ |
|  | $011$             | $2\epsilon$           | $2\epsilon$  | 0                     | 0           | 0            | 0                 | 0                     | $2\epsilon$ |
|  | $1\bar{1}0$       | $-4\epsilon$          | 0            | $2\epsilon$           | $2\epsilon$ | $-2\epsilon$ | 0                 | $-2\epsilon$          | $2\epsilon$ |
|  | $10\bar{1}$       | $-2\epsilon$          | $-2\epsilon$ | $2\epsilon$           | 0           | $2\epsilon$  | $2\epsilon$       | $2\epsilon$           | 0           |
|  | $0\bar{1}1$       | $-2\epsilon$          | $2\epsilon$  | 0                     | $2\epsilon$ | $-4\epsilon$ | $-2\epsilon$      | $-4\epsilon$          | $2\epsilon$ |
| $\mathbf{R} = \epsilon \langle 111 \rangle$<br>(assumed) | $111$             | 0                     | $2\epsilon$  | $2\epsilon$           | $\epsilon$  | 0            | $\epsilon$        | 0                     | $4\epsilon$ |
|  | $\bar{1}\bar{1}1$ | $-4\epsilon$          | $-2\epsilon$ | $2\epsilon$           | $3\epsilon$ | $-4\epsilon$ | $-\epsilon$       | $-4\epsilon$          | $4\epsilon$ |
|  | $1\bar{1}\bar{1}$ | 0                     | $2\epsilon$  | $2\epsilon$           | $-\epsilon$ | $4\epsilon$  | $3\epsilon$       | $4\epsilon$           | 0           |
|  | $\bar{1}11$       | $4\epsilon$           | $2\epsilon$  | $-2\epsilon$          | $-\epsilon$ | 0            | $-\epsilon$       | 0                     | 0           |

Combination of the image direction analysis with the image extinction analysis reveals that the most likely atomic displacement is of the form  $\{110\}\langle\bar{1}\bar{1}0\rangle$ ; this is the mode of displacement most commonly associated with tweed contrast microstructures.

#### 6. Diffraction Streaking: Extinction Analysis

Cu-Mn samples aged to reveal V-shaped images also show weak streaking in the associated SAEDP. These streaks can be used to identify the microstructure in the area selected for imaging. Diffraction spot streaking is associated with either the shape of crystal defects in the lattice or from lattice strain associated with them. Stenographic projection can be used to predict the direction of diffraction spot streaking. In this case expected streak direction for  $\langle 110 \rangle$  type atomic displacements is shown by arrows in Figures 19, 21 & 23, while streak directions for  $\langle 111 \rangle$  type atomic displacements is shown by arrows in Figures 20, 22 & 24.

Figure 29 shows diffraction spot streaking for a  $[001]$  zone pattern taken from a Cu-Mn sample aged at  $400^\circ\text{C}$  for 10 hours. This sample shows streaking in the  $[\bar{2}20]$  and  $[220]$  directions. Examination of Figures 19 and 20 shows that all streaks predicted by  $\langle 111 \rangle$  type atomic displacements are present while only two of the four streaks predicted by  $\langle 110 \rangle$  type atomic displacements exist. Figure 30 shows diffraction streaking for a  $[011]$  zone pattern acquired from a Cu-Mn sample aged at  $500^\circ\text{C}$  for 8 hours. This sample shows streaking in the  $[2\bar{1}\bar{1}]$  and  $[2\bar{1}1]$  directions. Comparing the observed directions to those predicted in Figures 21 and 22 shows that while one streak predicted for the  $\langle 110 \rangle$  type atomic displacement is missing, the streak directions are wrong for  $\langle 111 \rangle$  type atomic displacements where  $\langle 111 \rangle$  streaking is predicted.

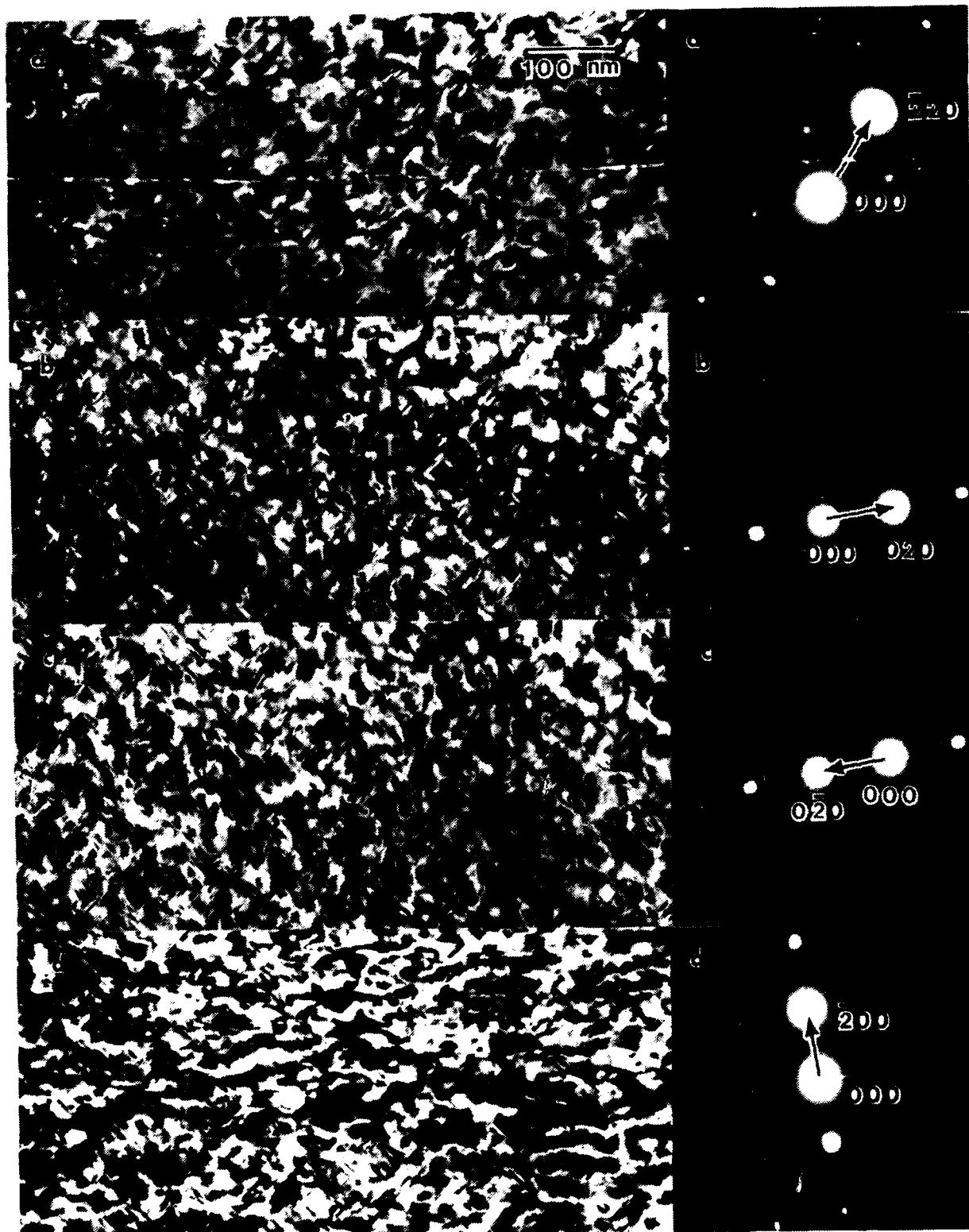


Figure 26: Aged Cu-Mn showing V-shaped images, (001) Zone, a:  $g = \bar{2}20$ , b:  $g = 020$ , c:  $g = 0\bar{2}0$ , d:  $g = \bar{2}00$ .

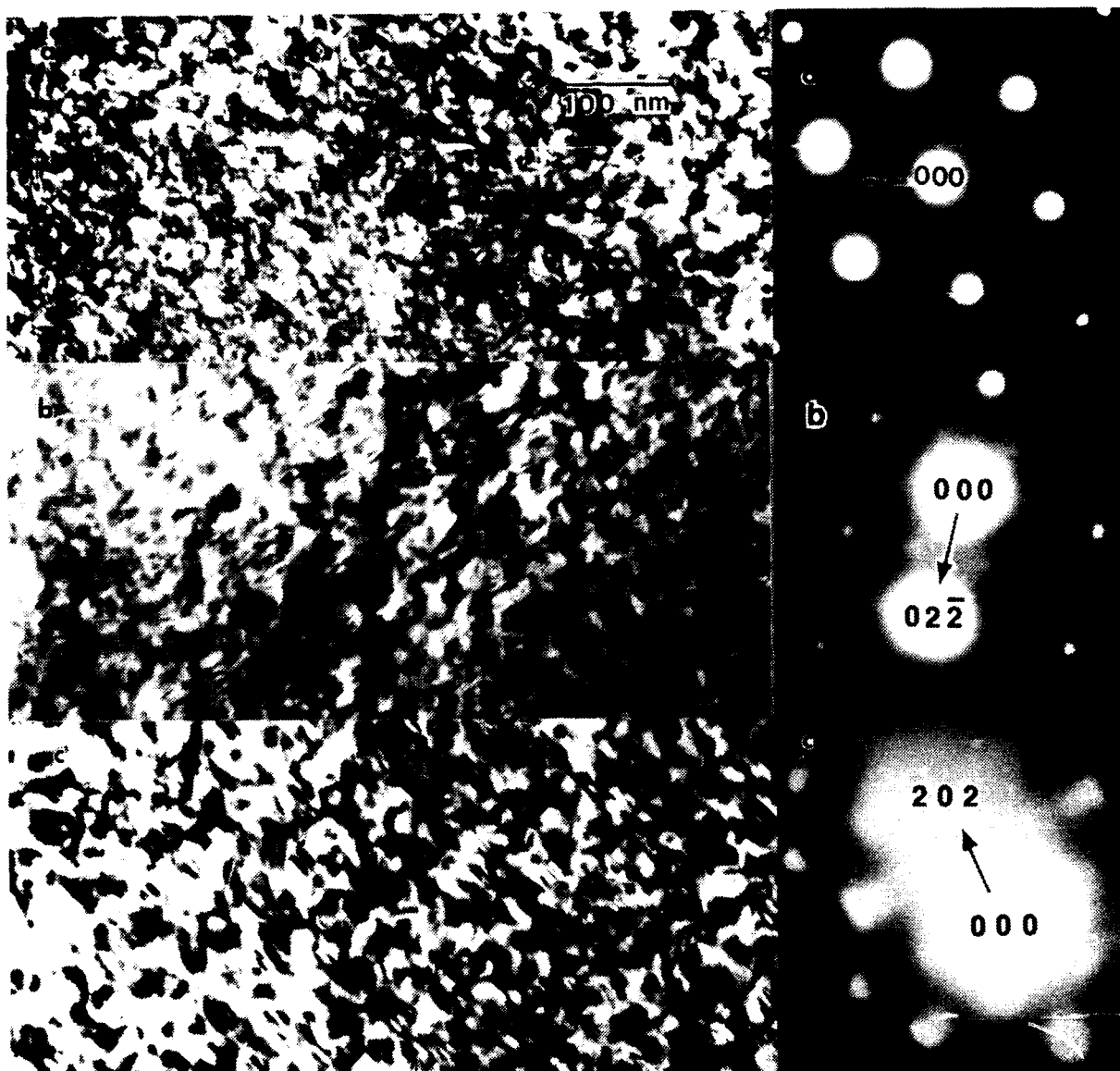


Figure 27: Aged Cu-Mn alloy showing V-shaped images,  $(\bar{1}11)$  zone, a: Bragg condition, b:  $g = 02\bar{2}$  and c:  $g = 20\bar{1}$ .

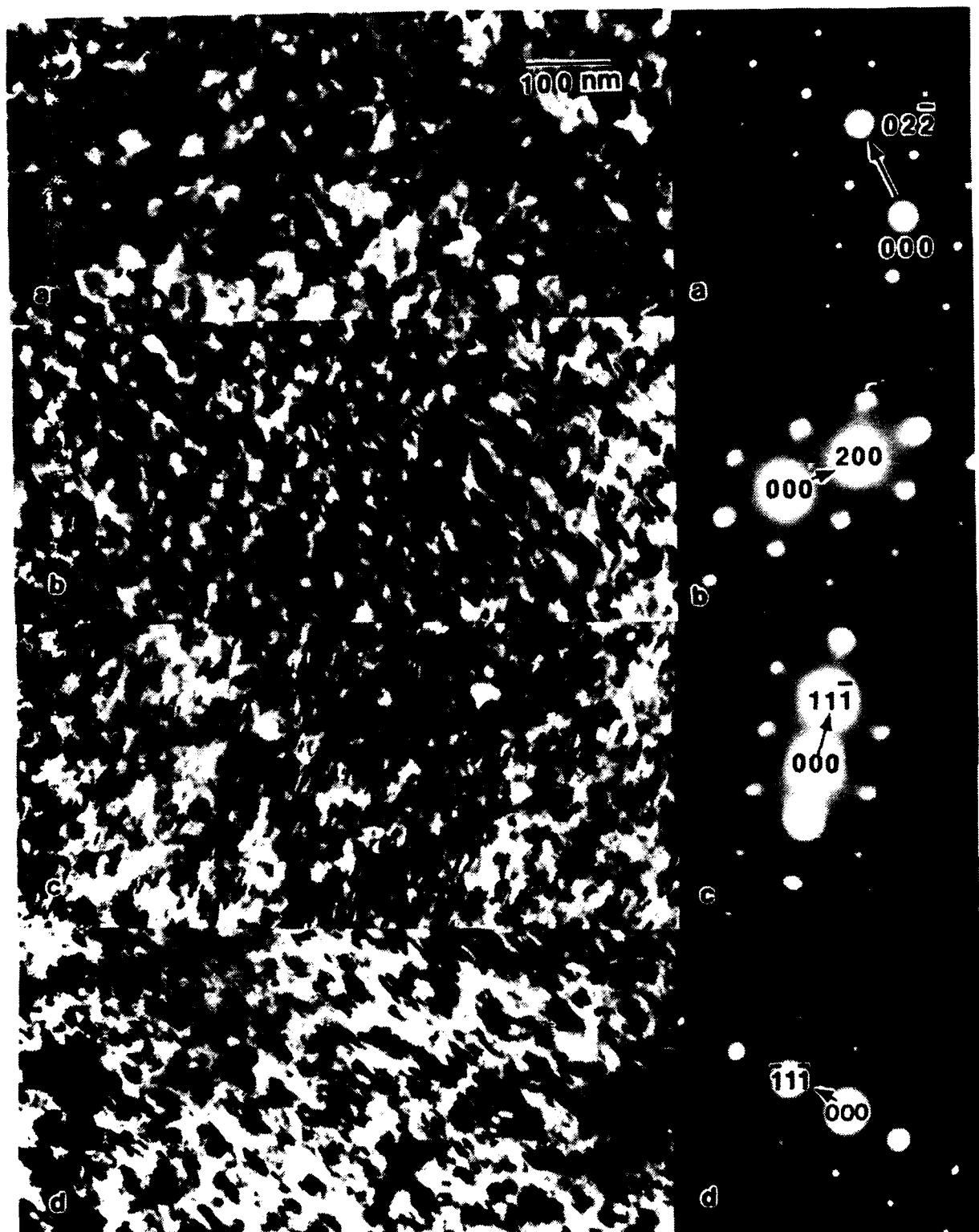


Figure 28: Aged Cu-Mn alloy showing V-shaped images, (011) zone, a:  $g=022$ , b:  $g=200$ , c:  $g=111$ , d:  $g=111$ .

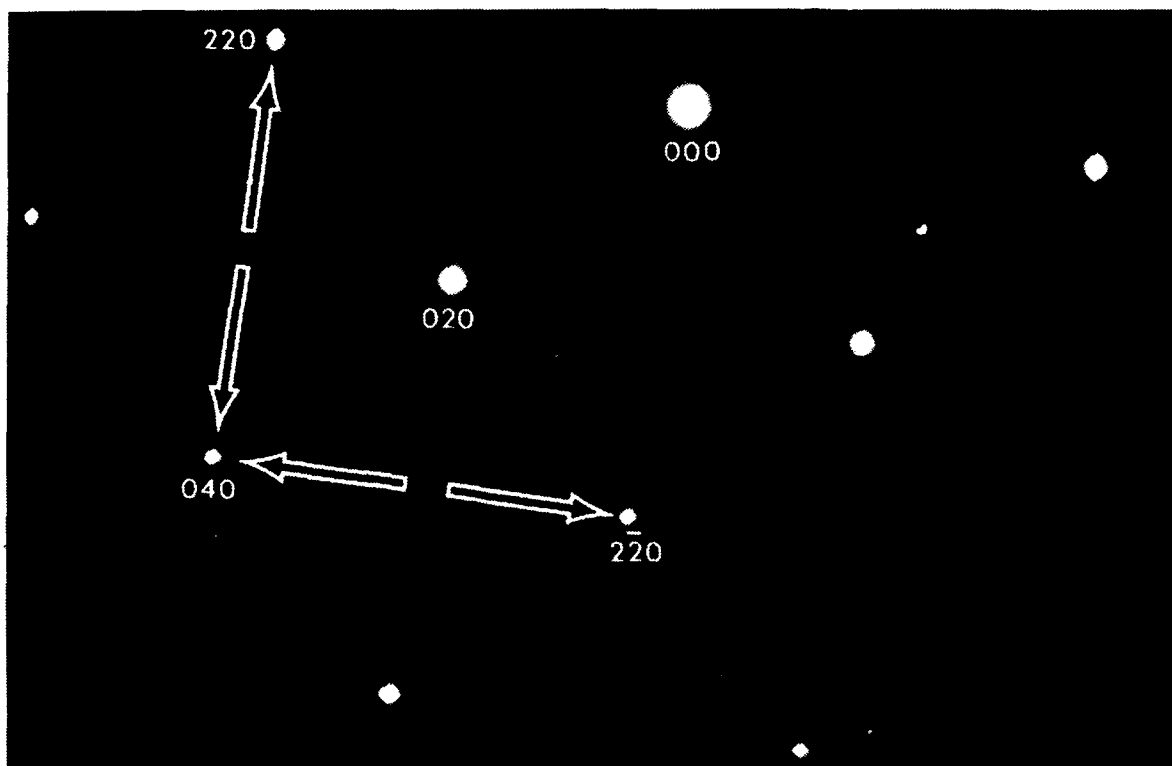


Figure 29: Diffraction spot streaking for a [001] zone pattern taken from a Cu-Mn sample aged at 400 °C for 10 hours.

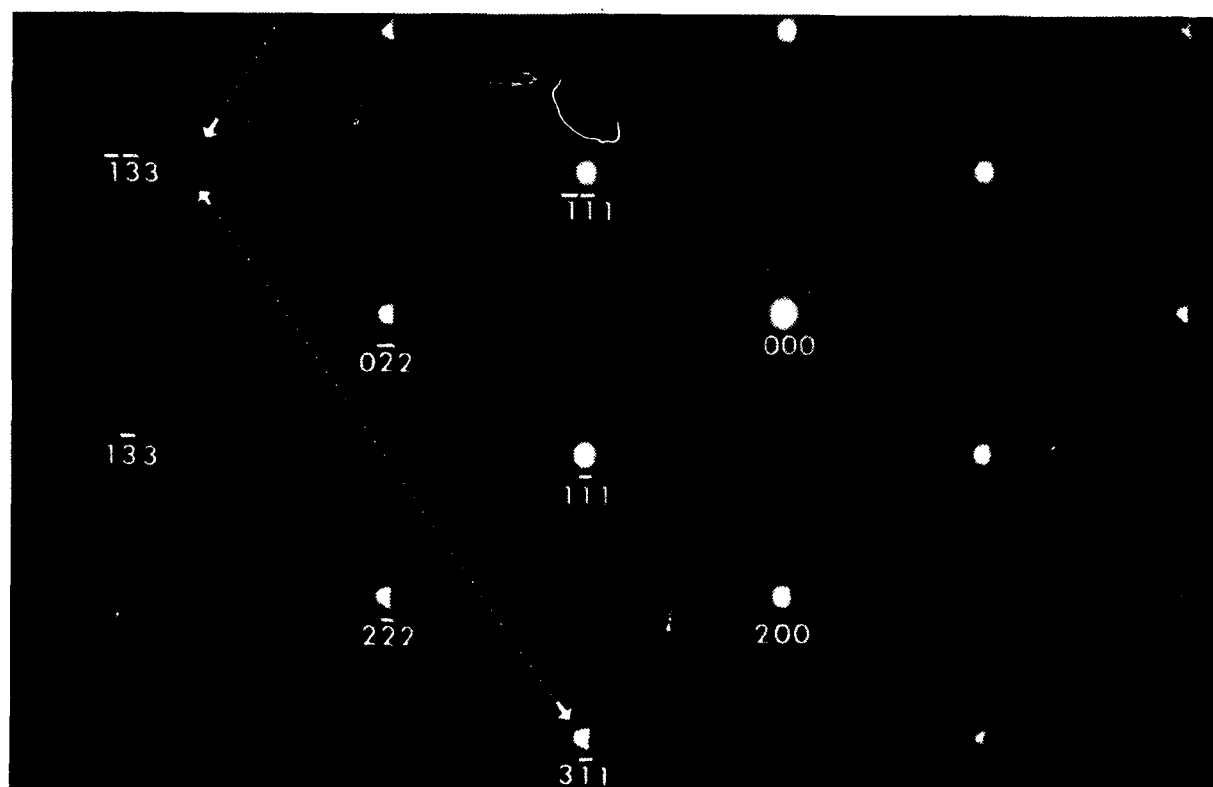


Figure 30: Diffraction streaking for a [011] zone pattern acquired from a Cu-Mn sample aged at 500 °C for 8 hours.

The extinction of relrods can be used to further characterize the microstructure. Relrod extinction will occur when  $\mathbf{g} \cdot \mathbf{e} = 0$ . If we assume the static shear displacement wave  $\epsilon\langle 110 \rangle \langle \bar{1}\bar{1}0 \rangle$  normally found in tweed structure  $\mathbf{e} = \epsilon\langle \bar{1}\bar{1}0 \rangle$ . The number of  $\langle 110 \rangle$  relrods which will vanish is 2 for {h00}, 1 for {hh0} and 3 for {hhh} reflections. Tables III and IV tabulate values of  $\mathbf{g} \cdot \mathbf{e}$  for the  $\mathbf{g}$  vectors found Figures 27 and 28. Actual streak direction seen in Figures 27 and 28 are listed below each table.

| Table III: Streak Extinction Analysis (011) Zone Axis |                  |  |                    |                          |                          |
|---|------------------|--|--------------------|--------------------------|--------------------------|
| Atom Displacement                                     | Streak Direction | Value of $\mathbf{g} \cdot \mathbf{e}$ |                    |                          |                          |
|   |                  | $\mathbf{g} = 02\bar{2}$               | $\mathbf{g} = 200$ | $\mathbf{g} = 11\bar{1}$ | $\mathbf{g} = \bar{1}11$ |
| 110   | $2\bar{1}1$      | 2                                      | 2                  | 2                        | 0                        |
| 101   | $21\bar{1}$      | 0                                      | 2                  | 0                        | -2                       |
| 011   | $0\bar{2}2$      | 2                                      | 0                  | 0                        | 0                        |
| 110   | $21\bar{1}$      | 2                                      | 2                  | 0                        | -2                       |
| $10\bar{1}$   | $21\bar{1}$      | 2                                      | 2                  | 2                        | 0                        |
| $01\bar{1}$   | 000              | 4                                      | 0                  | 2                        | 2                        |

The actual streaks observed in Figure 27 are:

$\mathbf{g} = 02\bar{2}$  streak directions:  $21\bar{1}$ ,  $211$

$\mathbf{g} = 200$  streak directions:  $21\bar{1}$ ,  $211$

$\mathbf{g} = 11\bar{1}$  streak directions:  $21\bar{1}$

$\mathbf{g} = \bar{1}11$  streak directions:  $211$

| Table IV: Streak Extinction Analysis ( $\bar{1}11$ ) Zone Axis |                  |  |                    |
|--|------------------|--|--------------------|
| Atom Displacement  | Streak Direction | Value of $\mathbf{g} \cdot \mathbf{e}$ |                    |
|  |                  | $\mathbf{g} = 02\bar{2}$               | $\mathbf{g} = 202$ |
| 110  | $2\bar{2}4$      | 2                                      | 2                  |
| 101  | $24\bar{2}$      | -2                                     | 4                  |
| 011  | $0\bar{2}2$      | 0                                      | 2                  |
| $1\bar{1}0$  | 220              | -2                                     | 2                  |
| $10\bar{1}$  | 202              | 2                                      | 0                  |
| $0\bar{1}1$  | 422              | 4                                      | -2                 |

The actual streaks shown in Figure 28 are:  
g = 022 streak directions: 220,202,224,242,422  
g = 202 streak directions: 220,022,422,224,242

Figure 31 summarizes the expected streak directions and actual streak directions for each of the three zones. By combining the streak direction analysis with the streak extinction analysis, it becomes clear that an atomic displacement of the form  $\{110\}\langle\bar{1}\bar{1}0\rangle$  fits the experimental observations much better than an atomic displacement of the form  $\{110\}\langle111\rangle$ , and that  $\{110\}$  plates fit the observation better than  $\langle110\rangle$  needles.

## 7. High Resolution TEM

In order to examine the correlation between lattice fringes and the V-shaped images due to diffraction contrast, the lattice images were intentionally taken in such a way that both images overlapped. This required the sacrifice of some lattice fringe image quality. Additionally, flickering occurred during the film exposure further deteriorating lattice image quality. An example lattice fringe image photograph is included as Figure 32. The SAEDP for this image showed the incident beam, a strong  $\langle\bar{1}11\rangle$  systematic reflection and two weak  $\langle002\rangle$  reflections. The crystal is at a near  $(110)$  orientation and the crystallographic directions are indicated. The large dark area lying in approximately a  $[\bar{1}11]$  orientation shows the V-shaped images. The horizontal fringes exactly correspond to  $(\bar{1}11)$  planes whose spacing is 0.22nm and will be referred to as  $(\bar{1}11)$  fringes. The oblique fringes were frequently seen inside of, and in the neighborhood of V-shaped images. There are two type of oblique fringes. One type, which runs from upper left to lower right has a fringe spacing of from 0.19nm (the spacing of  $(002)$  planes) to 0.24nm and are almost normal to the  $[002]$  direction. Even though the fringe spacing does not always match the  $(002)$  plane spacing, these fringes are thought to be  $(002)$  planes and will be referred to as  $(002)$  fringes. The



| Zone Axis | $\langle 110 \rangle^*$ relrod | $\langle 111 \rangle^*$ relrod | $\langle 110 \rangle^*$ relrod + extinction | Observed |
|-----------|--------------------------------|--------------------------------|---|----------|
| [001]     |                                |                                |   |          |
| [011]     |                                |                                |   |          |
| [111]     |                                |                                |   |          |

**Figure 31:** Comparison of predicted and actual diffraction spot streaking for [001], [011] and  $\bar{1}\bar{1}\bar{1}$  zone axis.

other oblique fringe runs from upper right to lower left and have a spacing of 0.19nm to 0.24nm. These fringes are less distinct, but make an angle nearly the same as (002) fringes with respect to the  $\bar{1}\bar{1}\bar{1}$  direction and are therefore thought to be the lattice fringes of a twin crystallite with a  $\bar{1}\bar{1}\bar{1}$  twinning axis. The approximate twin size is 20nm x 200nm and the twin boundary has not been observed. It should be noted that the SAEDP associated with this image does not show twin spots, possibly because the twins are small both in size and in number.

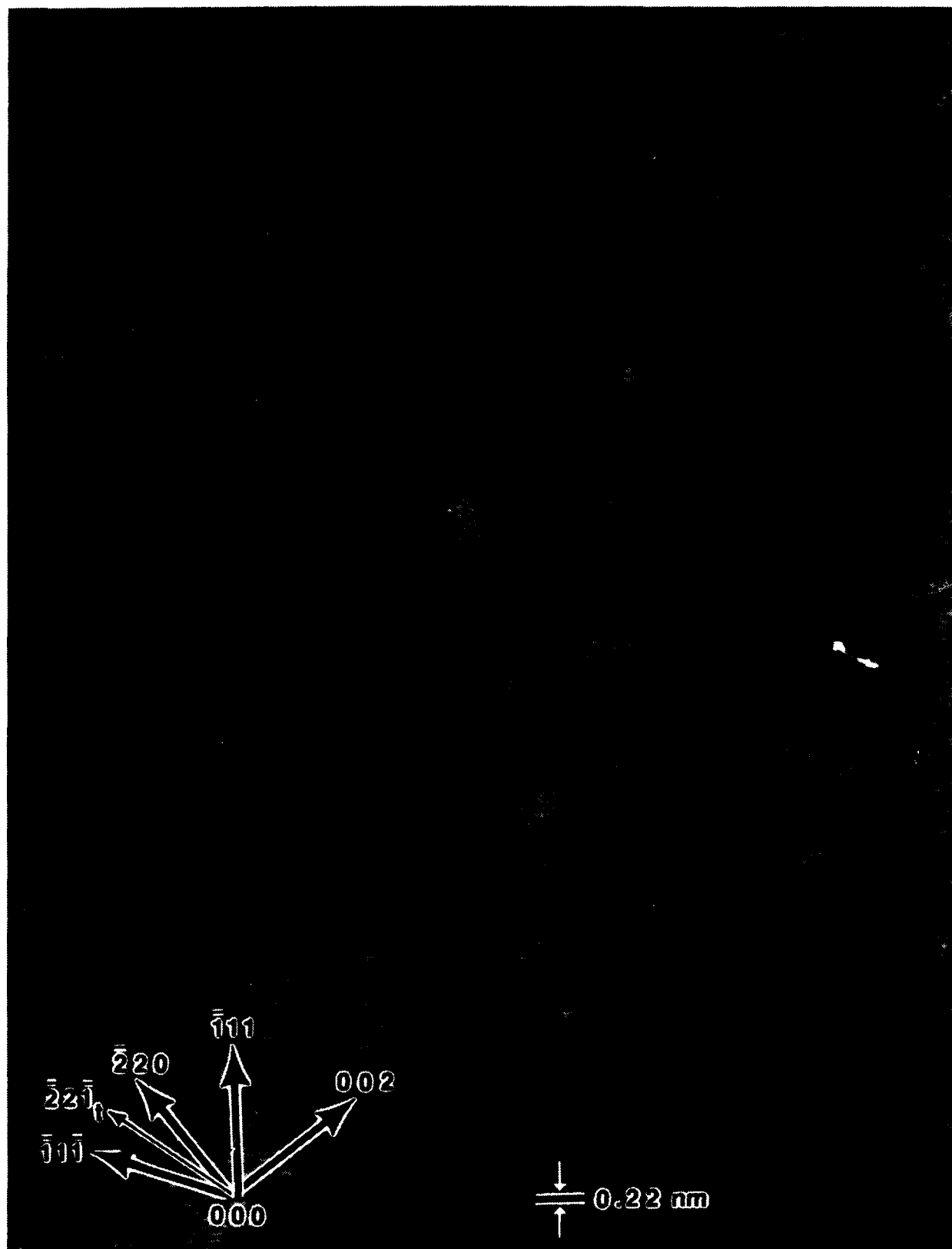


**Figure 32:** HREM showing correlation between lattice fringes and V-shaped image. FCT crystallites and twins with  $[111]$  twinning axis are seen near V-shaped image.

When  $(\bar{1}11)$  fringes pass across a branch of a V-shaped image they are seen to shift. Sometimes an individual fringe will disappear. There is no measurable change in fringe spacing between one side of the V-shaped image branch and the other. The largest shift in  $(\bar{1}11)$  fringes normally occurs when they cross the branch of a V-shaped image towards its tip. The shift in the  $(\bar{1}11)$  fringes is thought to occur due to the presence of an FCT crystallite within the V-shaped image. The existence of an FCT crystallite is also supported by the higher concentration of manganese at V-shaped images as reported below. The exact FCT crystal boundary location is not clear, but its approximate location is shown by the shifted and missing fringes. The missing fringes indicate dislocations which are predominately edge in character and are thus an additional indication of the FCT crystallite boundary location.

#### 8. Microbeam compositional analysis

The Cu-Mn phase diagram shows a miscibility gap between 40-90% Mn by weight. Aging of the alloy thus results in concentration gradients. Measurements of Cu and Mn concentration was performed on the rounded sites which contain V-shaped images, and on the surrounding matrix of the microstructure. Typical results are given in Figure 33a for the matrix and Figure 33b for a V-shaped image. The Mn concentration in the vicinity of the V-shaped images is clearly higher than in the matrix.

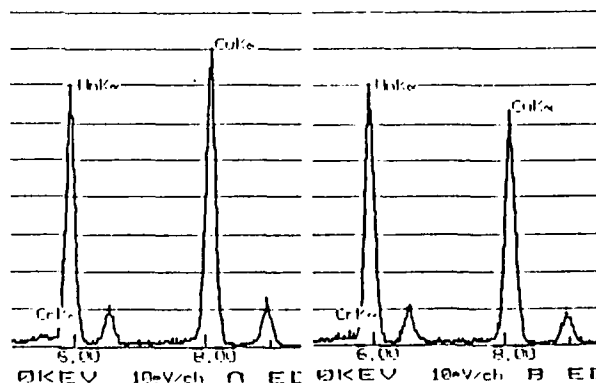


**Figure 33:** EDX analysis of Cu and Mn for matrix (a), and for round or V-shaped image (b). Sample aged at 450 °C for 10 hours.

A rough estimate of Mn concentration was obtained for a number of regions which contained V-shaped images; the Mn concentration varied from 49% to 59% by weight. Since these V-containing images were completely embedded in the matrix, the actual Mn concentration in the regions which form V-shaped images is probably much higher. At Mn concentrations of 80 wt. % or greater FCT martensite is stable at room temperature [Ref. 12]. From these results, it seems quite possible that the Mn concentration in the vicinity of the V-shaped images is high enough for the FCT phase to be stable at room temperature.

## V. DISCUSSION

### A. "Mottled" and "String" Images

The term "tweed" is a generic term for a particular sort of diffraction contrast in TEM images. This typically consists of irregular lines of contrast lying approximately along traces of  $\{110\}$  planes of a cubic parent phase, forming a kind of cross-hatched pattern. The lines of contrast obey extinction rules which are consistent with them being due to  $\langle 110 \rangle$  shear distortions of  $\{110\}$  planes [Ref. 81,84]. There are numerous systems in which tweed microstructures are observed, and a variety of origins of the shear distortions which are one of the two basic conditions that must be satisfied for this type of image to develop. The conditions are: (i) a source of finely distributed centers of asymmetric strain, and (ii) an elastically anisotropic matrix phase. In different systems the strain centers may be G-P zones [Ref. 84], fine precipitates [Ref. 85], ordered domains [Ref. 86], or simply domains in which there is an incipient lattice transition which distorts the lattice [Ref. 87]. For many cubic lattices, the existence of certain soft elastic constants often provides a matrix phase which is particularly susceptible to shear distortions of the type  $\{110\}\langle 110 \rangle$  [Ref. 88]. In order to excite this distortion, based on the  $\langle 110 \rangle$  transverse phonon mode, the straining centers distributed in the matrix must be asymmetric. If they are symmetric, they are more likely to excite the typically soft  $\langle 100 \rangle$  longitudinal mode, the distortions of which would lead to  $\{100\}$  contrast traces rather than the typical  $\{110\}$  contrast traces of a true tweed microstructure [Ref. 90].

For an aging temperature of 400°C, the alloy studied in the present work displayed a "mottled" contrast for aging times less than about 4 hours, as seen in Figure 34. The fact that a tweed contrast microstructure is not displayed at these short aging times indicates that the conditions for tweed [Ref. 84] have not (yet) been satisfied. That is, there are either not

enough points of asymmetric strain in the microstructure, and/or the level of asymmetric strain provided by each point is not sufficient. If we assume that the source of asymmetric straining points in this case is the distortion of the incipient FCC to FCT lattice transition occurring within Mn-enriched regions in the

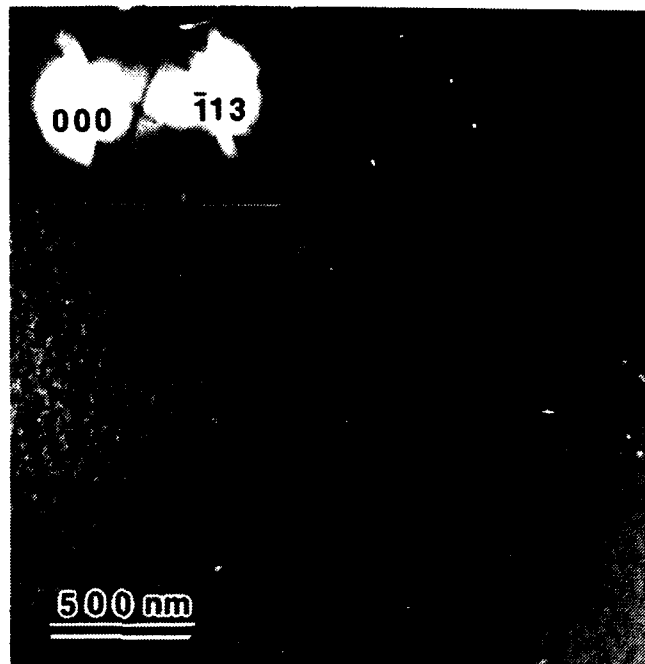


Figure 34: Mottled contrast and slip trace in sample aged 2 hours at 400 ° C. Bright field image with  $g=113$ . Beam direction near  $\langle 110 \rangle$ .

microstructure, then it is apparent that at these early times the phase separation in the Cu-Mn FCC solid solution has not yet produced sufficient numbers of Mn-enriched regions or that perhaps the regions have not yet achieved the degree of Mn enrichment required to undergo a tetragonal distortion upon cooling.

#### B. Tweed Contrast

The "sharpness" of a tweed microstructure, that is to say the degree of alignment and contrast, is dependent on the distribution, the nature and the magnitude of the strain centers, as well as the degree of anisotropy of the matrix phase. If any of these factors is deficient (not enough strain centers, not enough asymmetric distortion provided by each strain center, or insufficient elastic anisotropy of the matrix), the typical  $\{110\}$ -aligned tweed contrast will not be observed; in these "weak" cases the image will simply present a "mottled" contrast. Therefore, many "tweedy" alloys show a variation in the distinction of the tweed contrast as the distribution and strength of the strain centers changes, for example with aging [Ref. 84] or upon cooling toward a temperature range of lattice instability [Ref. 89].

The extinction phenomenon described in section 4.1.3 and the existence of  $\langle 110 \rangle^*$  rel rods indicates that the tweed structure is caused by  $\{110\}\langle 1\bar{1}0 \rangle$  displacement waves. These results are consistent with the report of Fe-Pd alloys by Oshima et al [Ref. 78].

### C. "Tweed Bands"

The surfaces of an electropolished Cu-Mn-Al sample were normally covered by a thin manganese rich layer which was mainly amorphous and partly crystalline. If the amorphous layer is removed by ion bombardment, tweed bands were easily observed in the thicker regions of a foil. This implies that tweed bands are related to surface phenomenon. The three dimensional distributions of tweed contrast has been reported to have the highest density near foil surfaces and those of tweed band contrast are thought to have the highest density closer to the foil surfaces than tweed contrast [Ref. 78]. By using molecular-dynamics simulations, Silberstein and Clapp have found that an interatomic potential that is unstable to  $\{110\}\langle 1\bar{1}0 \rangle$  shears leads to tweed formation in fcc crystals [Ref. 90]. It is possible that the  $\{110\}\langle 1\bar{1}0 \rangle$  shear displacements observed in aged Inconel 718 is due to the bulk material having a interatomic potential similar to the one investigated by Silberstein and Clapp. It is known that the binding state of interior atoms in a bulk crystal are different from the binding state of atoms on, or very close to a free surface. If the interatomic potential of the atoms near free surfaces is different in such a way that surface material is unstable to shears in a  $\{110\}$  plane but with a direction different from  $\langle 1\bar{1}0 \rangle$ , a structure, namely tweed band, different then tweed structure will appear.

The SAEDP from a crystal with (111) orientation shows strong streaking in the  $\langle 422 \rangle$  directions. This streaking is much stronger than the streaking from the (100) and (110) orientations, and can be explained to correspond to  $\langle 110 \rangle^*$  rel rods. It is possible that the strength of the  $\langle 422 \rangle$  streaking in the (111) orientation is due to it being the superposition

of  $\langle 110 \rangle^*$  rel rods and atom displacement in the  $\langle 1\bar{1}2 \rangle$  direction. If so, the displacement waves near the surface responsible for tweed bands would be  $\{110\}\langle 1\bar{1}2 \rangle$ .

#### D. "V-shaped" Contrast

The most vivid features seen in Fig. 12 are the small sets of zig-zag pattern. These are localized, presumably to the most Mn-enriched regions, and the most distinct groups of this sort were not observed to be flickering. We therefore assume that they represent static groups of self-accommodating FCT units. They are very reminiscent in form, but much smaller in size, than the type of self-accommodating martensite plate groups which are well-known to form for many thermoelastic martensites [Ref. 91]. The "V-shapes" within these groups are pointing exactly along one or the other of the two obvious  $\{110\}$  tweed traces in this  $\langle 100 \rangle$  beam direction image. The obvious indication is that the habit plane traces of the V-shaped crystals in these zig-zag groups are clustered fairly closely around one of the  $\{110\}$  parent phase planes, and in fact seem to be symmetrically disposed with respect to these parent planes. This is completely consistent with the usual morphological behavior of groups of self-accommodating martensite plates in shape memory alloys.

HREM has revealed the presence of a FCT martensite crystallite within V-shaped images and small twins with an  $\langle 111 \rangle$  twinning axis. The twins are thought to be located in the matrix outside of the FCT crystal since a twin with a  $\langle 110 \rangle$  twinning axis would be seen if it were in a FCT crystal. Part of the strain caused by the formation of FCT martensite is released by the formation of the small twins, residual strain in the matrix causes the V-shaped image. The atomic displacements due to the matrix strain are in the  $\langle 1\bar{1}0 \rangle$  direction on  $\{110\}$  planes as previously described and the center line of the V-shaped images is in  $\langle \bar{1}11 \rangle$  directions.

The V-shaped images arise from matrix strain contrast caused both by FCT martensite and twins lie outside FCT martensite. The legs of the V itself represent a strained boundary



between the FCC matrix and the FCT martensite or between two FCT martensites. The open end of the V is clearly a coherent, indeed a boundaryless region.

FCT martensites are located in manganese rich regions. Tsunoda et al report that the stiffness modulus:

$$C' = \frac{1}{2}(C_{11} - C_{12}) \quad (2)$$

decreases to approximately zero as manganese content increases to 82 at. % [Ref. 92]. It is, therefore expected that {110} twins would be present in FCT martensite or in the manganese rich regions. No {110} twins have been detected to date.

## **E. Modeling of the Microstructure**

### **1. Strain Effects on Transformation**

In this section a model of Cu-Mn microstructure morphology during aging and subsequent cooling will be presented. This model provides an explanation of changes in flickering activity and in the Specific Damping Capacity (SDC) with aging.

Vitek and Warlimont demonstrated that Manganese rich Cu-Mn alloys undergo decomposition at elevated temperatures within a metastable miscibility gap [Ref. 93]. Vintaykin et al refined the location of this miscibility gap which intersects 400°C at approximately 33 wt. % Mn and 93 wt. % Mn (see Figure 1) [Ref. 28]. Since the original composition of Incramute is 44.8 wt. % Mn, after aging beyond a certain required minimum, the microstructure will consist of small Mn enriched regions surrounded by larger Mn depleted regions (see Figure 1).

Further examination of Figure 1 shows that the edge of the strain spinodal intersects 400°C at approximately 45 wt. % Mn. This indicates that Incramute is at the very edge of this region. Vintaykin, Dmitriyev and Udovenko [Ref. 28] investigated several Cu-Mn alloys, including one, which at 48.5 at. % Mn, is almost identical to Incramute (it must

be noted that Incramute has additional alloying elements), and determined that the mechanism of decomposition for this alloy was most likely nucleation and growth.

Hillert shows that the size of the critical radius for nucleation and growth is proportional to the distance between the alloy composition and the edge of the miscibility gap. The critical radius approaches zero at the spinodal and infinity at the miscibility gap (Some composition inhomogeneity is required even for spinodal decomposition). The processes of nucleation and growth and spinodal decomposition can be thought of as continuous in this region; If a large enough nucleate is formed with a maximum composition within the spinodal, the same thermodynamic forces that cause spinodal decomposition will encourage its growth. [Ref. 94]

The decomposition of the microstructure into small Mn enriched regions and large Mn depleted regions results in localized strained regions in the crystal in the area around and within the Mn enriched regions due to the lattice mismatch between these regions. Clapp demonstrates that localized strained regions can result in the formation of soft phonon modes, that is a large reduction in the elastic constant [Ref. 95]. This large reduction in the elastic constant allows large strains to develop at relatively low stress.

The existence in a soft phonon mode in Cu-Mn was demonstrated by Tsunoda et al [Ref. 92]. Figure 35 which was copied from Reference 92 shows the value of  $C'$  approaching zero at approximately 82 at. % Mn, the composition at which the Neel Temperature is approximately the same as room temperature. A low value of  $C'$  indicates that the FCC lattice is unstable to the  $\{110\}\langle 1\bar{1}0\rangle$  shear mode. A coupling of two  $\{110\}\langle 1\bar{1}0\rangle$  shears, which give a net  $\langle 112\rangle$  displacement, can create an FCT lattice.

Silberstein and Clapp modeled the lattice potential vs strain as a double minimum curve in the case of a strongly anharmonic lattice which exhibited a  $\langle 1\bar{1}0\rangle\{110\}$  shear instability [Ref. 90]. Figure 36 shows this double minimum curve. The height of the energy

barrier is marked as  $\epsilon$ . At various temperatures the system properties are:

1. If  $kT < \epsilon$ , the crystal will tend to stay in a strained configuration (tetragonal) as the kinetic energy is not large enough to surmount the free energy barrier. A diffraction pattern taken under this condition would show spot displacement from the Bragg position.
2. If  $kt \approx \epsilon$ , the crystal has a finite probability of climbing the energy barrier and will keep switching from one strained configuration to the other. A diffraction pattern would show spot splitting or elongation.
3. If  $kt > \epsilon$ , the crystal lattice will behave as a regular FCC lattice with the atoms vibrating around the zero strain position. The diffraction pattern should show peaks at the regular Bragg position.

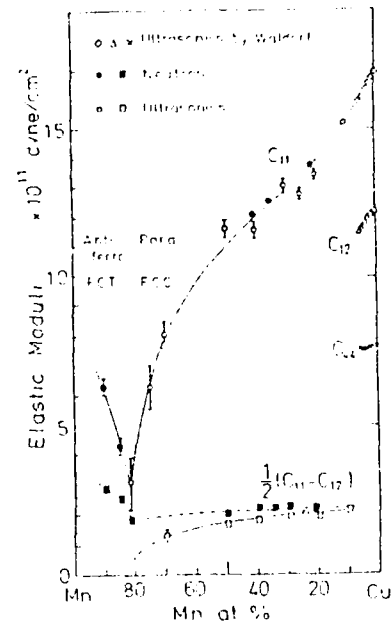


Figure 35: Elastic Moduli of Cu-Mn alloys as determined by neutron and ultrasonic measurement at room temperature.

## 2. Mechanism of Flickering

In Incramute the height of the energy barrier,  $\epsilon$ , would be approximately equal to  $kT_n$ , where  $T_n$  is the Neel temperature which is approximately the same as  $M_s$ , the martensitic start temperature. Figure 1 (phase diagram) shows that  $T_n$  (and  $M_s$ ) increase with increasing Mn concentration which would indicate that the height of the energy barrier would also increase with increasing Mn concentration.

Since Incramute lies within the miscibility gap (see Figure 1) and exhibits a continuous composition gradient during decomposition as shown in Figure 37, after

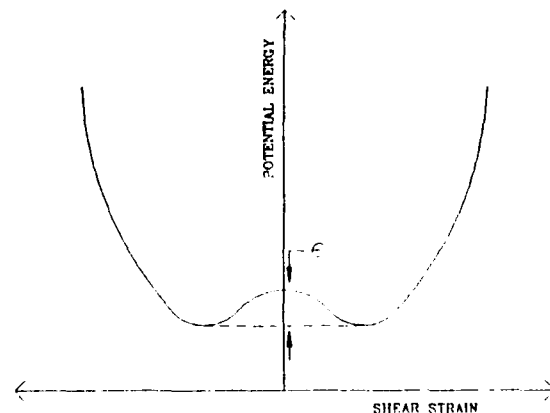


Figure 36: Schematic drawing of potential energy vs shear strain model for locally strained regions in the crystal.

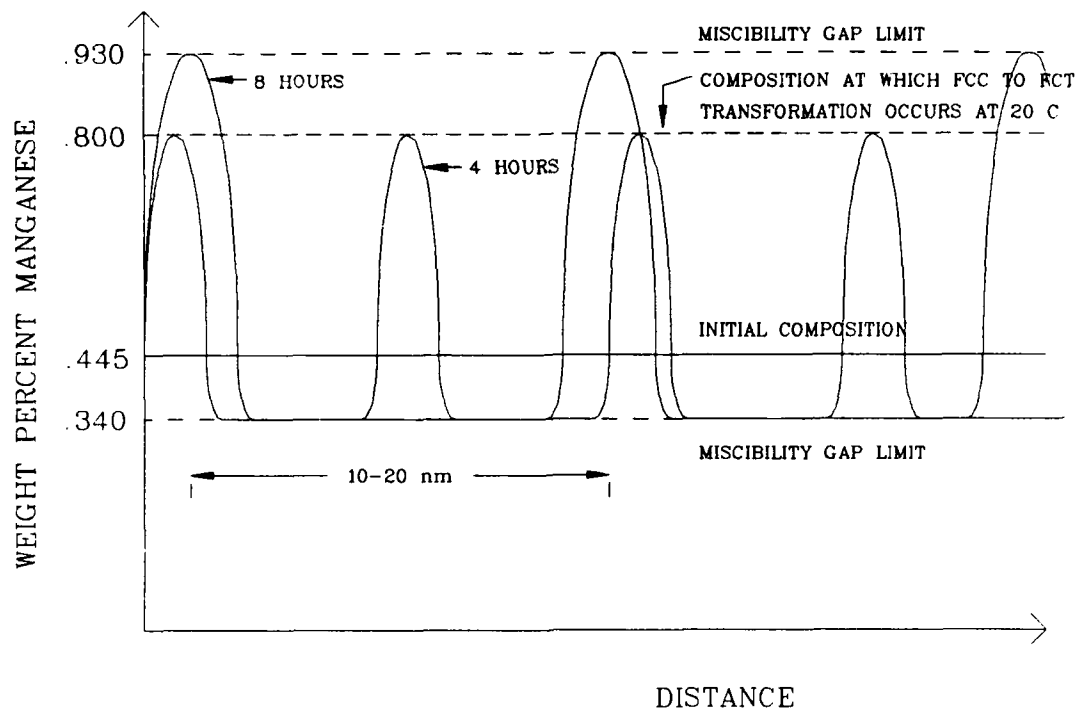


Figure 37: Schematic drawing of Incramute composition at 4 and 8 hours.

sufficient aging, some portion of the microstructure is at the composition where  $T_n$  is the same as  $T_{amb}$  (assuming  $T_{amb}$  is around the normal room temperature). Any addition of energy, such as energy added by the electron beam or the damping experiment will cause an FCT to FCC transformation of some small amount of the microstructure. Cyclic or fluctuating energy addition, such as that added by the damping experiment or experienced by local sites in the vicinity of the electron beam, will result in an continuous FCT to FCC to FCT transformation in these susceptible regions of the microstructure.

The energy required to cause this FCT to FCC to FCT transformation would be very low within regions whose composition is close to the composition where  $T_n$  is the same as  $T_{amb}$ . The  $c/a$  ratio of these regions is close to 1 since the  $c/a$  ratio for Incramute decreases with increasing Mn. Thus the regions lying near the edge of the Mn enriched zone are easily reoriented by the vibrational waves caused by the TEM or damping experiment. As the vibrational wave moves into the center of the Mn enriched zone it is amplified by the

reorientation of the c-axis of regions through which it passes. If the vibrational wave is of sufficient amplitude it is able to reorient the zones having the highest Mn enrichment.

In aged Incramute, Mn enriched regions show V-shaped images which resemble the self accommodating crystallites found in shape memory alloys. Within each of the V's, the crystallites c/a ratio decreases from the open end (where it is approximately 1) towards the tip. Alternate V's contain crystallites normally related by a twin orientation (which in Incramute has a  $\langle 111 \rangle$  twin axis). Figure 38 shows the transformation of a Mn-enriched

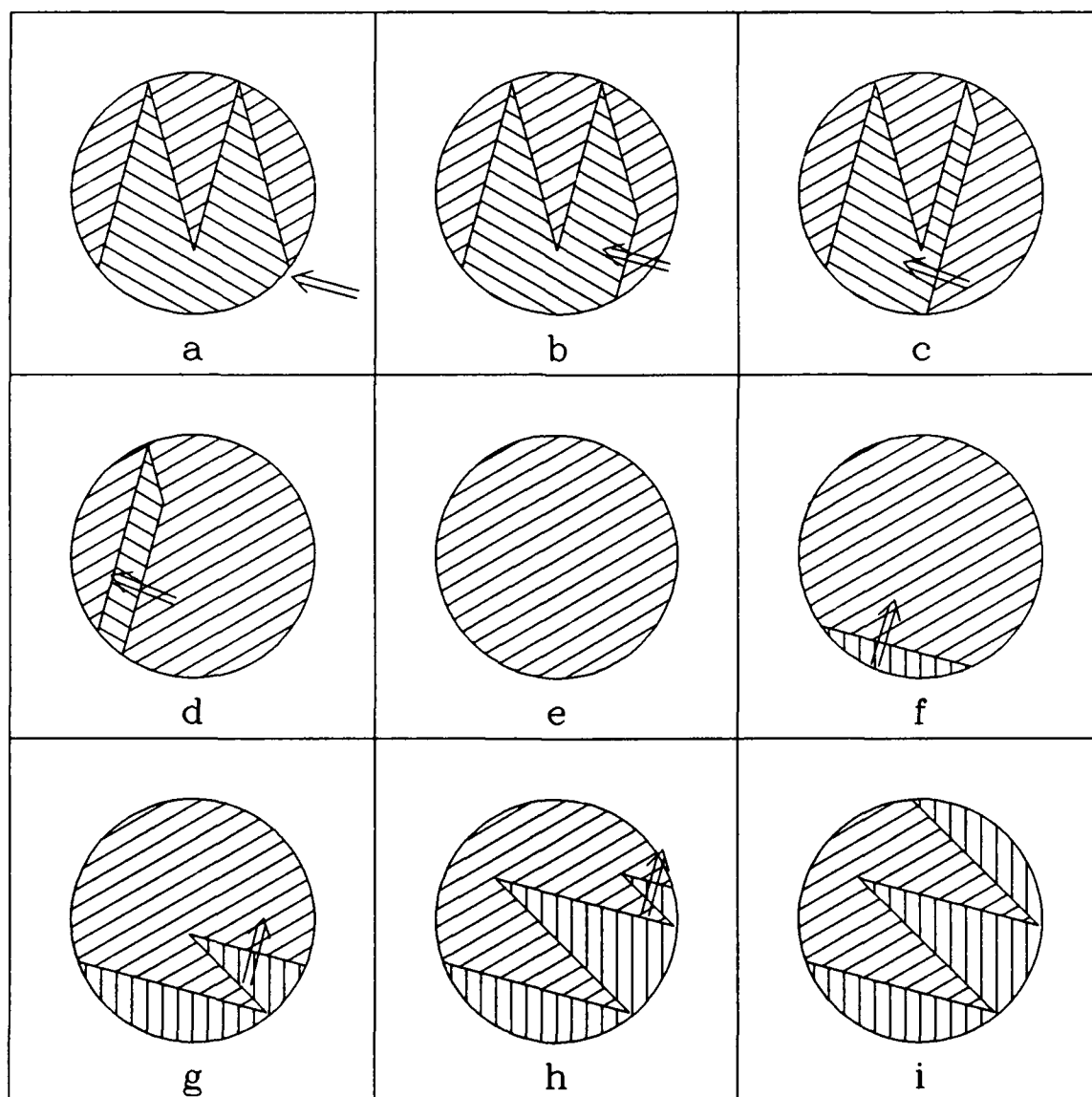


**Figure 38:** 'Cartoon' showing the mechanism of transformation from one V-shaped orientation to another as observed during flickering.

region containing self accommodating crystallites with two c-axis orientations from one V-shaped region orientation to another. Figure 38a shows the Mn-enriched region prior to arrival of the vibrational wave which will cause the transformation. In Figure 38b-e the vibrational wave enters the region and transforms it into a crystal with one c-axis orientation. The resulting crystal is highly stressed due to all of the c-axis being aligned which causes it to be 'too small' in one direction. In Figure 38f-h a spontaneous, second, transformation relieves the stresses caused by the first transformation creating FCT regions with an third c-axis orientation which is twin related to the c-axis orientation created in the first transformation. Figure 38i shows the final transformation product, a region of self-accommodating crystallites with the V's pointed in a different direction than the original configuration.

In Incommensurate samples that contain tweed structure, flickering involves one or two string images. Sometimes only a short or partial string image is seen to flicker. This suggests that flickering is caused by local stresses which affect only one or two string images. At the aging times that produce tweed structure the maximum Mn concentration is probably below the miscibility gap limit (see Figure 4) and the width of the Mn concentration peaks is small. This implies that the size of the FCT region is very small and c/a ratio close to 1.0. Little energy is required to reorient one of these regions and the specific damping coefficient is thus lower than that at more extended aging times.

Flickering is thus caused by the reorientation of the FCT crystallites which lie in Mn enriched regions of the matrix. This transformation occurs extremely rapidly and results in changes of strain contrast due to the reorientation of the strained regions between the self accommodating crystallites and / or between FCT crystallites and the matrix.

### 3. Thermodynamic Transformation Model

A spinodally decomposing alloy is one whose free energy vs composition curve is characterized by a region in which  $G''(c)$  is negative (see figure 39). Shewman [Ref. 96] gives the relationship between diffusion and  $G''(c)$  as:

$$D = MC(1-C)G'' \quad (3)$$

Where:

- D is the Diffusion coefficient.
- M is the mobility.
- C the composition.
- $G''$  the second derivative of the Free Energy.

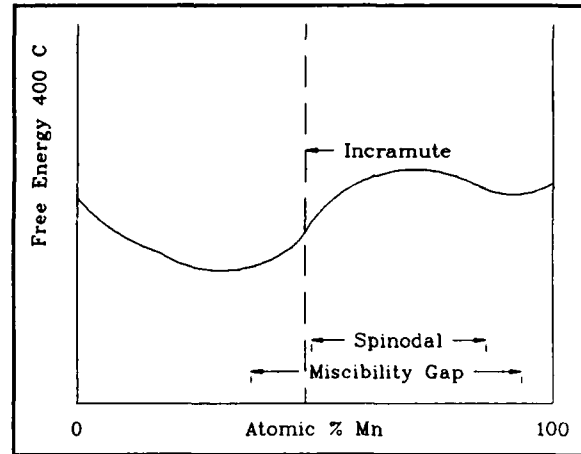


Figure 39: Schematic diagram of Free energy vs Composition for Cu-Mn alloys at 400 °C.

Cahn [Ref. 97] describes the various factors that effect free energy which include (but is not limited to) bond energy, interface energy and strain energy. Relationships described by Shewman [Ref. 96] are used to develop a model of composition vs time which includes terms related to each of these three energies.

Free energy due to atomic bonding using a nearest neighbor model is given by Shewman as:

$$G_b(C) = \frac{1}{2}NZC(1-C)(2V_{AB} - V_{BB} - V_{AA}) + RT[C\ln(C) + (1-C)\ln(1-C)] \quad (4)$$

Where:

- $G_b$  = free energy due to bonding
- $V_{AA}$  = energy of an A-A bond.
- $V_{BB}$  = energy of an B-B bond.

- $V_{AB}$  = energy of an A-B bond.
- $N$  = the number of atoms in a mole.
- $Z$  = the number of nearest neighbors.
- $C$  = atomic fraction of B atoms.
- $R$  = ideal gas constant.

The second derivative of this expression is:

$$G''_b(C) = -Z(V_{AB} - V_{AA} - V_{BB}) + RT\left(\frac{1}{C} + \frac{1}{1-C}\right) \quad (5)$$

For the interfacial free energy Shewman recommends the relationship:

$$G_i = \frac{\alpha \Delta C}{\lambda^2} \quad (6)$$

Where:

- $G_i$  = the interfacial free energy.
- $\alpha$  = a constant of proportionality
- $\lambda$  = the wavelength of the fluctuation.
- $\Delta C$  = the change in composition across the interface

For the second derivative of the strain free energy Shewman used the relationship:

$$G''_\epsilon = \frac{\eta^2 E}{2(1-\nu)} \quad (7)$$

Where:

- $G''_\epsilon$  = The second derivative of strain free energy.
- $\eta$  = The rate of change of the lattice parameter per unit change in concentration.
- $E$  = Young's modulus.



- $\nu$  = Poisson's ratio.

#### 4. Computer Model of the Transformation

Since many of the parameters required by the free energy expressions were unavailable a number of assumptions were made in developing the computer model. Specifically:

- Since the lattice parameter of Mn is larger than that of Cu,  $\eta$  was assumed to be positive and constant.
- Examination of Figure 35 shows that  $C'$ , the elastic modulus of interest in this transformation, decreases as the at. % Mn increases, up to the alloy composition at which the Neel Temperature is equal to room temperature. Since the Neel Temperature intersects 100 at. % Mn below 200°C and the temperature to be studied in the model is 400°C, the elastic modulus was assumed to decreased with increasing Mn concentration.
- By definition  $G'' = 0$  at the spinodal. The two unknown constants were solved for by using the intersection of the strain spinodal and 400°C.
- Interface free energy acts to determine the minimum wavelength and to make a coarser microstructure energetically favorable. Since the value of interface free energy,  $G_i \rightarrow 0$  as  $\lambda \rightarrow \infty$ , and due to the complexity of determining  $\Delta C$  for a given interface and determining which interface was related to which wave, the relationship  $d_i(\lambda) = \alpha/\lambda^2$  was assumed. This makes the diffusion coefficient more positive, or less negative at shorter wavelengths and thus encourages coarsening.  $G_i$  was neglected in solving for the unknown constants.

Combining the equations for  $G_e''$  and  $G_b''$  yields:

$$G''(c) - K_1 + \frac{RT}{c(1-c)} + K_2(1-c) \quad (8)$$

For the first computer run, the exact value of the strain spinodal was used to determine  $K_1$  and  $K_2$ , specifically the strain spinodal intersects 400°C at compositions of 49 at. % Mn and 87 at. % Mn. The maximum composition reached in the model's composition profile matched that predicted by the miscibility gap at 400°C. However the minimum

composition reached by the computer model was much higher than predicted by the miscibility gap at 400°C and the strain spinodal values used to actually set  $K_1$  and  $K_2$  for the final computer model were 45 at. % Mn and 87 at. % Mn. These values gave a reasonable match between the maximum and minimum values for composition predicted by the computer model and by the miscibility gap. Combining equation (1) and (6),  $d_i$  and the values of  $K_1$  and  $K_2$  determined by the method given above gave the following diffusion equation:

$$d(c) = -13.74c(1-c) + 1.33 + 15.20c(1-c)^2 + \frac{\alpha}{\lambda^2} \quad (9)$$

Figure 40 shows the value of the diffusion coefficient for two different values of  $\lambda$ , the approximate initial value of 8, and the final value of 40. The small difference is sufficient to cause microstructural coarsening. Figures 41 and 42 show the initial composition profiles used for the computer model. Two initial

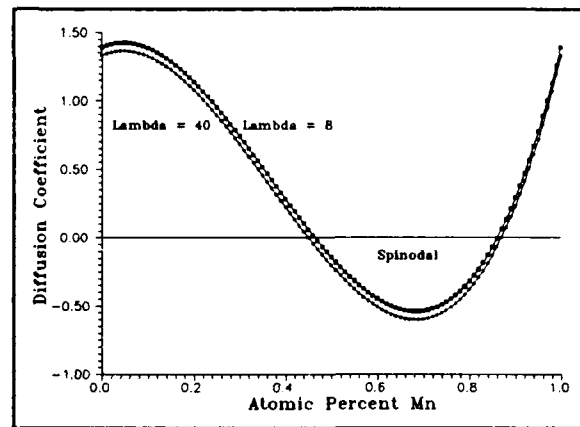


Figure 40: Plot of Equation 7 (diffusion coefficient vs atomic % Mn) for  $\lambda=8$  &  $\lambda=40$ .

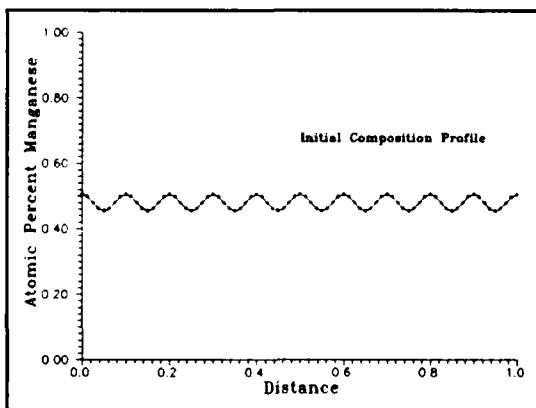


Figure 41: Initial composition for computer model simulating Incramute transformation.

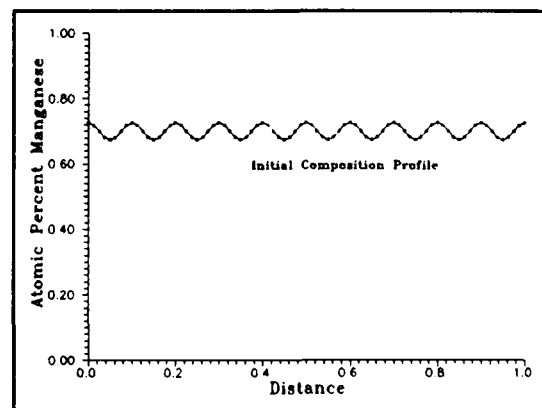


Figure 42: Initial composition for computer model of 70 at. % Mn transformation.

compositions are used to allow comparison of the transformation of an alloy near the edge of the spinodal (Ingramute), and an alloy near the center of the spinodal (70 at. % Mn). A initial sinusoidal composition profile was used since for spinodal decomposition to occur some initial microstructural inhomogeneity is needed.

## **5. Computer Model Results**

Figures 43 and 44 show the composition profile during the early part of the transformation before coarsening has started. The Ingramute profile appears as a series of sharp peaks which don't quite reach the miscibility gap. The 70 at. % Mn alloy has reached the edge of the miscibility gap and broken up into broad peaks.

Figures 45 and 46 show the composition profile at an intermediate aging time when both alloys have started to coarsen. At this stage of coarsening some of the peaks have been absorbed by the others and at least one of the peaks is notably larger than the others. Figures 47 and 48 show the composition profile at an extended aging time when an equilibrium profile (for the computer model) is being approached. After extending aging the composition profile shows one or two large Mn enriched regions surrounded by Cu enriched regions.

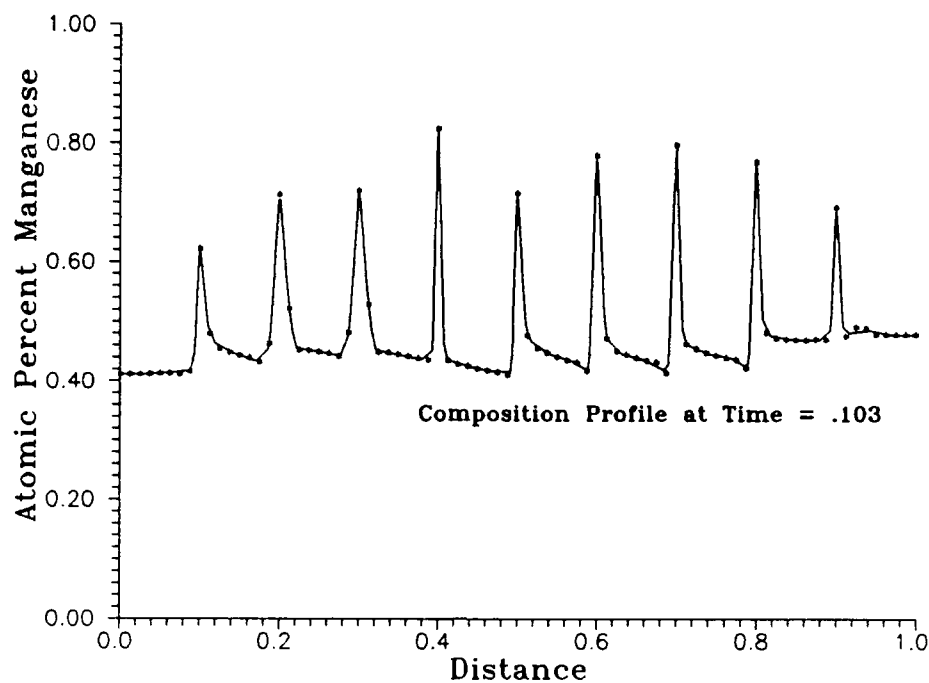
Figure 49 was prepared by counting the number of peaks every one hundred time steps and dividing the total number of node points in the model by the number of peaks to determine the average wavelength. This figure shows that Ingramute coarsens more slowly than the 70 at. % Mn alloy until the width of one of the Mn-enriched regions starts to increase then coarsens much more rapidly. Figure 50, which was copied from Reference 28, shows alloy 1, (which has the same at. % Mn as Ingramute), initially coarsening much more rapidly than alloys 2-4, (the computer model of 70 at. % Mn composition lies midway between alloy 3 and 4), then, after extended aging, much more slowly than alloys 2-4. Vintaykin characterizes alloy 1 as undergoing nucleation and growth as opposed to a pure

spinodal decomposition. The S shaped curve of the Incramute modulation wavelength shown in Figure 49 is characteristic of a nucleation and growth phenomenon. The absence of the S shaped curve in Vintaykin's data is probable explained by nucleation taking place during the quench after solution treatment of his sample.

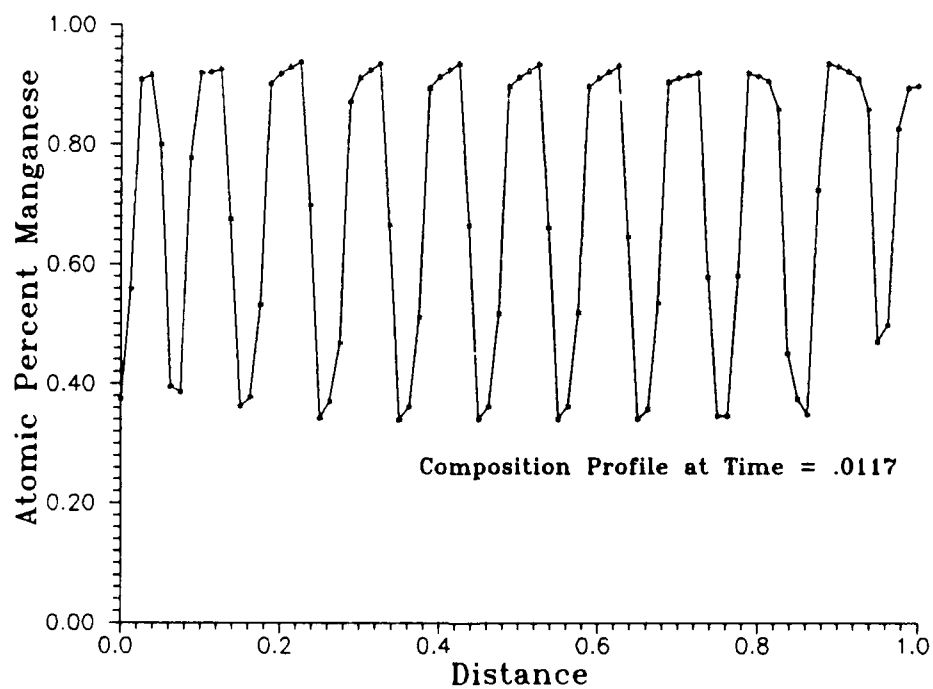
In order to test the theory that the portion of the microstructure which is at the composition where  $T_n$  is the same as  $T_{amb}$  causes flickering and high damping behavior by undergoing a reversible FCC-FCT transformation, an attempt was made to measure the amount of microstructure in the composition profile of the model near the composition of 80 at. % Mn (the composition where  $T_n = 20^\circ\text{C}$ ). This amount should be proportional to the radius of the peak (since the region of the microstructure occupied by the FCT martensites is very roughly disc (or plate) shaped and thus ~2-D) divided by the slope of the composition profile at 80 at. % Mn (since the higher the slope, the less microstructure around that composition). A problem with this model is that the maximum slope is reached when one node point is at the composition of Mn corresponding to one leg of the miscibility gap while the next node point is at the composition of Mn corresponding to the other leg of the miscibility gap, a slope of about  $\frac{1}{2}$ . This results in the amount of microstructure at a composition near 80 at. % Mn, as measured by the model, being too high at extended aging times. The actual maximum slope would be  $\infty$ , as diffusion slowed to zero, which would result in no finite volume of microstructure at 80 at. % Mn. Figure 51 shows the relative amount of Incramute microstructure near 80 at. % Mn using the computer model vs. time.

Figure 52 is a plot of SDC at an average peak strain of  $1\text{E-}3$  vs time using data taken from previous work at Naval Postgraduate School [Ref. 98]. The shape of Figure 51 and Figure 52 are similar, and SDC decreases rapidly, back to its initial value as microstructure coarsening slows (refer to Figure 49).

The reason for the decrease in SDC with aging can be explained by the shape of the composition profile. After extended aging the composition profile resembles a square wave with upper and lower values equal to the compositions corresponding to the miscibility gap concentrations at 400° C. The portion of the microstructure corresponding to the lower Mn concentration is FCC, the portion which is Mn-enriched is FCT with a c/a ratio of ~.96. With this high a c/a ratio a relatively high amount of energy is needed to reorient the c-axis. Additionally the absence of any significant amount of FCT with a c/a ratio of 1.0 results in no amplification of the vibrational wave. Without this amplification vibrational waves of large enough magnitude to reorient the FCT crystallites at lower aging times are no longer strong enough to reorient the overaged microstructure and SDC decreases.



**Figure 43:** Composition profile during the early aging transformation of Incramute.



**Figure 44:** Composition profile during the early aging transformation of a 70 at. % Mn alloy.

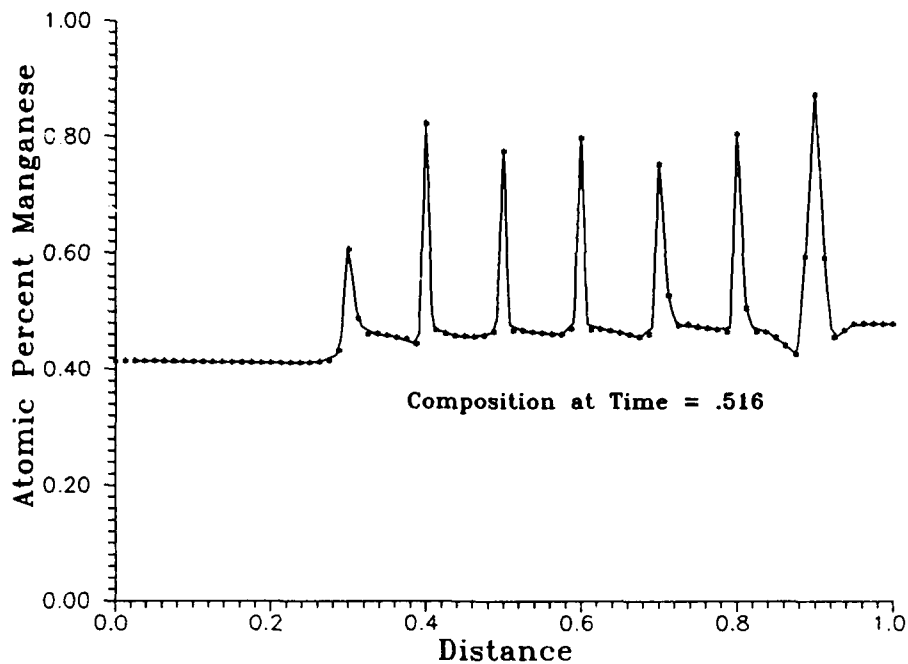


**Figure 45:** Composition profile of Incramute at the beginning of microstructural coarsening. Note that the last peak's width is larger than that of the other peaks.

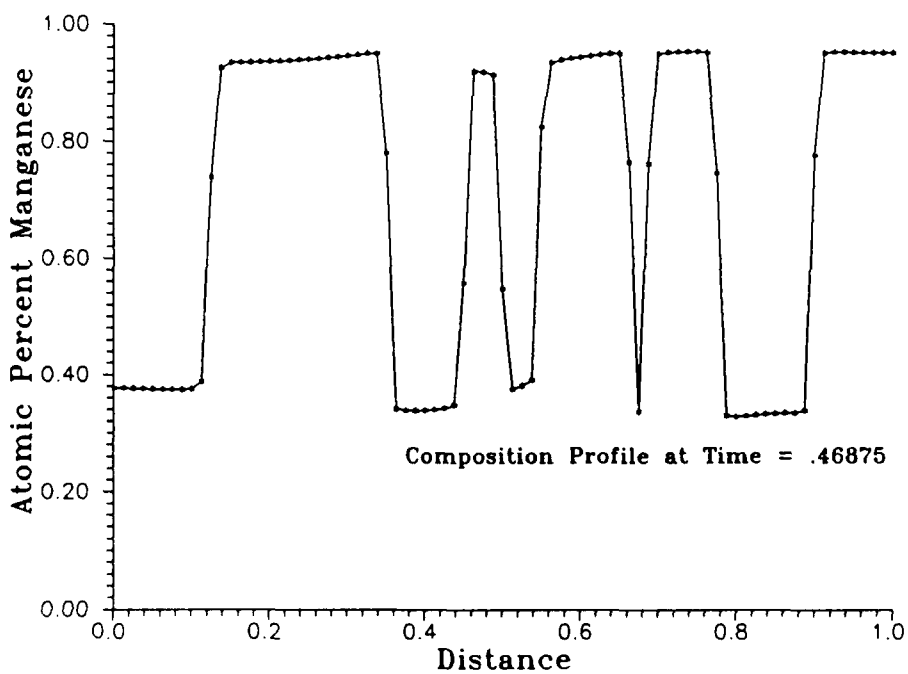


**Figure 46:** Composition profile of 70 at. % Mn alloy after microstructural coarsening has started.

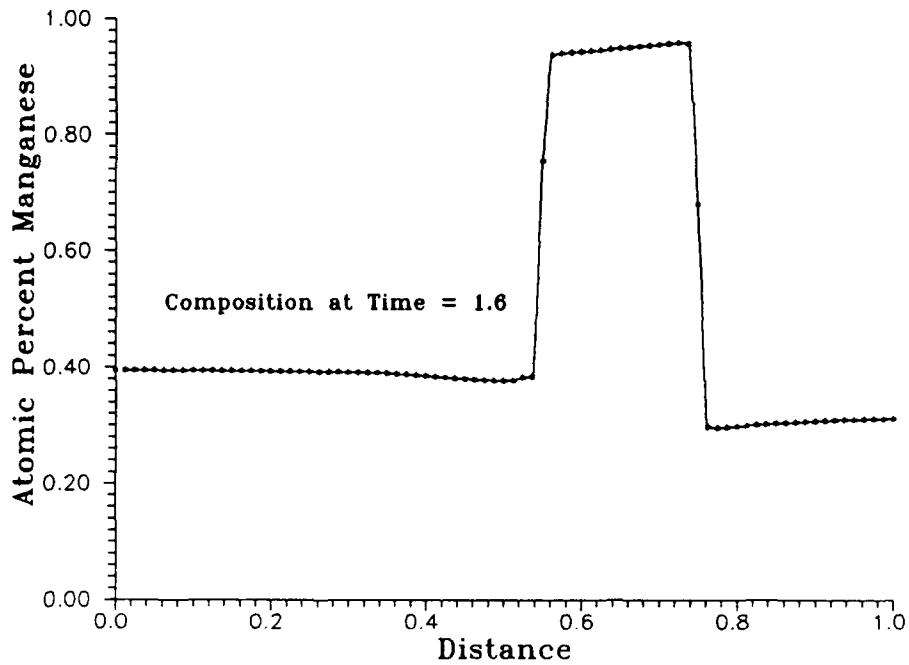


**Figure 47:** Composition profile of Incramute at the end of microstructural coarsening (in the model).

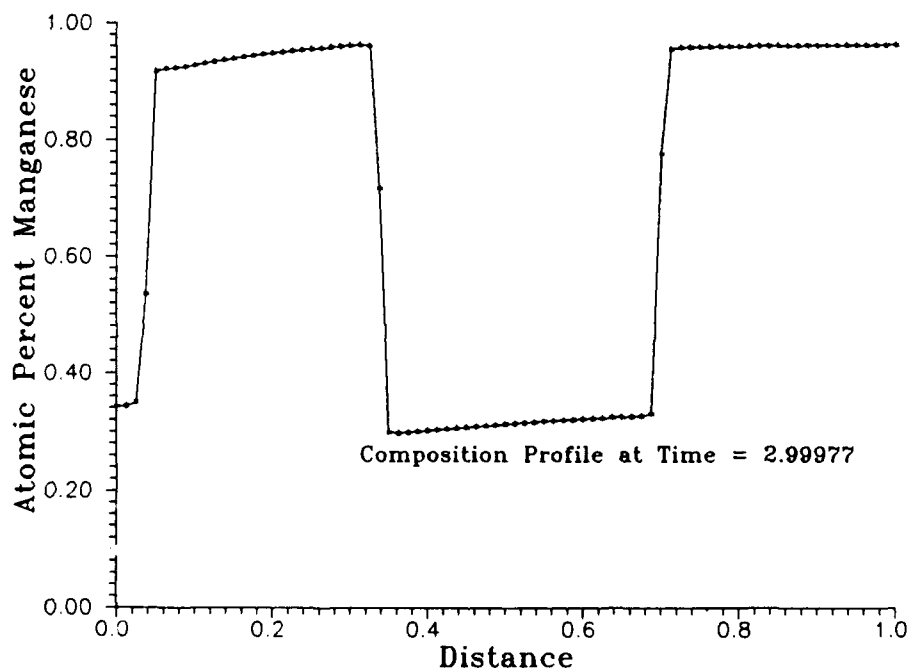


**Figure 48:** Composition profile of 70 at. % Mn alloy after extended aging. The microstructural has coarsened into two peaks.



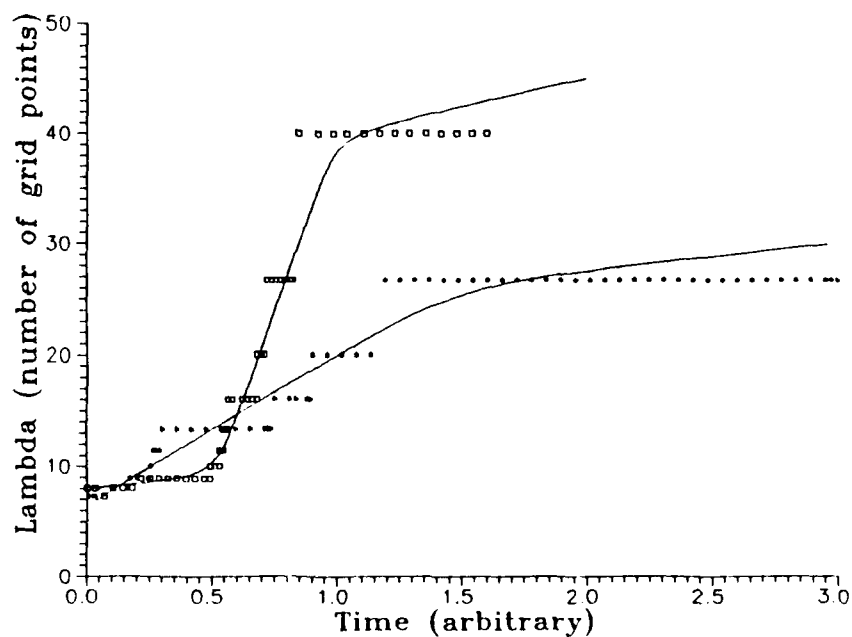


Figure 49: Plot of Wavelength vs. Time for Incramute and 70 at. % Mn. Wavelength is determined by dividing the number on node points (80) in the model by the number of peaks every 100 time steps.

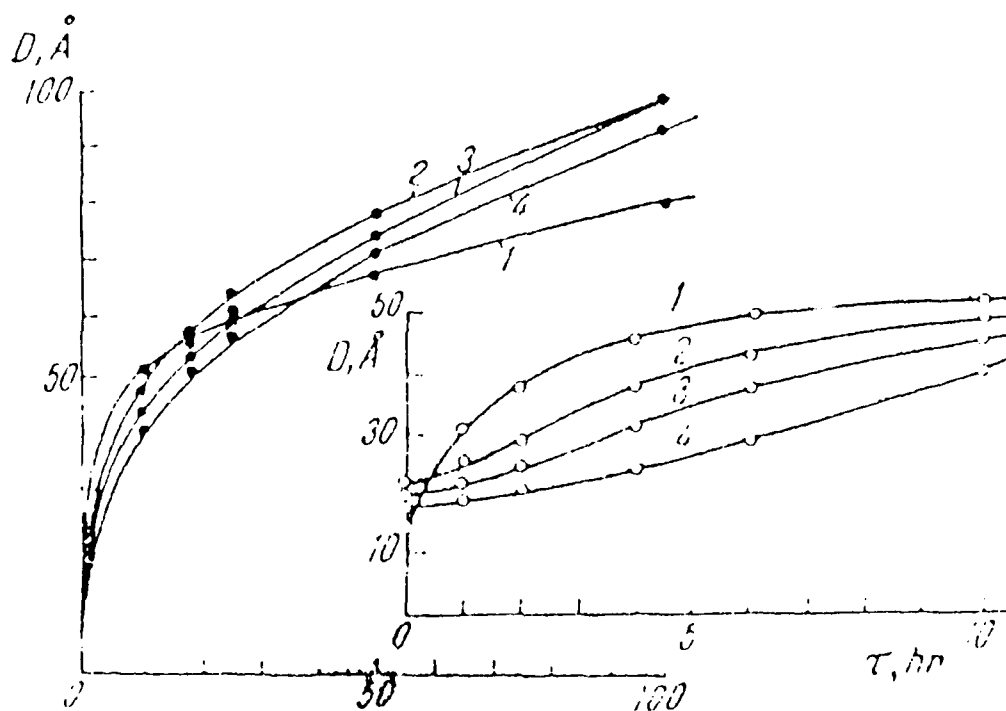
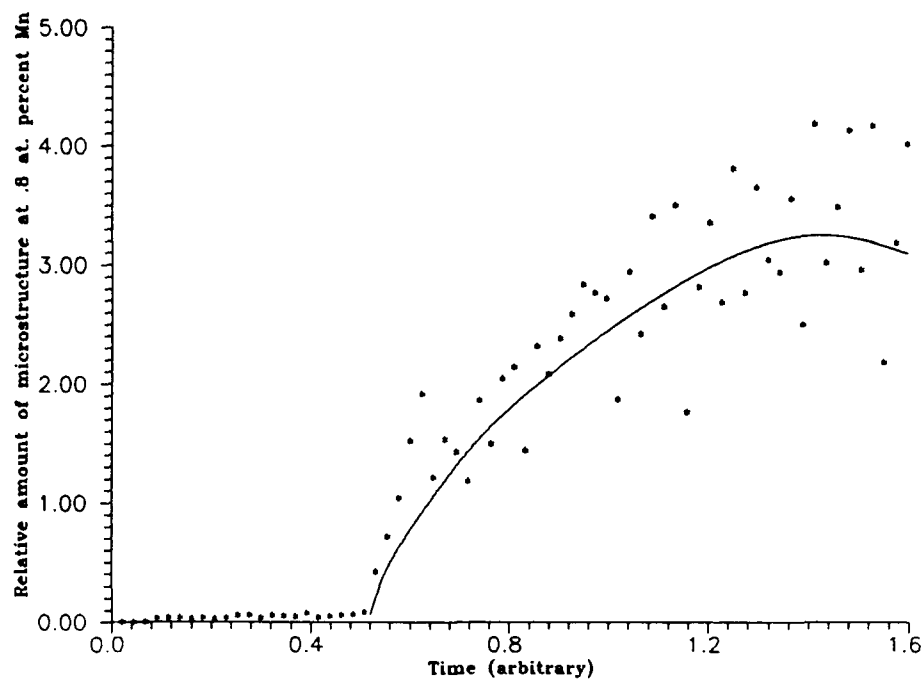
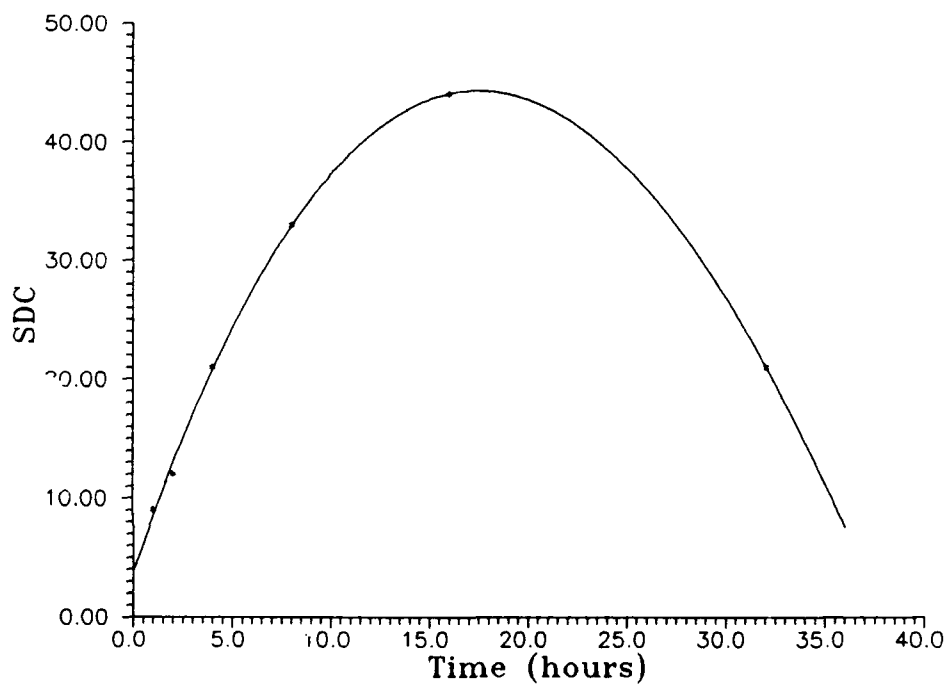


Figure 50: Plot of Wavelength vs. Time for four Cu-Mn alloys, 1) 48.5 at. % Mn (approximately the same as Incramute), 2) 59.7 at. % Mn, 3) 66.8 at. % Mn and 4) 75.1 at. % Mn.



**Figure 51:** Plot of relative amount of the computer model's microstructure near 80 at. % Mn vs time.



**Figure 52:** Plot of SDC at an average peak strain of 1E-3 vs time from Reference 10???

## F. Mechanisms of High Damping

### 1. Strain Dependence of Damping

Some insight into the mechanisms of damping which underlay the behavior of high-damping alloys can be obtained by examining the strain-dependence of the damping. The typical pattern of the strain-dependence of damping is shown in Figure 53, which was developed from data presented in [Ref. 99], for a number of high damping alloys.

It is observed that in most high-damping alloys, the damping which is realized is a sensitive function of the (cyclic) strain amplitude which is imposed, with damping increasing as the strain amplitude increases. Typically, there is a distinct

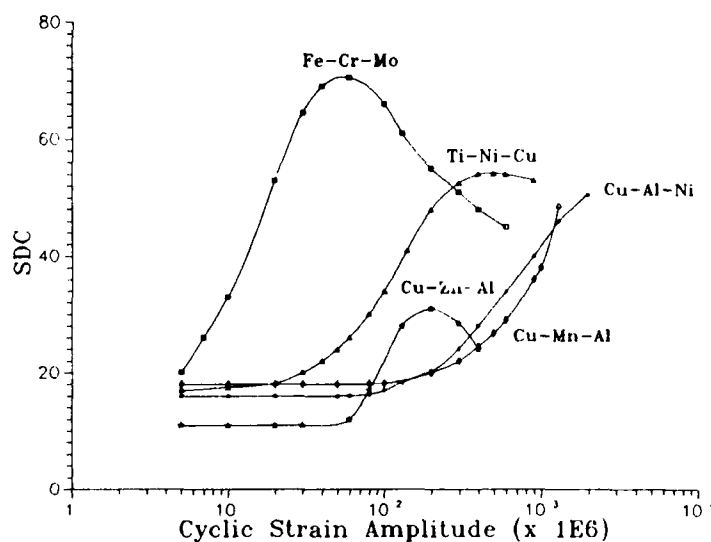


Figure 53: SDC vs cyclic strain amplitude for Ti-Ni, Cu-Al-Ni and Cu-Zn-Al shape memory alloys, a Fe-Cr-Mo ferromagnetic alloy, and a Cu-Mn-based anti-ferromagnetic alloy.

strain threshold, above which the high damping mechanism is activated. (The specific value of this strain threshold depends upon the alloy, and of course upon its prior thermomechanical history.) Above the strain threshold, the damping typically exhibits a strong dependence upon the cyclic strain, increasing rapidly as strain increases. Eventually, the damping saturates, that is, reaches a maximum.

This strain-dependant behavior suggests that each of these alloys has a mechanism of internal friction that can be activated only by the application of sufficient strain, and also that there is a limit to the ability of this mechanism to operate.

## 2. Damping by Microstructural Boundaries

Based on this information, we can conceive a simple microstructural model for high-damping alloys. First, we may note that in virtually all the well-known high-damping alloys, the microstructural features which are believed to be associated with high damping are some sort of mobile crystallographic boundaries. In the various classes of high damping alloys, these may be ferromagnetic domain walls, twin boundaries and so forth. Some illustrations of the form and distribution of such boundaries are given in Figure 54a & b.

As these photomicrographs show, the microstructure typically is subdivided by a large number of closely-spaced boundaries. In general, we may assume that the internal friction (damping) which can be provided by a given microstructure is dependent on:

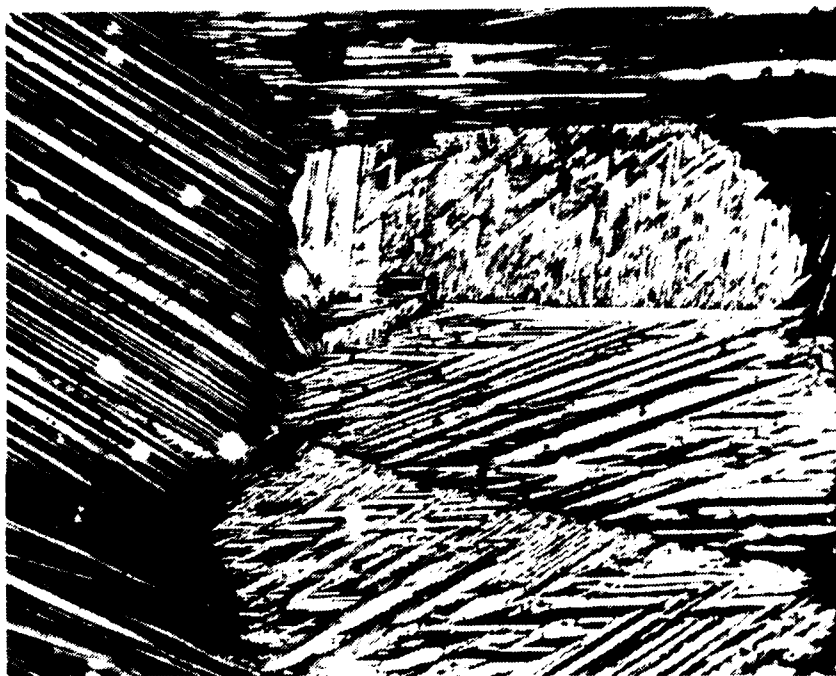


Figure 54: Illustration of the "subdivision" of parent phase grains into martensite plate variants in thermoelastic Cu-Zn-Al. The numerous intervariant boundaries can absorb energy as they move [Ref. 100].

1. The number of potentially high-damping features which are capable of reversible movement.
2. The extent to which these features move under given conditions.
3. The friction which resists such movement.

The essence of this qualitative description of high damping mechanisms can be paraphrased by stating that in order to realize high damping we must have available a lot of reasonably mobile features (which we now realize to be mainly mobile intercrystalline

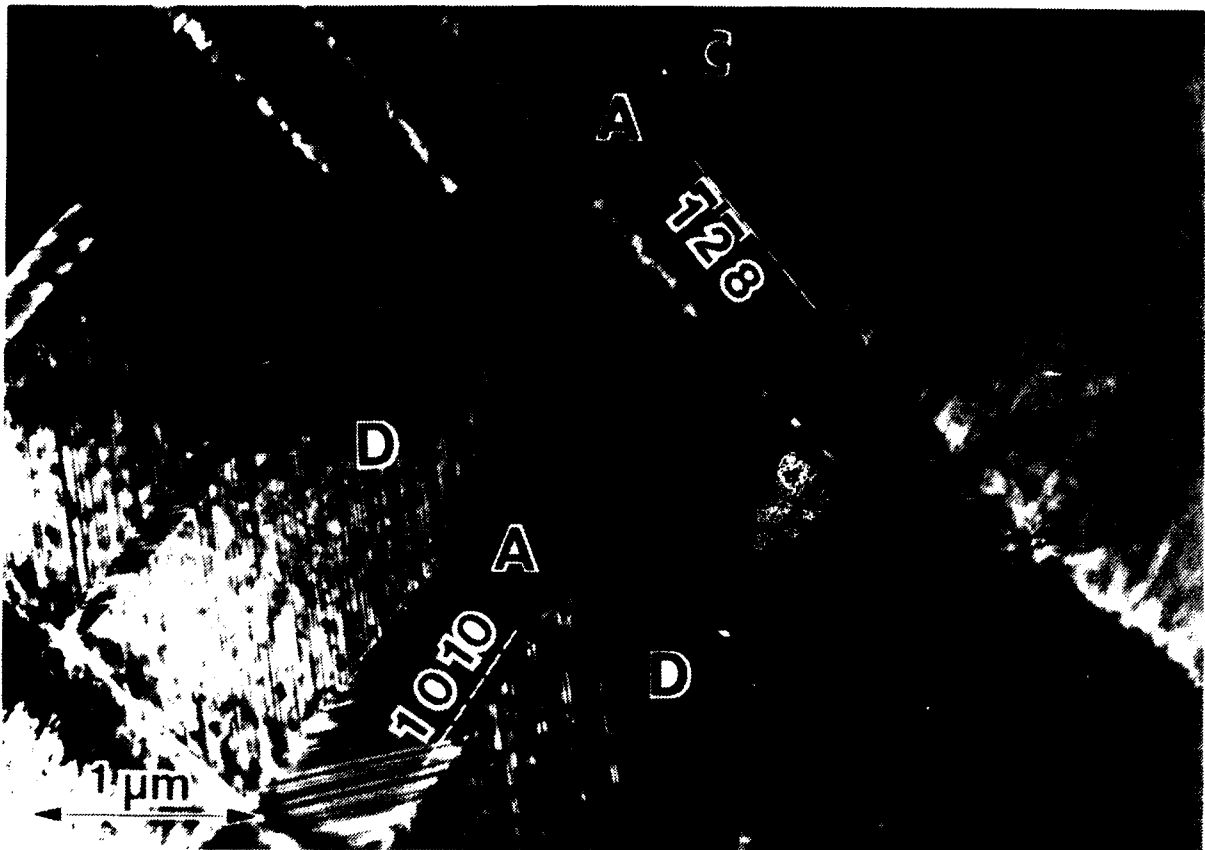


Figure 54: Faulted substructure details of the martensite plates in a Cu-Zn-Al alloy; these substructural boundaries are mobile, and contribute to the process of energy absorption. From [Ref. 101].

boundaries); furthermore, we must actually move these features, but they must not be too easy to move.

### 3. Atomistic Structure of High-Damping Boundaries in Microstructures

The obvious assumption has been stated: energy must be absorbed by the resistance to motion of these boundaries as they are moved. But exactly how is energy absorbed at the various types of mobile boundaries which have been mentioned above? This is a more difficult question to answer, since very little in the way of detailed structural modeling of the boundaries, let alone their internal friction, has been completed.

It is clear, of course, that the internal friction which is contributed by a given boundary as it moves should be a function of the atomistic structure of the boundary. Research has revealed some of the details of the atomistic structure of the boundaries in some high-damping alloys. For example, the nature of the boundaries in martensitic and in

ferromagnetic microstructures is pretty well understood in a general way, and in some specific cases, detailed models have been presented.

**a. Martensite Intervariant Boundaries**

For some of the thermoelastic martensitic alloys, interest in the shape memory behavior has led naturally to studies of the inherent mobility of the boundaries between the different orientation variants (plates), including the effect of structural and sub-structural (fault) variations on boundary structure and mobility.

For example, the intervariant boundary structure may be revealed by high resolution TEM, as in Figure 55. At such a boundary, the crystal structure of the martensite

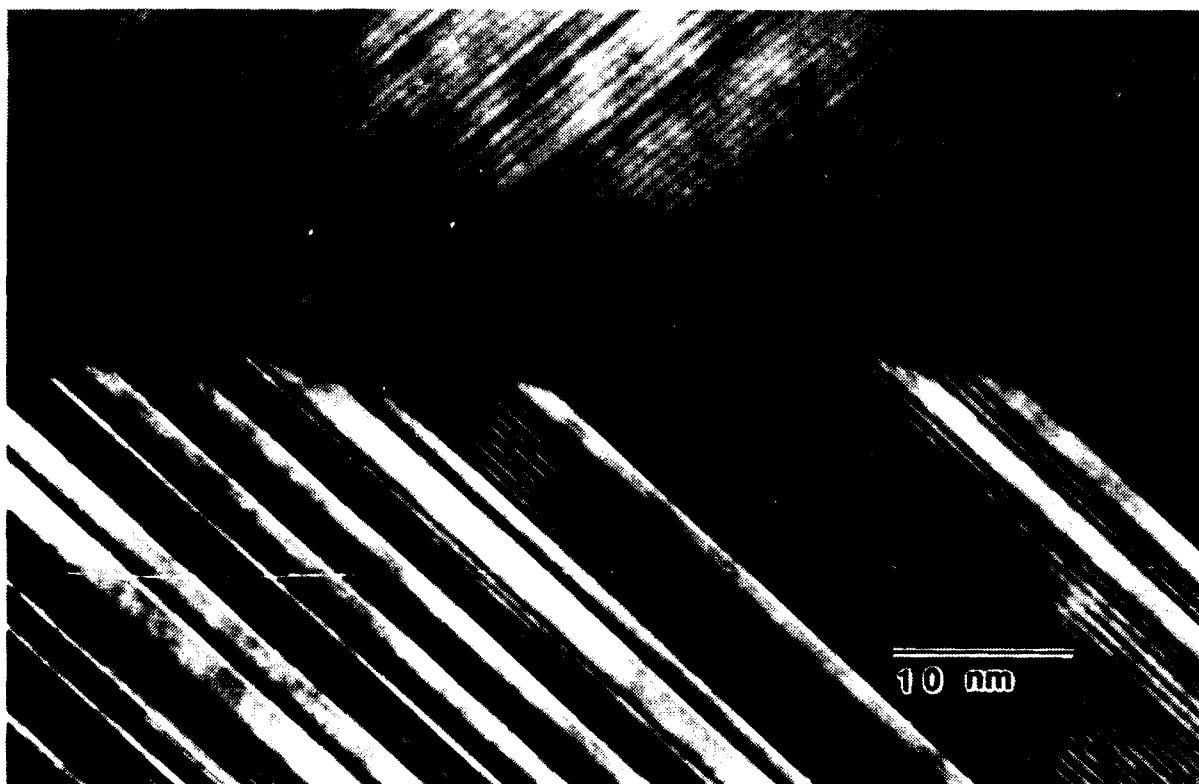


**Figure 55:** Shown here is a A/D intervariant boundary within a Cu-Al-Ni alloy. The presence of structural faults (2H structure) within the 18R martensite plates causes changes of the boundary inclination.

(in this case, 18R) quite abruptly changes orientation, with the crystal sections on either side of the boundary often adopting a twin relationship with one another. The type of information in the lattice image, together with the corresponding diffraction data can lead

to an atomistic model for the boundary, such as shown in Figure 55. In this particular case, the presence of 2H structural faults in the otherwise 18R martensitic structure changes the boundary structure [Ref. 101]; this is believed to decrease the mobility of the intervariant boundary, which may be unfavorable from the standpoint of shape memory applications, but probably increases the internal friction and would therefore be favorable for damping applications.

#### **b. Ferromagnetic Domain Walls**

Any elementary physics textbook will explain that the boundaries between ferromagnetic domains can be considered to be regions within which there is a gradual rotation of the magnetic dipole vector, as shown in Figure 56. On an atomistic level, such a boundary is considerably wider than a typical martensitic intervariant boundary. Under stress, domain walls are known to move according to the

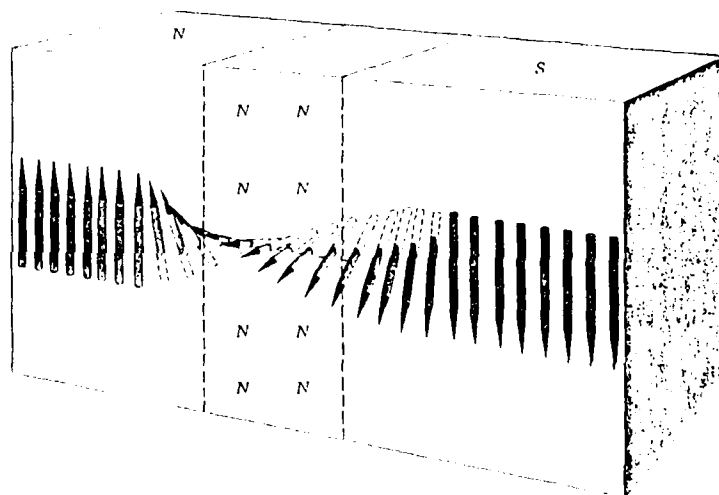


**Figure 56:** Schematic of a ferromagnetic domain wall. From [Ref. 102].

magnetostrictive effect. When such a boundary moves, energy is absorbed on the atomistic level by magnetization reversal of the particle. If the particle is large, magnetization reversal takes place via the process of boundary displacement, a process which requires weak fields and very little energy. But if the particle is small, the magnetization of the particle must rotate as a whole, requiring large fields [Ref. 102].

### **c. Mini-twins in Antiferromagnetic Mn-Cu Alloys**

It has been appreciated for some time that antiferromagnetically ordered Mn-rich Mn-Cu alloys can provide quite high damping. In these alloys, an FCC phase transforms upon cooling and becomes subdivided into an array of differently-oriented FCT regions. The microstructure which results is sometimes very similar in form to that of the thermoelastic martensitic alloys, illustrated above. In fact, the FCT regions in Mn-Cu alloys are simultaneously antiferromagnetic domains and what may be regarded as quasi-martensitic (very low strain martensite) variants. Because of the very low degree of tetragonality of the FCT structure, the intervariant boundaries would be expected to be quite mobile, and in fact, shape memory behavior has been reported for such microstructures.

#### **4. High Damping in Mn-Cu alloys**

In certain Mn-Cu alloys, a dispersion of Mn-enriched regions may be developed by aging, and this discrete array of regions then may undergo the FCC to FCT transformation on cooling; as for quenched homogeneous Mn-Cu alloys which undergo the FCC to FCT transformation, this also leads to a high-damping condition.

In the preceding sections of this thesis, the microstructure of these aged Mn-Cu alloys has been characterized in detail. At first glance (at the level of observation of conventional TEM), the microstructure are quite different from those of other high-damping alloys, wherein an array of distinctly planar boundaries are evident. For example, after relatively short aging times, a "tweed" contrast microstructure develops in these Mn-Cu alloys (see Figure 3), and although this corresponds to a quite high-damping condition, it is not immediately evident what sort of boundaries or other features may lie "under the tweed" and produce the large internal friction. Further study reveals that the "tweedy" microstructure contains an array of Mn-enriched regions (dispersed on about the scale of the tweed striations), and within each of these Mn-enriched regions is a set of FCT variants on a very



fine scale. In other words, the microstructure which is providing the high internal friction is very much like that of the thermoelastic martensitic alloys (or indeed of quenched homogeneous Mn-Cu alloys), but with a scale that is an order of magnitude or so finer.

The nature of the boundaries within the Mn-enriched regions of aged Mn-Cu alloys has been successfully studied using high resolution TEM. Such a study is assisted by the fact that as the alloy is aged longer, the Mn-enriched regions become somewhat larger and more discrete, so that the array of FCT variants within them can be more easily noticed, as seen in Figure 12.

High-resolution TEM studies confirm that the contrast observed in conventional TEM images is due to sets of very fine-scale twin-related FCT regions embedded in an FCC matrix. For example, the lattice image shown in Figure 32 reveals a small but discrete twin boundary between two very small FCT regions (the spacing of the 220 FCC matrix planes which are imaged is 0.217 nm). It is interesting to notice that the tetragonality on either side of the boundary is completely coherent with the surrounding FCC matrix. That is, there is no distinct boundary around the pair of tetragonal regions; rather, the tetragonality gradually blends into the FCC matrix. This, of course, provides the possibility of "boundaryless internal friction", or at least of internal friction produced by very diffuse interfaces (Consideration of the fact that ferromagnetic domain walls have an analogous diffuse width make this seem less unusual.)

Careful examination of Figure 32 reveals regions of the twin traces which appear to be cross-hatched. This can be explained as being due to the movement of the boundaries between differently oriented FCT regions during the photographic exposure. This confirms that the "flickering" contrast is due to the movement of the boundaries between differently oriented FCT regions.

These studies on aged Mn-Cu alloys have provided a unique opportunity to actually observe the action of the high-damping boundaries. While the movement of the boundaries in the TEM (which gives rise to the so-called "flickering" contrast) is clearly due to excitation of the thin foil by the incident beam (probably due to thermal stresses set up by non-uniform heating), and due to the cascading of the physical response from one region to another in the crystal (the nature of which has been shown to have chaotic character) [Ref. 103], it is probably reasonable to assume that the measured high damping of these alloys is due to a similar movement of these same boundaries when subjected to conventional mechanical excitation, that is, during macroscopic vibration of a component.

## VI. SUMMARY

The microstructural distribution of fine scale FCT regions formed in an aged Mn-Cu-based alloy was analyzed. In order to determine the orientation of the FCT crystallites, a variety of methods of analysis were used, including; diffraction streak direction, streak extinction and trace extinction. Candidate atomic displacements and FCT crystallite orientations were assumed and the expected results for the three analysis methods were predicted using mathematical methods. The actual results were compared to the predicted results and the displacements which did not predict directions or extinctions observed in the actual results were eliminated. Ultimately, this procedure showed that the crystallites are formed as  $\{110\}$  plates by shears of the form  $\{110\}\langle\bar{1}\bar{1}0\rangle$ .

The Cu-Mn phase diagram shows that a sample of Incramute aged at 400°C will disassociate within a miscibility gap to Mn-enriched regions at ~93 at. % Mn and Mn-depleted regions at ~37 at. % Mn. The FCC-FCT transformation occurs at ~82 at. % Mn at room temperature, and FCT Incramute's c/a ratio decreases from ~1.0 at the FCC-FCT transformation Mn concentration to ~.96 at 93 at. % Mn. The computer model developed to demonstrate Incramute composition profile changes with time reveals that the initial as solutionized composition profile gives way to small Mn-enriched regions surrounded by larger Mn-depleted regions. These initial Mn-enriched regions do not reach the maximum Mn concentration allowed by the miscibility gap, but with time, coarsening of the microstructure takes place and the Mn-enriched regions become both fewer in number, larger in size and reach a maximum concentration of ~93 at. % Mn. TEM photomicrographs show that in aged Incramute the Mn-enriched regions contain V-shaped images which closely resemble the self accommodating crystallite groups found in shape memory alloys. Alternate crystallites appear to be twin related, with the V-shape being the twin trace.

The changes in damping properties can be explained by the microstructure and composition profile changes that occur with aging. At early aging times when the FCC-FCT transformation Mn concentration is just reached, the FCT crystallites are very small and have a  $c/a$  ratio near 1.0. The damping experiment sets up vibrational waves in the Incramute matrix. Vibrational waves with the proper wave vector which enter these Mn-enriched regions reorient the  $c$ -axis of the FCT crystallite. Since the  $c/a$  ratio is near 1.0 only a small amount of energy is required for this reorientation which implies that the amount of energy lost by the vibrational wave is small. Incramute with this type of heat treatment exhibits a small damping coefficient increase over the solution treated alloy.

After more extended aging when the Mn-enriched region has grown and the maximum Mn concentration is reached, the microstructure consists of larger Mn-enriched regions with V-shaped images at the center. The  $c/a$  ratio of these regions varies from  $\sim 1.0$  at the point where the FCC-FCT transformation concentration of Mn is first reached to  $\sim .96$  nearer the center of the region. Vibrational waves with the proper wave vector that enter the FCT region first encounter FCT Incramute with a  $c/a$  ratio of 1.0 and reorient the  $c$ -axis of this region. As this reorientation takes place, the net strain field acting on the region is increased due to the  $c$ -axis alignment causing a net shrinkage in the direction of alignment ( $c/a$  is less than 1.0). This strain field added to the one caused by the vibrational wave is of sufficient amplitude to cause reorientation of the FCT crystallites in the center of the Mn-enriched region. This reorientation requires the movement of twin boundaries and thus absorbs a significant amount of energy. Incramute with this heat treatment shows the highest damping coefficient.

When overaged, the Incramute composition profile resembles a square wave, with abrupt composition changes between the Mn-enriched regions and Mn-depleted matrix. These rapid composition changes preclude the presence of any significant amount of FCT

Incrumute with  $c/a$  ratios greater than .96. The absence of these high  $c/a$  ratio regions results in the absence of the strain fields which aided the vibrational waves in reorienting the low  $c/a$  ratio, twin related FCT regions. This implies that vibrational waves that were of sufficient amplitude to reorient the low  $c/a$  ratio regions can no longer perform this reorientation and that damping is reduced. Incramute subjected to overaging displays a significantly smaller damping coefficient than Incramute with the aging treatment mentioned in the paragraph above.

Flickering can also be explained by changes in microstructure and composition profile with aging. Vibrational waves are created by uneven heating of the TEM sample by the electron beam. When a vibrational wave causes the reorientation of the  $c$ -axis, the strain fields of the initial  $c$ -axis orientation is relieved and a new strain fields is set up. Since strain fields in a TEM sample are viewed as images, it appears that the image has moved. These vibrational waves can move very rapidly, up to the speed of sound, ~5000 meters per second in metal. Thus reorientation of the  $c$ -axis is extremely rapid and appears by eye as the instantaneous movement of the image from one orientation to another. Flickering starts after a heat treatment which causes tweed structure to appear, about 4 hours at 400°C. The amount of flickering appears to increase with increased aging until some maximum is reached at about the same aging time at which the maximum damping coefficient is reached, and then slowly dies off at increased aging. Incramute heat treated to the point where its damping coefficient is essentially the same as it was when solution treated no longer exhibits flickering.

## APPENDIX

```

C  THIS PROGRAM DETERMINES THE COMPOSITION PROFILE OF A 1-D, UNIFORM
C  SAMPLE UNDERGOING SPINODAL DECOMPOSITION FOR VARIOUS ARBITRARY
C  TIMES. THE DIFFERENTIAL EQUATION IS:  $C_t = d \cdot C_{xx}$ . INITIAL  $M_n$ 
C  IS .480. MAXIMUM ALLOWED  $M_n$  CONCENTRATION IS .93, MINIMUM ALLOWED
C   $M_n$  CONCENTRATION IS .37 (ATOMIC PERCENT). DERIVATIVE BOUNDARY
C  CONDITIONS WITH FLUX ACROSS THE BOUNDARY EQUAL TO ZERO
C  ***** DIMENSION REQUIRED ARRAYS *****
C
DOUBLEPRECISION HSTEP,TK,SIZE,R,CJ(0:500),ALFA,SUM,DIFF,AN
DOUBLEPRECISION C(0:500),D(0:500),DD(0:500),L(0:500),TOTAL
REAL XX(0:500),CC(0:500),PTIME
C
C  ***** OPEN THE OUTPUT FILE *****
C
OPEN (UNIT = 11, STATUS = 'UNKNOWN', FILE='PROFILE.DAT')
OPEN (UNIT = 12, FILE = 'INPUT.DAT')
OPEN (UNIT = 13, FILE = 'LAMBDA.DAT')
OPEN (UNIT = 14, FILE = 'SLOPE.DAT')
OPEN (UNIT = 15, FILE='OLDPRO.DAT')
CALL QSETUP(2,3,-1,1)
C
C  ***** READ IN INPUT DATA *****
C
PRINT *, 'ENTER THE NUMBER OF INTERVALS AS AN INTEGER (100 MAX)'
PRINT *, 'MUST BE EVEN'
READ *, N
PRINT *, 'THE SELECTED NUMBER OF INTERVALS IS', N
PRINT *, 'ENTER THE FINAL TIME'
READ *, TIME
PRINT *, 'THE SELECTED FINAL TIME IS:', TIME
PRINT *, 'ENTER THE DESIRED VALUE OF R'
READ *, R
PRINT *, 'THE SELECTED VALUE OF R IS:', R
PRINT *, 'ENTER THE VALUE OF ALFA'
READ *, ALFA
PRINT *, 'THE SELECTED VALUE OF ALFA IS:', ALFA
READ (12,*) ISAVE
C
C  ***** CALCULATE THE REQUIRED NUMBER OF TIME STEPS *****
C
SIZE = N
HSTEP = 1/SIZE
PRINT *, 'HSTEP =', HSTEP
TK=12*R*HSTEP**2
PRINT *, 'TK =', TK
KSTEPS = TIME/TK

```

```

PRINT *, 'THE REQUIRED NUMBER OF TIME STEPS IS:', KSTEPS
WRITE (11,*) 'ALFA=', ALFA, 'R=', R, 'FINAL TIME =', TIME
C
C ***** SET IN THE INITIAL VALUES *****
C
JTIME = 0
TOTAL = 0
SUM = 0
IGRAF=0
PRINT *, 'TO CONTINUE A RUN TYPE 1, ELSE TYPE 0'
READ *, INEW
IF (INEW .EQ. 1) THEN
  READ(15,*) OLDTIM
  DO 1 I=0,N
    READ(15,*) XXX, C(I)
1  SUM = SUM + C(I)
    ELSE
      PI=3.14159265359
      DO 10 I = 0, N
        XI=I
        C(I) = .48 + .025*DCOS((PI/4.0)*XI)
10 SUM = SUM + C(I)
      ENDIF
C
C ***** START CALCULATIONS *****
C
CM=1
20 DO 25 I=0,N
  DD(I)=-13.74*CM*C(I)*(1-C(I))+1.33*CM+15.20*C(I)*(1-C(I))**2
25 CONTINUE
  CALL LAMBDA(N, C, L)
  D(2) = (DD(2)+ALFA/L(2)**2+DD(0)+ALFA/L(0)**2)/2
  D(1) = (DD(1)+ALFA/L(1)**2+DD(0)+ALFA/L(0)**2)/2
  D(0) = (32*D(1)-2*D(2))/30
  CJ(0) = -2*R*D(2)*C(2) + 32*R*D(1)*C(1) + (1-30*R*D(0))*C(0)
  D(3) = (DD(3)+ALFA/L(3)**2+DD(1)+ALFA/L(1)**2)/2
  D(2) = (DD(2)+ALFA/L(2)**2+DD(1)+ALFA/L(1)**2)/2
  D(0) = (DD(0)+ALFA/L(0)**2+DD(1)+ALFA/L(1)**2)/2
  D(1) = (16*D(0)+16*D(2)-2*D(3))/30
  CJ(1)=-2*R*D(3)*C(3)+16*R*D(2)*C(2)+16*R*D(0)*C(0)+(1-30*R*D(1))
;C(1)
  DO 30 I = 2, N-2
    D(I+2) = (DD(I+2)+ALFA/L(I+2)**2+DD(I)+ALFA/L(I)**2)/2
    D(I+1) = (DD(I+1)+ALFA/L(I+1)**2+DD(I)+ALFA/L(I)**2)/2
    D(I-1) = (DD(I-1)+ALFA/L(I-1)**2+DD(I)+ALFA/L(I)**2)/2
    D(I-2) = (DD(I-2)+ALFA/L(I-2)**2+DD(I)+ALFA/L(I)**2)/2
    D(I) = (16*D(I+1)+16*D(I-1)-D(I-2)-D(I+2))/30
    CJ(I) = -R*D(I-2)*C(I-2)+16*R*D(I-1)*C(I-1)+(1-30*R*D(I))*C(I)
; -R*D(I+2)*C(I+2) + 16*R*D(I+1)*C(I+1)
30 CONTINUE

```

```

      D(N-3) = (DD(N-3)+ALFA/L(N-3)**2+DD(N-1)+ALFA/L(N-1)**2)/2
      D(N-2) = (DD(N-2)+ALFA/L(N-2)**2+DD(N-1)+ALFA/L(N-1)**2)/2
      D(N) = (DD(N)+ ALFA/L(N)**2+ DD(N-1)+ALFA/L(N-1)**2)/2
      D(N-1) = (16*D(N)+16*D(N-2)-2*D(N-3))/30
      CJ(N-1)=-2*R*D(N-3)*C(N-3)+16*R*D(N-2)*C(N-2)+16*R*D(N)*C(N)
      ;+(1-30*R*D(N-1))*C(N-1)
      D(N-2) = (DD(N-2)+ALFA/L(N-2)**2+DD(N)+ALFA/L(N)**2)/2
      D(N-1) = (DD(N-1)+ALFA/L(N-1)**2+DD(N)+ALFA/L(N)**2)/2
      D(N) = (32*D(N-1)-2*D(N-2))/30
      CJ(N)=-2*R*D(N-2)*C(N-2)+32*R*D(N-1)*C(N-1)+(1-30*R*D(N))*C(N)
      DO 40 K = 0,N
40 C(K)=CJ(K)
C
C ***** SEE IF TIME STEPS ARE COMPLETE *****
C
      IF (JTIME + 1 .GE. KSTEPS) THEN
      GO TO 100
      ELSEIF (JTIME .EQ. IGRAF) THEN
      CALL QCLEAR(0,0)
      GO TO 90
      ELSE
      JTIME = JTIME + 1
      GO TO 20
      ENDIF
C
C ***** PRINT OUT RESULTS *****
C
90 TOT = 0
   TOTAL = 0
   XTIME = TK*JTIME
   PTIME = XTIME + OLDTIM
   DO 95 I=0,N
      X=HSTEP*I
      XX(I)=X
      CC(I)=C(I)
      TOTAL = TOTAL + C(I)
95  TOT = TOT + C(I)
   NN=N+1
   CALL QSMODE(16)
   CALL QPTABL(1,1.0,0.0,1.0,0.0,1.0,1,NN,XX,CC)
   CALL QQNPUT(450,300,PTIME,4)
   CALL QQNPUT(450,275,TOT,4)
   CALL DATA (N,C,PTIME)
   CALL AMOUNT(N,C,PTIME)
C
C ***** CORRECT FOR THE TRUNCATION ERROR *****
C
      AN = N+1
      DIFF = SUM - TOTAL
      DO 97 IJ= 0,N

```



```

97 C(IJ) = C(IJ) + DIFF/AN
   IF (JTIME .EQ. ISAVE) THEN
     WRITE (11,*) 'THE PRESENT TIME IS', PTIME
     DO 98 I=0,N
       WRITE (11,*) XX(I), C(I)
98 CONTINUE
     WRITE (11,*) 'TOTAL =', TOT
     READ (12,*) ISAVE
     ENDIF
     JTIME = JTIME + 1
     IGRAF = IGRAF + 100
     GO TO 20
100 TOT = 0
     PTIME = TK*KSTEPS + OLDTIM
     WRITE (11,*) 'THE PRESENT TIME IS', PTIME
     DO 110 I = 0,N
       TOT = TOT + C(I)
       PRINT *, I, ' C(I)= ', C(I)
       X = HSTEP * I
110 WRITE(11,*) X, C(I)
     WRITE(11,*) 'THE TOTAL IS', TOT
     PRINT *, 'THE TOTAL IS', TOT
     STOP
     END
     SUBROUTINE LAMBDA(N,C,L)
C *****
C               SUBROUTINE LAMBDA
C *****
C
C   THIS SUBROUTINE DETERMINES THE WAVELENGTH OF THE COMPOSITION
C   PROFILE FOR A BINARY ALLOY
C *****
C
C
DOUBLEPRECISION L(0:500), C(0:500)
  IPEAK = 0
  M = 1
  DO 20 II = 1,N
    IF (C(II).GT.C(II-1).AND.IPEAK.EQ.0) THEN
      M = M + 1
      ELSEIF (C(II).LE.C(II-1)) THEN
        M = M + 1
        IPEAK = 1
      ELSE
        DO 25 K = II-M,II
          L(K) = M
25    CONTINUE
        M = 1
        IPEAK = 0
      ENDIF

```

```

20  CONTINUE
    DO 30 K = II-M,II
30  L(K) = M
    RETURN
    END
SUBROUTINE DATA(N,C,PTIME)
C  *****
C  SUBROUTINE DATA
C  *****
C  THIS SUBROUTINE DETERMINES THE WAVELENGTH OF THE COMPOSITION
C  PROFILE FOR A BINARY ALLOY
C  *****
C
DOUBLEPRECISION L(0:500), C(0:500)
    IPEAK = 0
    M = i
    DO 20 II = 1,N
    IF (C(II)-C(II-1)).GT..02.AND.IPEAK.EQ.0) THEN
        M = M + 1
        ELSEIF (C(II)-C(II-1)).LE..02) THEN
            M = M + 1
            IPEAK = 1
        ELSE
            DO 25 K = II-M,II
            L(K) = M
25  CONTINUE
            M = 1
            IPEAK = 0
        ENDIF
    20  CONTINUE
        DO 30 K = II-M,II
30  L(K) = M
        NPEAK = 0
        ISTART = 0
35  IF (ISTART .GE. N) THEN
        GO TO 40
        ELSE
            ISTART = ISTART + L(ISTART)
            NPEAK = NPEAK + 1
        ENDIF
        GO TO 35
40  AN = N
        APEAK = NPEAK
        ALAMBDA = AN / APEAK
        WRITE (13,*) PTIME, ALAMBDA
        IPEAK = 0
        RETURN
    END

```

```

SUBROUTINE AMOUNT(N,C,PTIME)
C *****
C
C THIS SUBROUTINE ESTIMATES THE RELATIVE AMOUNT OF Mn AT .8 at. %
C +/- SOME DIFFERENTIAL AMOUNT BY FINDING REGIONS WHERE THE
C COMPOSITION IS .8, FINDING THE SLOPE IN THAT REGION AND ESTIMATES
C THE AREA CONTAINING THE REQUIRED COMPOSITION OF Mn BY
MULTIPLYING
C THE SLOPE TIMES THE RADIUS OF THE REGION GREATER THAN .8 at. %.
C *****
DOUBLEPRECISION C(0:500)
I = 0
AMT = 0.0
10 XM = 0.0
IF (I.EQ.N+1) THEN
GO TO 100
ELSEIF(C(I).GT..8.AND.I.EQ.0) THEN
20 I=I+1
IF(C(I).LE..8) THEN
SLOPE = C(I-1)-C(I)
XM = I-1
XPLUS = (C(I-1)-.8)/SLOPE
AMT = (1-.9*SLOPE) * (XM + XPLUS)
I = I + 1
GO TO 10
ENDIF
GO TO 20
ELSEIF (C(I).GT..8.AND.C(I-1).LT..8) THEN
SLOPE = C(I) - C(I-1)
XPLUS = (C(I) - .8)/SLOPE
DO 30 J = I+1,N
IF (C(J).LE..8) THEN
SLOPE = SLOPE + C(J-1) - C(J)
XPLUS = XPLUS + (C(J-1)-.8)/(C(J-1)-C(J))
AMT = AMT +(1-.9*SLOPE)*(XPLUS + XM)/2.0
I = I + 1
GO TO 10
ELSE
XM = XM + 1
ENDIF
30 CONTINUE
AMT = AMT + (1-.9*SLOPE) * (XPLUS + XM)
GO TO 100
ELSE
I = I + 1
ENDIF
GO TO 10
100 WRITE(14,*) PTIME,AMT
RETURN
END

```

## LIST OF REFERENCES

1. Dean, R. S., Long, J. R., Graham, T. R., E. V. Potter and Hayes, E. T., "The Copper-Manganese Equilibrium System," Transactions ASM, Vol. 34, pp. 443-464, 1945.
2. Dean, R. S., Potter, E. V. and Long, J. R., "Properties of Transitional Structures in Copper-Manganese Alloys," Transactions ASM, Vol. 34, pp. 465-500, 1945.
3. Dean, R. S., Long, J. R., Graham, T. R., Roberson, A. H. and Armantrout, C. E., "The Alpha Solid Solution Area of the Copper-Manganese-Aluminum System," Transactions AIME, Vol. 171, pp. 70-88, 1947.
4. Dean, R. S., Long, J. R. and Graham, T. R., "Copper-Manganese-Aluminum Alloys - Properties of Wrought Alpha Solid Solution Alloys," Transactions AIME, Vol. 171, pp. 89-104, 1947.
5. Meneghetti, D. and Sidhu, S. S., "Magnetic Structures in Copper-Manganese Alloys", Physical Review, Vol. 105, No. 1, pp. 130-135, 1957.
6. Bacon, G. E., Dunmur, I. W., Smith, J. H. and Street, R., "The Antiferromagnetism of Manganese Copper Alloys", Proceedings of the Royal Society of London, Series A, Vol. 241, pp. 223-238, 1957.
7. Street, R., "Magnetic Properties of Manganese Copper Alloys", Journal of Applied Physics, Supplement to Vol. 31, No. 5, pp. 310S-317S, 1960.
8. Schwaneke, A. E. and Jensen, J. W., "Magnetic Susceptibility and Internal Friction of Tetragonal Manganese-Copper Alloys Containing 70 Percent Manganese", Journal of Applied Physics, Supplement to Vol. 33, No. 3, pp. 1350-1351, 1962.
9. Makhurane, P. and Gaunt, P., "Lattice Distortion, Elasticity and Antiferromagnetic Order in Copper-Manganese Alloys", Journal of Physics C (Solid State Physics), Ser. 2, Vol. 2, pp. 959-965, 1969.
10. Worrell, F. T., "Twinning in Tetragonal Alloys of Copper and Manganese", Journal of Applied Physics, Vol. 19, pp. 929-933, 1948.
11. Siefert, A. V. and Worrell, F. T., "The Role of Tetragonal Twins in the Internal Friction of Copper Manganese Alloys", Journal of Applied Physics, Vol. 22, No. 10, pp. 1257-1259, 1951.
12. Basinski, Z. S. and Christian, J. W., "The Cubic-Tetragonal Transformation in Manganese-Copper Alloys", Journal of the Institute of Metals, Vol. 80, pp. 659-666, 1951-52.
13. Jensen, J. W., Schwaneke, A. E., and Walsh, D. F., "Fatigue Properties of Manganese-Copper Damping Alloys", Bureau of Mines Report of Investigations 5853, U.S. Department of Interior, 1961.

14. Jensen, J. W. and Walsh, D. F., "Manganese-Copper Damping Alloys", Bureau of Mines Bulletin 624, U.S. Department of Interior, 1965.
15. Entwistle, K. M., Christian, J. W., Birchon, D., Bromley, D. E., Goodwin, R. J., Kelly, P. M., Brammar, I. S., Ball, A., Williams, K. J. and Roberts, E., "Discussion: The Physical Metallurgy of Alloys of High Damping Capacity", Journal of the Institute of Metals, Vol. 93, pp. 546-549, 1964-65.
16. Butler, E. P. and Kelly, P. M., "High Damping Capacity Manganese-Copper Alloys. Part 1 - Metallography", Transactions of the Metallurgical Society of AIME, Vol. 242, pp. 2099-2106, 1968.
17. Butler, E. P. and Kelly, P. M., "High Damping Capacity Manganese-Copper Alloys. Part 2 - The Effect of Storage and of Deformation on the Damping Capacity of 70/30 Mn-Cu Alloy", Transactions of the Metallurgical Society of AIME, Vol. 242, pp. 2107-2109, 1968.
18. Birchon, D., Bromley D. E. and Healey, D., "Mechanism of Energy Dissipation in High-Damping-Capacity Manganese-Copper Alloys", Metal Science Journal, Vol. 2, pp. 41-46, 1968.
19. Goodwin, R. J., "Manganese-Copper Alloys of High Damping Capacity", Metal Science Journal, Vol. 2, pp. 121-128, 1968.
20. Hedley, J. A., "The Mechanism of Damping in Manganese-Copper Alloys", Metal Science Journal, Vol. 2, pp. 129-137, 1968.
21. Sugimoto, K., Mori, T. and Shiode, S., "Effect of Composition on the Internal Friction and Young's Modulus in Gamma-Phase Mn-Cu Alloys", Metal Science Journal, Vol. 7, pp. 103-108, 1973.
22. Smith J. H. and Vance, E. R., "Decomposition of Gamma-Phase Manganese Copper Alloys", Journal of Applied Physics, Vol. 40, No. 12, pp. 4853-4858, 1969.
23. Stokes, H. J. and Hewin, I. D., "The Effect of Aging on Young's Modulus, Electrical Resistivity, and Hardness of 80:20 Manganese-Copper Alloy.", Journal of the Institute of Metals, Vol. 89, pp. 77-79, 1960-61.
24. Vintaykin, Ye. Z., Litvin, D. F. and Udovenko, V. A., "Fine Crystalline Structure in Highly Shock-Absorbing Alloys of Manganese and Copper", Physical Metallurgy and Metallography (in Russian, Fiz. Metal. Metalloved.), Vol. 37, No. 6, pp. 1228-1237, 1974.
25. Vitek, J. M. and Warlimont, H., "On a Metastable Miscibility Gap in Gamma-Mn-Cu Alloys and the Origin of their High Damping Capacity", Metal Science, Vol. 10, No. 1, pp. 7-13, 1976.
26. Venkateswararao, P. and Chatterjee, D. K., "Structural Studies on the Alloying Behavior of Gamma-Mn and the Development of a High Damping Capacity in Mn-Cu Alloys", Journal of Material Science, Vol. 15, pp. 139-148, 1980.

27. Vintaykin, Ye. Z., Udovenko, V. A., Dmitriyev, V. B. and Bichinashvili, A. I., Problemy metalloved i fiz. met. 3, Moscow, Metallurgiya, 1975.
28. Vintaykin, Ye. Z., Dmitriyev, V. B. and Udovenko, V. A., "Spinodal Decomposition in Manganese-Copper Alloys", Physical Metallurgy and Metallography, Vol. 46, No. 4, pp. 97-107, 1978.
29. Gaulin, B. D., Spooner, S. and Morii, Y., "Kinetics of Phase Separation in  $Mn_{0.67}Cu_{0.33}$ ", Physical Review Letters, Vol. 59, No. 6, pp. 668-671, August 1987.  
30. Spooner, B. D., Gaulin and Y. Morii, "An in-situ study of decomposition in manganese-rich copper-manganese alloys with neutron scattering", Proceedings of Phase Transformations '87, Institute of Metals, London, pp. 158-159, (1988)
31. Menshikov, A. Z., Favstov, Yu. K., Kochetkova, L. P., Konoplev, L. M. and Dorofeyev, Yu. A., "Structural Transformations During the Tempering of High-Damping Manganese-Copper Alloys", Physical Metallurgy and Metallography (in Russian, Fiz. Metal. Metalloved.), Vol. 39, No. 4, pp. 793-800, 1975.
32. Bichinashvili, A. I., Vintaykin, Ye. Z., Litvin, D. F. and Udovenko, V. A., "X-ray Investigation of the FCC to FCT Transformation in Manganese-Copper Alloys", Physical Metallurgy and Metallography (in Russian, Fiz. Metal. Metalloved.), Vol. 41, No. 1, pp. 112-117, 1976.
33. Kuteliya, E. R., Kerashvili, V. N. and Sanadze, V. V., "Electron Microscopic Investigation of the Processes of Separation of High-Copper Cu-Mn Alloys", Physical Metallurgy and Metallography (in Russian, Fiz. Metal. Metalloved.), Vol. 44, No. 5, pp. 190-194, 1977.
34. Vintaykin, Ye. Z., Dmitriyev, V. B. and Udovenko, V. A., "Antiferromagnetism in Heterogeneous Manganese-Copper Alloys", Physical Metallurgy and Metallography (in Russian, Fiz. Metal. Metalloved.), Vol. 44, No. 5, pp. 107-113, 1979.
35. Vintaykin, Ye. Z., Sakhno, V. M. and Udovenko, V. A., "Fine Crystal Structure of MnCuGe Alloys", Physical Metallurgy and Metallography, Vol. 51, No. 4, pp. 93-97, 1981.
36. Guseva, L. N., Dolinskaya, L. K. and Skurikhin, M. N., "Aging of Alloy Cu + 72% Mn Alloyed with Nickel, Iron and Aluminum", Izvestiya Akademii Nauk SSSR. Metall., No. 6, pp. 138-142, 1984.
37. Zolotukhin, I. V., Tkachenko, T. V., Skorobogatov, V. S. and Shvetsov, N. F., "Effect of Heat Treatment on Damping Mechanical Oscillations in a 70%Mn-30%Cu Alloy", Soviet Journal of Non-Ferrous Metals, (in Russian, Tsvetnize Metall.), no vol., pp. 63-64, 1974.
38. V'yunenکو Yu. N. and Likhachev, V. A., "Internal Friction in Alloys Based on CuMn", Problemy Prochnosti (Translated into English by Plenum Publishing Corp., 1986), No. 5, pp. 59-62, 1985.

39. Demin, S. A., Ustinov, A. I. and Chuistov, K. V., "The Nature of the Volume Effect in Mn-Cu Alloys", Soviet Physics - Doklady, Vol. 24, No. 5, pp. 387-389, 1979.
40. Vintaykin, Ye. Z., Udovenko, V. A., Litvin, D. F. and Serebryakov, V. G., "Elastic Constants of Manganese-Copper Alloys", Physical Metallurgy and Metallography (in Russian, Fiz. Metal. Metalloved.), Vol. 49, No. 4, pp. 182-185, 1980.
41. Vintaykin, Ye. Z., Udovenko, V. A., Mikke, K. and Yankovska, I., "Phonon Spectra in Gamma-Mn Alloys Near the Face-Centered Cubic to Face-Centered Tetragonal Transformation", Soviet Physics - Doklady, Vol. 26, No. 6, pp. 617-618, 1981.
42. Vintaikin, Ye. Z., Sakhno, V. M. and Udovenko, V. A., "Local Premartensitic Instability in FCC Manganese-Copper Alloys", Soviet Physics - Doklady, Vol. 24, No. 5, pp. 393-395, 1979.
43. Vintaikin, Ye. Z. and Udovenko, V. A., "Premartensite Instabilities in Manganese-Copper Alloys", Physical Metallurgy and Metallography (in Russian, Fiz. Metal. Metalloved.), Vol. 51, No. 5, pp. 160-162, 1981.
44. Vintaykin, Ye. Z., Matorin, V. I., Udovenko, V. A. and Shcherbedinskij, G. V., "The Premartensitic Instability of FCC Gamma-Mn-Based Alloys", Proceedings of The International Conference on Martensitic Transformations, The Japan Institute of Metals, pp. 121-126, 1986.
45. Savitskii, E. M., Burkhanov, G. S. and Zalivin, I. M., "Mechanical-Memory Effect in Manganese-Copper Alloy", Soviet Physics - Doklady, Vol. 17, No. 5, pp. 492-494, 1972.
46. Vintaykin, Ye. Z., Udovenko, V. A., Bichinashvili, A. I. and Litvin, D. F., "Reversible Deformation During Martensitic and Reverse Martensitic Transformations in Manganese-Copper Alloys", Soviet Physics - Doklady, Vol. 20, No. 5, pp. 357-359, 1975.
47. Vintaykin, Ye. Z., Litvin, D. F., Makushev, S. Yu. and Udovenko, V. A., "The Structural Mechanism of the Form-memory Effect in Mn-Cu Alloys", Soviet Physics - Doklady, Vol. 21, No. 7, pp. 405-407, 1976.
48. Vintaykin, Ye. Z., Udovenko, V. A., Makushev, S. Yu. and Litvin, D. F., "The Shape Memory Effect and Mechanism of Plastic Deformation in Manganese-Copper Alloys", Physical Metallurgy and Metallography (in Russian, Fiz. Metal. Metalloved.), Vol. 45, No. 4, pp. 139-144, 1978.
49. Vintaykin, Ye. Z., Sakhno, V. M. and Udovenko, V. A., "Reversible Shape Memory Effect in Alloys of Manganese with Germanium and Gallium", Physical Metallurgy and Metallography, Vol. 46, No. 3, pp. 161-163, 1978.
50. Demin, S. A., Ustinov, A. I. and Chuistov, K. V., "Plastic Deformation and Shape Recovery in Mn-Cu Alloys During the FCC-to-FCC Transformation Under Constant Stresses", Physical Metallurgy and Metallography, Vol. 52, No. 1, pp. 179-182, 1981.

51. Aravin, B. P., Kuz'min, S. L. and Likhachev, V. A., "Shape Memory Effect in MnCu Alloys", Physics of Metals (in Russian, Metallofizika), Vol. 3, No. 4, pp. 739-753, 1981.
52. Vintaykin, Ye. Z., Litvin, D. F. and Makushev, S. Yu., "Critical Shear Stresses of Twinning and Glide in Manganese-Copper Alloys with Tetragonal Structure", Soviet Physics - Doklady, Vol. 23, No. 6, pp. 425-427, 1978.
53. Aoyagi, T. and Sumino, K., "Mechanical Behavior of Crystals with Twinned Structure", Physica Status Solidi, Vol. 33, pp. 317-326, 1969.
54. Sumino, K., "Experimental Determination of Intrinsic Resistive Stress for Twinning Surface Dislocations", Physica Status Solidi, Vol. 33, pp. 327-335, 1969.
55. Sugimoto, K. and Mizutani, K., "Changes of Internal Friction and Young's Modulus Associated with 400 C - Aging in High Damping Mn-Cu and Mn-Cu-Ni Alloys", Journal of Japan Institute of Metals, Vol. 39, No. 5, pp. 503-511, 1975.
56. Sugimoto K. and Ohta, K., "Velocity Anomaly and Attenuation Peak Of Cu-37%Mn Single Crystal in the Vicinity of its Phase Transformation Temperature", Proc. of the 6th International Conference on Internal Friction and Ultrasonic Attenuation in Solids, Tokyo, pp. 725-729, 1977.
57. Ito, K., Kobayashi, M. and Tsukishima, M., "High Damping Capacity in Mn-Base Gamma-Phase Alloys", Journal De Physique, Vol. C5, pp. C5.641-C5.646, 1981.
58. Sogabe, Y., Kishida, K. and Nakagawa, K., "Wave Propagation Analysis for Determining the Dynamic Properties of High Damping Alloys", Bulletin of the Japan Society of Mechanical Engineering, Vol. 25, No. 201, pp. 321-327, 1982.
59. Ito, K., and Tsukishima, M., "Damping Capacity of  $(\text{Mn}_{1-x}\text{Co}_x)_{0.95}\text{Cu}_{0.05}$  Metastable Gamma-Phase Alloys", Transactions of the Japan Institute of Metals, Vol. 26, No. 5, pp. 319-324, 1985.
60. Tsunoda, Y. and Nakai, Y., "X-ray and Neutron Scattering Measurements in Mn-rich Gamma-MnCu Alloy Single Crystal", Journal of the Physical Society of Japan, Vol. 50, No. 1, pp. 90-96, 1981.
61. Tsunodo, Y. and Wakabayashi, N., "Phonons and Martensitic Transformation in Mn-rich Gamma-MnCu Alloys", Journal of the Physical Society of Japan, Vol. 50, No. 10, pp. 3341-3348, 1981.
62. Tsunoda, Y., Oishi N. and Kunitomi, N., "Bulk Modulus and Martensitic Transformation in Mn-Cu Alloys", Physica, 119B, pp. 51-55, 1983.
63. Nittono, O., Satoh, T. and Koyama, Y., "Cubic-Tetragonal Transformation and Reversible Shape Memory Effect in Manganese-Copper Alloys", Transactions of the Japan Institute of Metals, Vol. 22, No. 4, pp. 225-236, 1981.



64. Shimizu, K., Okumura, Y. and Kubo, H., "Crystallographic and Morphological Studies on the FCT to FCT Transformation in Mn-Cu Alloys", Transactions of the Japan Institute of Metals, Vol. 23, No. 2, pp. 53-59, 1982.
65. Ito, K., Tsukishima M. and Kobayashi, M., "Temperature Dependence of Lattice Parameters and the FCC/FCT/FCO Transformation in Some Mn-Based Metastable Gamma-Phase Alloys", Transactions of the Japan Institute of Metals, Vol. 24, No. 7, pp. 487-490, 1983.
66. Warlimont, H., Bernecker, K. and Luck, R., Z. Metallk., Vol. 62, p. 816, (1971)
67. Warlimont, H., "Zur Bedeutung des Gefuges hochdampfender Legierungen", Radex-Rundschau (in German), Vol. 1/2, pp. 108-114, 1980.
68. Wolfenden, A., "Mechanical Damping at 40 KHz in Mn-Cu Alloys", Physica Status Solidi (a), Vol. 44, pp. K171-K175, 1977.
69. Yeomens S. R. and McCormick, P. G., "An Investigation of Precipitation and Strengthening in Age-hardening Copper-Manganese Alloys", Materials Science and Engineering, Vol. 34, pp. 101-109, 1978.
70. Cowlam, N., Bacon, G. E. and Gillott, L., "Changes in Cell Dimensions at the Martensitic Transformation in Gamma Mn-Cu Alloys", Journal of Physics F: Metal Phys., Vol. 7, No. 12, pp. L315-L319, 1977.
71. Pan, Z.-L., Sprungmann, K. W., Schmidt, H. K. and Ritchie, I. G., "Internal Friction in Some High-Damping Alloys", Proceedings of the 5th European Conference on Internal Friction and Ultrasonic Attenuation in Solids, J. de Physique, C8, 573, 1987.
72. Pan, Z.-L. and Ritchie, I. G., "Harmonic Generation Associated with Nonlinear Friction in a High-Damping Mn-Cu Alloy", Proceedings of the 5th European Conference on Internal Friction and Ultrasonic Attenuation in Solids, J. de Physique, C8, 347, (1987)
73. Harangozo, I. Z., Egri, L., Kedves, F. J. and Kiss, S., "Internal Friction of High Damping Capacity Manganese Alloys", Journal De Physique, Vol. C9, pp. C9.303-C9.306, 1983.
74. Perkins, J., "Tweed Microstructures and the Evolution of High Damping in Cu-Mn Based Alloys", Phase Transformations '87, Institute of Metals, London, pp. 165-168, 1988.
75. Binary Alloy Phase Diagrams (T. B. Massalski, Editor-in-Chief; J. L. Murray, L. H. Bennett and H. Baker, Editors), American Society for Metals, 934, (1986)
76. A quasimartensitic transformation is a diffusionless phase transformation which has the crystallographic and morphological characteristics of a martensitic transformation but which is not dominated by strain energy. This occurs in cases where there is a very small volume change in the transformation.

77. Perkins, J., Mayes, L.L., Yamashita, T., Wu, M. H. and Reskusich, J., "Pre-Martensitic Transitions in Aged Cu-Mn Alloys", Proc. MRS Intl. Meeting on Advanced Materials (Tokyo 1988), Symposium on Shape Memory Materials (K. Shimizu and K. Otsuka, eds.), Materials Research Society, Pittsburgh (1988)
78. Oshima, R., Sugiyama, M. and Fujita, F. E., "Tweed Structures Associated with Fcc-Fct Transformations in Fe-Pd Alloys", Metallurgical Transactions A Vol. 19A, pp. 803-810, (1988)
79. Perkins, J., Adachi, K., Wu, M.H. and Yamashita, T., "TEM Studies of Transformation Interfaces and Substructures in some Copper -Based Shape-Memory Alloys", Ultramicroscopy, Vol. 30, pp. 217-232, (1988)
80. Van Tendeloo, G., Chandrasekaran, M. and Lovey, F.C., "Modulated Microstructures in  $\beta$  Cu-Zn-Al", Metallurgical Transactions A, Vol. 17A, pp. 2153-2161, (1986)
81. Robertson, I. M. and Wayman, C. M., "Tweed Microstructures: I. Characterization of Beta-NiAl", Philosophical Magazine A, Vol. 48, No. 3, pp. 421-442, 1983.
82. Robertson, I. M. and Wayman, C. M., "Tweed Microstructures: II. In several Phases of the Ni-Al System", Philosophical Magazine A, Vol. 48, No. 3, pp. 443-467, 1983.
83. Robertson, I. M. and Wayman, C. M., "Tweed Microstructures: III. Origin of the Tweed Contrast in Beta and Gamma Ni-Al Alloys", Philosophical Magazine A, Vol. 48, No. 4, pp. 629-647, 1983.
84. Tanner, L.E., "Diffraction Contrast from Elastic Shear Strains due to Coherent Phases", Philosophical Magazine, Vol. 14, No. 127, p. 111, 1966.
85. Delaney, L., Perkins, J. and Massalski, T.B., "Review: On the Structure and Microstructure of Quenched Beta-Brass Type Alloys", Journal of Materials Science, Vol. 7, pp. 1197-1215, 1972.
86. Tanner, L.E., "The Ordering Transformation in  $Ni_2V$ ", Acta Metallurgica, Vol. 20, pp. 1197-1227, 1972.
87. Schryvers, D., Tanner, L.E. and Van Tendeloo, G., "Premartensitic Microstructures as Seen in the High Resolution Electron Microscope: A Study of a Ni-Al Alloy", Proc. NATO/ASI Symposium on Phase Stability, Crete, 1984 (A. Gonis and M. Stocks, Eds.), Martinus Nijhoff Publishers, Dordrecht, Netherlands, (1988)
88. Zener, C., "Contributions to the Theory of Beta-Phase Alloys", Physical Review, Vol. 71, p. 846, 1947.
89. Tanner, L.E., private communication, (1988)
90. Silberstein, A. and Clapp, P. C., "Modeling and Interpretation of Tweed Microstructures in Face Centered Cubic Solids", Physical Review B, Vol. 38, No. 14, pp. 9555-9566, 1988.

91. T. Saburi and C. M. Wayman, "Crystallographic Similarities in Shape Memory Martensites", Acta Metallurgica, Vol. 27, pp. 979-995, (1979)
92. Tsunoda, Y., Oishi, N. and Kunitomi, N., "Bulk Modulus and Martensitic Transformation in Mn-Cu Alloys", Physica, Vol. 119B, pp. 51-55, 1983
93. Vitek, J. M. and Warlimont, H., "On a metastable Miscibility Gap in  $\gamma$ -Mn-Cu Alloys and the Origin of their High Damping Capacity", Metal Sciences, Vol. 10, No. 1, pp. 7-13, 1976.
94. Hillert, M., "A Solid Solution Model for Inhomogeneous Systems", Acta Metallurgica, Vol. 9, pp. 525-535, 1961.
95. Clapp, P. C., "Localized Soft Modes Theory for Martensitic Transformations", Phys. Status Solidi. B, Vol. 57, pp. 561-569, 1973.
96. Shewman, P. G., "Transformations in Metals", pp. 291-299, J. Williams Book Co., 1983.
97. Cahn, John W., "Spinodal Decomposition", Transactions of the Metallurgical Society of AIME, Vol. 242, pp. 166-180, 1968.
98. Reskusich, J. and Perkins, J., "Damping Behavior of Inframute: Strain Dependence and Heat Treatment Effects", Prepared for David Taylor Naval Ship Research and Development Center, 1986.
99. Roey, K. P., "A Comparison of Cu-Al-Ni and other High Damping Alloys for the Purpose of Naval Ship Silencing Applications", Master's Thesis, Naval Postgraduate School, Monterey, California, September 1989.
100. Adachi, K., Perkins, J. and Wayman, C.M., "The Crystallography and Boundary Structure of Interplate-Group Combinations of 18R Martensite Variants in Cu-Zn-Al Shape Memory Alloys", Acta Metallurgica, Vol. 36, No. 5, pp. 1343-1364, 1988.
101. Adachi, K. and Perkins, J., "Lattice Image Studies on the Intervariant Boundary Structure and Substructure of Cu-Zn-Al 18R Martensite", Metallurgical Transactions, Vol. 16A, pp. 1551-1566, 1985.
102. Kittel, C., "Introduction to Solid State Physics, 5th Edition", p. 492, John Wiley & Sons, 1976.
103. Farkas, D. M., "A Microstructural Investigation of the Shear Distortions and Energetics of Motion Observed in an Aged High Damping 53Cu-45Mn-2Al Alloy", Master's and Mechanical Engineer's Thesis, Naval Postgraduate School, Monterey, California, March 1989.

# INITIAL DISTRIBUTION LIST

|    |  | No. Copies |
|----|--|------------|
| 1. | Defense Technical Information Center<br>Cameron Station<br>Alexandria, Virginia 22304-6145   | 2          |
| 2. | Library, Code 0142<br>Naval Postgraduate School<br>Monterey, California 93943-5002   | 2          |
| 3. | Professor Jeff Perkins, Code 69/Ps<br>Department of Mechanical Engineering<br>Naval Postgraduate School<br>Monterey, California 93943-5004 | 6          |
| 4. | Research Administration, Code 012<br>Naval Postgraduate School<br>Monterey, California 93943-5000  | 1          |
| 5. | Guy V. Holsten<br>care of J. Hafley<br>111 David's Way<br>Yorktown, Virginia 23692   | 2          |
| 6. | Department Chairman, Code 69 HY<br>Department of Mechanical Engineering<br>Naval Postgraduate School<br>Monterey, California 93943-5000    | 1          |
| 7. | Naval Engineering Curricular Office, Code 34<br>Naval Postgraduate School<br>Monterey, California 93943-5000                               | 1          |
| 8. | Mrs. Catherine Wong, Code 2812<br>David Taylor Naval Ship R & D Center<br>Annapolis, Maryland 21402  | 2          |
| 9. | Mr. Robert Hardy, Code 2803<br>David Taylor Naval Ship R & D Center<br>Annapolis, Maryland 21402   | 1          |